Wide-Band Multi-Mode Voltage Tuning Oscillators utilizing Phase-Change Switches

Submitted in partial fulfillment of the requirements for

the degree of

Doctor of Philosophy

In

Electrical and Computer Engineering

Ahmad B. Khairi

B.S., Electrical Engineering and Computer Science, Harvard College

Carnegie Mellon University
Pittsburgh, PA

September, 2016

ACKNOWLEDGEMENT

I would like to express my thanks and appreciation to my advisor, Prof. Jeyanandh Paramesh, who has guided, assisted, motivated and challenged me throughout my research work with his vast knowledge and creative thinking. I would also like to extend my gratitude to my dissertation committee: Prof. James Bain, Prof. L. Richard Carley and Dr. Robert M. Young for their advice and feedback.

I would like to thank Erkan Alpman, Stefano Pellerano, Brent Carlton, Ashoke Ravi and Amr Fahim for their help, support, friendship and guidance throughout my internship at Intel Labs. I would also like to thank Howard Samuels, Qingdong Meng, Alex Alexeyev and Andrew Milia for their help and support throughout my internship at ADI Lyric Labs.

In addition, I would like to acknowledge the Defense Advanced Research Projects Agency (DARPA) RF-FPGA for supporting this research. This work was partially supported by DARPA/MTO under the RF-Field Programmable Logic Array Program, and by the National Science Foundation under grant ECCS- 1309927 *"Reconfigurable All-Digital CMOS Frequency Synthesizers for Cognitive and Milimeter-Wave Radios"*.

I would also like to thank my fellow graduate students and colleagues Rahul Singh, Sandipan Kundu, Jaewon Choi, Cheng-Yuan Wen, Mohsen Shahmohammadi, Shadi Saberi, Shih-Chang Hung, Ahmed Hussein and Mazen Soliman for their friendship, help and support throughout my studies.

And last but not least, I would like to thank those who provided me with endless love and encouragement during my ups and downs over my time, my mother Shahrazad Dajani, my father Bashir Khairi, my sister Haneen Khairi and my dearest friends Rosemary Townsend, Ammar Ammar and Ashley Dubnick.

ABSTRACT

With the emergence of multi-standard and cognitive radios, the need for reconfigurable RF circuits increased. Such circuits require wide-band quadrature voltage controlled oscillators (QVCOs) to provide the local oscillator (LO) signal for up and down conversion. Wide-band QVCOs performance has lagged behind their narrowband VCO counterparts and numerous circuit techniques have been introduced to bridge the gap.

This dissertation presents techniques that have been used to implement wide-band reconfigurable QVCOs with focus on dual-resonance based circuits. System and circuit analysis are performed to understand the tuning-range, phase noise, and power tradeoffs and to consider quadrature phase errors. An 8.8-15.0 GHz actively coupled QVCO and a 13.8-20GHz passively coupled QVCO are presented. Both oscillators employ dual-resonance to achieve extended tuning ranges. Impulse sensitivity functions were used to study the impact of different passive and active device noises on the overall phase noise performance of the dual-resonance oscillator and the actively and passively coupled quadrature oscillators. The quadrature phase error due to the different architecture parameters were investigated for the actively and passively coupled quadrature oscillators.

The advantages of using switched capacitor tuning as a major part of passive tuning are identified, and the advantage of employing switches with large bandwidths, such as those associated with phase change materials, is mathematically quantified.

Furthermore, a novel method for accurate off chip phase error measurement using discrete components and phase shifters that does not require calibration is introduced.

Contents

1. ACKNOWLEDGEMENT ii

2. ABSTRACT iii

4. LIST OF FIGURES ix

5. LIST OF TABLES xvii

1. INTRODUCTION 1

1.1. Background 1

1.2. Thesis Contribution and Organization 5

2. WIDE-BAND TUNING QVCOS BACKGROUND 9

2.1. Introduction 9

2.2. Voltage Controlled Oscillator (VCO) Basics 9

2.3. VCO Tuning 15

2.3.1. Capacitance Degeneration 15

2.3.2. Multi-Mode Resonance 16

2.4. Start-Up Condition 18

2.4.1. Barkhausen's Criterion 18

2.4.2. Root Locus Method 18

2.4.3. Nyquist Stability Criterion 18

2.4.4. The Start-Up Condition of the Basic VCO 19

2.4.5. VCO Start-Up Summary 22

2.5. Phase Noise 24

2.5.1. The importance of phase noise: Spectral skirting and reciprocal mixing 24

2.5.2. Leeson's LTI phase noise equation 26

2.5.3. Hajimiri's linear time-variant phase noise model 28

2.5.4. The simulation of the impulse sensitivity function 31

2.5.5. Impulse sensitivity function of a basic LC oscillator 32

2.5.6. ISF-based phase noise derivation for the basic LC oscillator 39

2.6. Quadrature Considerations 42

3. PROPOSED QVCO ARCHITECTURES AND ANALYSIS 53

3.1. Introduction 53

3.2. The Proposed QVCO Architectures 54

3.3. 2nd Order Simplification of a 4th Order Dual-Resonator Network 56

3.3.1. The Splitting of Inductor L_M 58

3.3.2. The Derivation of the Voltage Ratio (α) 59

3.3.3. The Validity of the Real Voltage Ratio (α) Assumption 60

3.3.4. Circuit Parameter Scaling and Final Reduction 63

3.4. The Resonance Frequency of a Dual-Resonance Oscillator 64

3.5. Effective Quality Factor of Dual-Resonance Oscillator 65

3.6. Startup Condition of the Dual-Resonance Oscillator 68

3.6.1. Nyquist Criterion and Root Locus Method 70

3.7. Phase Noise of the Dual-Mode Resonance Oscillator (high resonance mode) 71

3.7.1. The 2nd Order Simplification of the test circuit 75

3.7.2. Phase noise simulation results 76
3.8. Phase Noise of the Dual-Mode Resonance Oscillator (low resonance mode)....77
3.9. Phase Noise of the Dual-Mode Resonance Oscillator Summary....79
4. THE RESONANCE TANK PASSIVES AND PHASE CHANGE SWITCHING 83
4.1. Introduction....83
4.2. The Inductor....83
4.3. The Tuned Capacitor....84
4.4. Basic LC Tank Design 85
4.5. Quality Factor of the CMOS Switched Capacitor Array 87
4.6. Phase Change Switching....89
4.7. Alternative Tuning Methods' Impact on CMOS Switched Capacitive Tuning....90
5. CIRCUIT DESIGN AND SIMULATIONS 93
5.1. Introduction....93
5.2. Active QVCO Circuit and Simulations....93
5.2.1. Circuit Overview....93
5.2.2. Transformer Design 94
5.2.3. Switch Capacitor Tuning Circuit 99
5.2.4. Complete Dual-Resonance Tank Simulation....101
5.2.5. Startup-Condition....103
5.2.1. Phase noise and phase error 104
5.3. Passive QVCO Circuit and Simulations 106

5.3.1. Circuit Overview 106
5.3.2. The four coupled resonators network 108
5.3.3. Startup-Condition 108
5.3.1. Phase noise and phase error 114
6. CIRCUIT MEASUREMENT 117
6.1. Introduction 117
6.2. Phase Noise Measurement 118
6.2.1. Methodology 118
6.2.2. Direct spectrum power density measurement at oscillation frequency 118
6.2.3. Phase detectors 118
6.2.4. Phase locked loop 119
6.2.5. Delay line frequency discriminator 120
6.2.6. Measurement Setup 121
6.3. Results 123
6.4. Quadrature Phase Measurement 125
6.4.1. Methodology 125
6.4.2. Measurement Setup 130
6.4.3. Results 131
6.5. Overall Performance 132
7. CONCLUSION AND FUTURE WORK 135
References 138

LIST OF FIGURES

FIGURE 1.1: (A) *CONVENTIONAL BASIC LC-TANK VCO AND MODIFIED IN (B) TO IMPLEMENT QUADRATURE IN 3 DIFFERENT ACTIVELY COUPLED ARCHITECTURES.* 2

FIGURE 2.1: *LC OSCILLATOR SYSTEM DIAGRAM* 10

FIGURE 2.2: *IDEAL NONLINEAR NEGATIVE CONDUCTANCE TRANSFER FUNCTION* 12

FIGURE 2.3: (A) *A BASIC RLC OSCILLATOR CONSISTING OF AN RLC RESONANCE TANK AND AN ENERGY COMPENSATING IMPEDANCE* (Z), *AND* (B) *THE SYSTEM REPRESENTATION OF THIS OSCILLATOR* 12

FIGURE 2.4: *VOLTAGE INPUT AND CURRENT OUTPUT WAVEFORMS OF IDEAL NONLINEAR CONDUCTANCE* 13

FIGURE 2.5: *NEGATIVE RESISTANCE REALIZED USING CROSS COUPLED TRANSCONDUCTANCE* 14

FIGURE 2.6: *CONDUCTANCE TRANSFER FUNCTION OF A GENERIC NON-IDEAL NEGATIVE RESISTANCE* 14

FIGURE 2.7: *MODIFICATION OF* (A) *DIFFERENTIAL PAIR NEGATIVE RESISTANCE TO IMPLEMENT* (B) *A NEGATIVE CAPACITANCE USING SOURCE DEGENERATION AND* (C) *THE CORRESPONDING HALF-CIRCUIT SMALL SIGNAL MODEL*.16

FIGURE 2.8: *AN INDUCTIVELY COUPLED RESONATOR* 17

FIGURE 2.9: *(A) CONTOUR OF VALUES OF "S" SWEPT TO GENERATE THE NYQUIST PLOT, AND (B) AN EXAMPLE NYQUIST PLOT WITH GAIN AND PHASE MARGINS MARKED ON THE PLOT* 19

FIGURE 2.10: *CROSS COUPLED OSCILLATOR SCHEMATIC AND EQUIVALENT SMALL SIGNAL CIRCUIT*....19

FIGURE 2.11: *COMPLEX CONJUGATE POLES OF THE LC-TANK VCO IN THE COMPLEX S-PLANE* 21

FIGURE 2.12: *NYQUIST PLOT*....22

FIGURE 2.13: *(A) THE S-PLANE IS SWEPT ALONG THE IMAGINARY AXIS FOR BOTH ROOT LOCUS AND NYQUIST PLOT METHODS AS GIVEN BY EQUATION (2.26), AND (B) THE NYQUIST PLOT THAT CORRESPONDS TO START-UP CONDITION IN EQUATION (2.26) WITH THE IMPLICIT ASSUMPTION THAT* $-G_M Z_0(j\Omega)$ *HAS NO RIGHT HALF PLANE POLES*....23

FIGURE 2.14: *SPECTRAL SKIRTING RESULTING FROM PHASE NOISE CORRUPTING THE DOWN CONVERSION OF A DESIRED RECEIVED SIGNAL BY AN UNDESIRED BLOCKER* 24

FIGURE 2.15: *SIGNAL SPECTRUM AND PHASE SPECTRUM VS. OFFSET FREQUENCY AS WAYS TO DETERMINE PHASE NOISE*...26

FIGURE 2.16: *PHASE NOISE PLOT AS DESCRIBED BY LEESON [17]* 26

FIGURE 2.17: *LC OSCILLATOR EQUIVALENT BASEBAND LTI SYSTEM DIAGRAM* 27

FIGURE 2.18: *CROSS COUPLED LC-OSCILLATOR SCHEMATIC WITH NOISE SOURCES OF INTEREST HIGHLIGHTED* (I_{NQ}, I_{ND}, I_{NT}) 32

FIGURE 2.19: *(A) THE NORMALIZED OUTPUT VOLTAGE WAVEFORM AND THE IMPULSE SENSITIVITY FUNCTION OF THE OUTPUT PHASE TO NOISE INJECTED AT THE THREE NOISE SOURCES (I_{NQ}, I_{ND}, I_{NT}) AS INDICATED IN FIGURE 2.18 AND (B) THE NORMALIZED DRAIN CURRENT AND (C) TRANSCONDUCTANCE OF TRANSISTOR M_0* 33

FIGURE 2.20: *THE STATE-SPACE OF THE SINGLE LC-TANK OSCILLATOR AS DEFINED BY THE VOLTAGE ACROSS THE CAPACITOR (V_C) AND THE CURRENT INSIDE THE INDUCTOR (I_L): A CHARGE INJECTION RESULTS IN A VOLTAGE STEP (ΔV), WHICH CAN CAUSE A PHASE SHIFT ($\Delta\Phi$), WHILE THE OSCILLATION AMPLITUDE EVENTUALLY RETURNS TO V_{C0} LIMITED BY CIRCUIT NONLINEARITIES [18]* 34

FIGURE 2.21: *NORMALIZED PERIODIC OSCILLATING DIFFERENTIAL VOLTAGE* (V_{DIFF}) *AND SWITCHING CURRENT* (I_{DIFF}) *WAVEFORMS CAPTURED BY A HYPERBOLIC TANGENT* (*TANHTANH*) *FUNCTION* 37

FIGURE 2.22: *EFFECTIVE DIFFERENTIAL TRANSCONDUCTANCE* (G_M) AS A FUNCTION OF PHASE, SHOWING HOW AS THE VALUE OF $K=G_{M0}V_0/I_0$ INCREASES, THE TRANSCONDUCTANCE APPROACHES A DIRAC DELTA. 38

FIGURE 2.23: *PHASE NOISE PLOTS FOR CIRCUIT SHOWN IN FIGURE 2.18* 39

FIGURE 2.24: *(A) NMOS AND (B) PMOS BASED CURRENT BIASING CIRCUIT* 41

FIGURE 2.25: *LINEARIZED QUADRATURE LC-TANK OSCILLATOR MODEL* 43

FIGURE 2.26: *QUADRATURE CURRENT PHASORS SUMMING UP AT THE OSCILLATION NODES AND CAUSING A FREQUENCY SHIFT FROM THE NATURAL OSCILLATION FREQUENCY OF THE LC- TANK* 43

FIGURE 2.27: *QUADRATURE LC-OSCILLATOR SCHEMATIC IN LOW RESONANCE MODE WITH NOISE SOURCES OF INTEREST HIGHLIGHTED* (I_{NQ1}, I_{NQ2}) 48

FIGURE 2.28: *PHASE NOISE PLOTS FOR CIRCUIT SHOWN IN FIGURE 2.27* 48

FIGURE 2.29: *VERILOG-A CODE FOR A DIFFERENTIAL TANH-G_M USED TO REPLACE TRANSISTORS IN SIMULATION* 49

FIGURE 2.30: *THE NORMALIZE OUTPUT VOLTAGE WAVEFORM AND THE IMPULSE SENSITIVITY FUNCTION OF THE OUTPUT PHASE TO NOISE INJECTED AT THE NOISE SOURCES INDICATED IN FIGURE 2.27USING VERLIOG-A G_M AS DESCRIBED BY FIGURE 2.29* 50

FIGURE 2.31: *PHASE NOISE PLOTS FOR CIRCUIT SHOWN IN FIGURE 2.27USING VERLIOG-A G_M AS DESCRIBED BY FIGURE 2.29* 50

FIGURE 2.32: *PHASE NOISE SWEEP VERSUS K=I_Q/I_I , FOR CIRCUIT SHOWN IN FIGURE 2.27USING VERLIOG-A G_M AS DESCRIBED BY FIGURE 2.29* 51

FIGURE 3.1: *(A) PASSIVE AND (B) ACTIVE QUADRATURE VOLTAGE CONTROLLED OSCILLATOR ARCHITECTURES WITH DUAL-RESONANCE MODE COUPLED RESONATOR TANKS* 55

FIGURE 3.2: *A COUPLED RESONANCE OSCILLATOR WITH TWO TRANSCONDUCTANCE ELEMENTS FORMING TWO FEEDBACK LOOPS AND THE SYSTEM REPRESENTATION OF THIS CIRCUIT* 55

FIGURE 3.3: (*A*) *EQUIVALENT PI-MODEL OF COUPLED CENTER-TAPPED INDUCTORS, AND* (*B*) *THE CORRESPONDING HALF-CIRCUIT EQUIVALENT MODELS* 56

FIGURE 3.4: *THE COUPLED RESONANCE OSCILLATOR WITH THE MUTUAL INDUCTANCE REPLACED BY THE DIFFERENTIAL PI-MODEL* 57

FIGURE 3.5: *THE SPLITTING OF A 2-TERMINAL INDUCTANCE INTO TWO SINGLE TERMINAL INDUCTANCES BY EQUATING IMPEDANCES* Z_1 *AND* Z_2 58

FIGURE 3.6: *THE COUPLED RESONANCE OSCILLATOR'S PI MODEL BROKEN INTO TWO PARTS FOR A GIVEN VOLTAGE RATIO A* 59

FIGURE 3.7: *A PLOT OF THE VOLTAGE SWING RATIO AT THE TWO NODES OF THE COUPLED RESONANCE OSCILLATOR AS A FUNCTION OF THE RATIO OF THE RESONANCE FREQUENCIES OF THE TWO RESONATORS PRIOR TO COUPLING* (*Z*) *FOR 5 MUTUAL COUPLING FACTORS* (*K*) 60

FIGURE 3.8: *THE TEST STRUCTURE FOR VALIDATING THE REAL VOLTAGE RATIO* (*A*) *ASSUMPTION* 60

FIGURE 3.9: *THE PHASE OF THE VOLTAGE RATIO* (*A*) *VS FREQUENCY FOR Q=10, 100, 1000 AND COUPLING FACTOR K=0.5. EACH PLOT CONSIDERS THREE FREQUENCY RATIOS Z, AND THE RESONANCE FREQUENCIES ARE MARKED* 61

FIGURE 3.10: *THE* (*A*) *MAGNITUDE AND* (*B*) *PHASE OF THE VOLTAGE RATIO* (*A*) *AT RESONANCE VS FREQUENCY RATIOS Z FREQUENCY FOR Q=10, 20,100, 1000 AND COUPLING FACTOR K=0.5. THE PLOT MARKED EXPRESSION IS THE PLOT OF THE A AS DERIVED IN EQUATION* (*3.4*) 61

FIGURE 3.11: *THE PHASE OF THE VOLTAGE RATIO* (*A*) *VS FREQUENCY FOR Q=10, 100, 1000 AND COUPLING FACTOR K=0.3. EACH PLOT CONSIDERS THREE FREQUENCY RATIOS Z, AND THE RESONANCE FREQUENCIES ARE MARKED* 62

FIGURE 3.12: *THE* (*A*) *MAGNITUDE AND* (*B*) *PHASE OF THE VOLTAGE RATIO* (*A*) *AT RESONANCE VS FREQUENCY RATIOS Z FREQUENCY FOR Q=10, 20,100, 1000 AND COUPLING FACTOR K=0.3. THE PLOT MARKED EXPRESSION IS THE PLOT OF THE A AS DERIVED IN EQUATION* (*3.4*) 62

FIGURE 3.13: *THE SECOND ORDER RESONATOR REPRESENTATION OF THE FOURTH ORDER COUPLED RESONATOR* 63

FIGURE 3.14: *THE SECOND ORDER RESONATOR REPRESENTATION OF THE FOURTH ORDER SYMMETRIC COUPLED RESONATOR* (*CONSISTING OF TWO IDENTICAL RESONATORS COUPLED*).....64

FIGURE 3.15: *THE RATIO OF THE OF THE COUPLED RESONATOR'S RESONANCE FREQUENCIES TO THE UNCOUPLED RESONANCE FREQUENCY* ($\Omega_{1,2}$) *VERSUS THE MUTUAL COUPLING FACTORS* (*K*) *FOR A 6 RATIOS OF THE UNCOUPLED RESONANCE* ($Z = \Omega_2/\Omega_1$).....65

FIGURE 3.16: *THE DERIVATION OF THE LUMPED PARALLEL RESISTANCE R OF A SYMMETRIC COUPLED RESONATOR FROM THE PARASITIC SERIES RESISTANCE OF THE INDUCTORS AND CAPACITORS.* 66

FIGURE 3.17: *THE RATIO OF THE QUALITY FACTOR OF A COUPLED RESONATOR CONSISTING OF TWO IDENTICAL INDUCTORS TUNED DIFFERENTLY* (*Z*) *TO THE ORIGINAL QUALITY FACTOR OF THE INDUCTORS WHEN THE COUPLED RESONATOR'S QUALITY FACTOR IS DOMINATED BY THAT OF THE INDUCTORS*.....68

FIGURE 3.18: *DECOMPOSING THE DUAL-RESONANCE OSCILLATOR INTO TWO CIRCUITS THAT CAN BE LINEARLY SUPERPOSED, NAMELY:* (*A*)*THE TWO TERMINAL NEGATIVE FEEDBACK LOOP AND* (*B*) *THE SINGLE TERMINAL NEGATIVE GM LOOP*.....69

FIGURE 3.19: *SYSTEM REPRESENTATION OF THE LINEAR DECOMPOSITION WHERE THE Z-PARAMETERS* (Z_{11},Z_{21}) *ARE DESCRIBED IN* FIGURE 3.2 69

FIGURE 3.20: *DUAL RESONANCE CROSS COUPLED LC-OSCILLATOR SCHEMATIC IN HIGH RESONANCE MODE WITH NOISE SOURCES OF INTEREST HIGHLIGHTED* (I_{NQ1}, I_{ND1}, $I_{NT1,}$ I_{NQ2}, I_{ND2}, I_{NT2}).....72

FIGURE 3.21: (*A*) *THE NORMALIZE OUTPUT VOLTAGE WAVEFORM AND THE IMPULSE SENSITIVITY FUNCTION OF THE OUTPUT PHASE TO NOISE INJECTED AT THE NOISE SOURCES INDICATED IN FIGURE 3.20* , (*B*) *THE NORMALIZED DRAIN CURRENT OF THE TRANSISTOR* M_0 *AND* (*C*) *THE CORRESPONDING TRANSCONDUCTANCE* G_M 73

FIGURE 3.22: *REDUCED MODEL OF THE DUAL-RESONANCE CROSS COUPLED LC-OSCILLATOR SCHEMATIC* 75

FIGURE 3.23: *PHASE NOISE PLOTS FOR CIRCUIT SHOWN IN FIGURE 3.20* 76

FIGURE 3.24: *DUAL RESONANCE CROSS COUPLED LC-OSCILLATOR SCHEMATIC IN LOW RESONANCE MODE WITH NOISE SOURCES OF INTEREST HIGHLIGHTED* (I_{NQ1}, I_{ND1}, $I_{NT1,}$ I_{NQ2}, I_{ND2}, I_{NT2}).....77

FIGURE 3.25: *THE NORMALIZE OUTPUT VOLTAGE WAVEFORM AND THE IMPULSE SENSITIVITY FUNCTION OF THE OUTPUT PHASE TO NOISE INJECTED AT THE NOISE SOURCES INDICATED IN FIGURE 3.24* 78

FIGURE 3.26: *PHASE NOISE PLOTS FOR CIRCUIT SHOWN IN FIGURE 3.24* 78

FIGURE 3.27: *PHASE NOISE COMPARISON OF THE CAPACITOR QUALITY FACTOR DOMINATED RESONATOR (PN_{RSC}) AND THE INDUCTANCE QUALITY FACTOR DOMINATED RESONATOR (PN_{RSL}) IN SINGLE LC-TANK VCO AND DUAL MODE RESONANCE IN HIGH FREQUENCY MODE (DR_H) AND LOW FREQUENCY MODE (DR_L)* 82

FIGURE 4.1*: (A) MAXIMUM $Q_L^3(\Omega_0)L$ FOR A NUMBER OF INDUCTOR CONFIGURATIONS IN THE 65 NM CMOS PROCESS NORMALIZED AND PLOTTED AGAINST THE MAXIMUM Q_L FREQUENCY AND (B) THE NORMALIZED PHASE NOISE TERM $\Omega_0/Q_L^3(\Omega_0)$ L PLOTTED AGAINST THE RESONANT FREQUENCY (Ω_0)* 84

FIGURE 4.2: *A BASIC LC TANK THAT CONSISTS OF A FIXED INDUCTOR (L), A TUNING VARACTOR WITH CAPACITANCE RANGING FROM C_{VMIN} TO C_{VMAX} AND A SWITCHED CAPACITOR ARRAY CONSISTING OF N IDENTICAL INSTANCES OF EQUAL UNIT CAPACITANCE (C_U)* 84

FIGURE 4.3: (A) *SWITCHED CAPACITOR ARRAY WITH PARASITIC FIXED CAPACITANCE (C_F), M ON BRANCHES AND N-M OFF BRANCHES OF UNIT CAPACITANCE (C_U) AND (B) THE EQUIVALENT MODEL OF THE SWITCHED CAPACITOR ARRAY WITH CMOS SWITCH PARASITIC ON-RESISTANCE (R_{ON}) AND OFF-CAPACITANCE (C_P) CONSIDERED* 85

FIGURE 4.4: *TUNING RANGE AS A FUNCTION OF THE SWITCHED CAPACITOR ARRAY'S B(THE RATIO OF MAX TO MIN TUNING CAPACITANCES) AT A RANGE OF X_N VALUES (THE RATIO OF THE FIXED CAPACITANCE TO THE TOTAL CAPACITANCE)* ..86

FIGURE 4.5: *NORMALIZED QUALITY FACTOR AS A FUNCTION OF NORMALIZED RESONANT FREQUENCY (Ω_R), AS TUNING RANGE (TR) AND FIXED TO MAXIMUM TOTAL CAPACITANCE RATIO (X_N) ARE VARIED.* 88

FIGURE 4.6: *PHASE-CHANGED SWITCHED CAPACITOR BRANCH AND ITS CIRCUIT MODEL.* 89

FIGURE 4.7: *NORMALIZED QUALITY FACTOR (TERMS BXC) DEMONSTRATING Q IMPROVEMENT FROM (A) TR REDUCTION (X_N=0.1) , (B) TR REDUCTION WITH X_N SCALED BY A FACTOR OF $(TR_{ORIGINAL}/TR_{FINAL})^2$ (X_N:0.1→ 0.2) AND (C) TR REDUCTION ASSOCIATE WITH P-C SWITCH (X_N=0.1 → [0.2,0.5] FOR [HIGH, LOW] SUB-BANDS RESPECTIVELY)*.....91

FIGURE 4.8: *IMPROVEMENT IN CMOS SWITCHED CAPACITOR TANK'S MINIMUM QUALITY FACTOR AS A FUNCTION OF TUNING RANGE (X_{NORIG}= 0.1)* 92

FIGURE 5.1: *ACTIVE QUADRATURE VOLTAGE CONTROLLED OSCILLATOR ARCHITECTURES WITH DUAL RESONANCE MODE COUPLED RESONATOR TANKS*.....93

FIGURE 5.2: *CIRCUIT SCHEMATIC OF THE PMOS CURRENT MIRROR USED FOR THE BIASING OF THE VCO*.....94

FIGURE 5.3: *MUTUAL INDUCTOR LAYOUT AND DIMENSIONS*.....95

FIGURE 5.4: *LUMPED ELEMENT MODEL OF INTEGRATED CIRCUIT MUTUAL INDUCTOR*.....95

FIGURE 5.5: *HALF CIRCUIT OF REDUCED CENTER-TAPPED MUTUAL INDUCTOR MODEL*.....96

FIGURE 5.6: (*A*) *SINGLE-ENDED AND* (*B*) *DIFFERENTIALLY DRIVEN MUTUAL INDUCTOR* 96

FIGURE 5.7: (A) *Y-PARAMETER REPRESENTATION OF THE 4-PORT MUTUAL INDUCTOR AND ITS REDUCTION TO* (*B*) *THEN TO* (*C*) 97

FIGURE 5.8: *MUTUAL INDUCTOR* (*A*) *INDUCTANCE,* (*B*) *COUPLING FACTOR AND* (*C*) *DIFFERENTIAL QUALITY FACTOR* 98

FIGURE 5.9: *CIRCUIT SCHEMATICS OF THE SWITCHED CAPACITOR ARRAY SHOWING DEVICES SIZES AND APPROXIMATE UNIT CAPACITANCE.* 99

FIGURE 5.10: (*A*) *SINGLE-ENDED AND* (*B*) *DIFFERENTIALLY DRIVEN CAPACITOR* 99

FIGURE 5.11: *SWITCHED CAPACITOR ARRAY'S* (*A*) *CAPACITANCE AND* (*B*) *QUALITY FACTOR ACROSS THE TUNING RANGE FOR A LAYOUT BASED SIMULATIONS* 100

FIGURE 5.12: *PASSIVE QUADRATURE VOLTAGE CONTROLLED OSCILLATOR ARCHITECTURES WITH DUAL RESONANCE MODE COUPLED RESONATOR TANKS* 101

FIGURE 5.13: (*A*) *SINGLE-ENDED AND* (*B*) *DIFFERENTIALLY DRIVEN CAPACITOR* 102

FIGURE 5.14: *OVERALL TANK QUALITY FACTOR AT RESONANCE ASSUMING A 100FF ADDITIONAL FIXED CAPACITANCE* 103

FIGURE 5.15: *ACTIVE QUADRATURE VOLTAGE CONTROLLED OSCILLATOR* 2^{ND} *ORDER EQUIVALENT CIRCUIT* 104

FIGURE 5.16: *PHASE NOISE SWEEP VERSUS* $K=I_Q/I_1$ *, FOR DUAL-RESONANCE QVCO, EQUIVALENT* 2^{ND} *ORDER QVCO AND THE THEORETICAL EXPRESSION FOR PHASE NOISE WITH CIRCUITS SIMULATED USING VERLIOG-A* G_M *AS DESCRIBED BY FIGURE 2.29* 105

FIGURE 5.17: *PASSIVE QUADRATURE VOLTAGE CONTROLLED OSCILLATOR ARCHITECTURES WITH DUAL RESONANCE MODE COUPLED RESONATOR TANKS* 107

FIGURE 5.18: *CIRCUIT SCHEMATIC OF THE PMOS CURRENT MIRROR USED FOR THE BIASING OF THE VCO* 107

FIGURE 5.19: *LAYOUT AND DIMENSIONS OF THE FOUR COUPLED RESONATORS WITH CAPACITANCE PLACEMENT INDICATED BY ARROWS* 108

FIGURE 5.20: *PASSIVE NETWORK CORRESPONDING TO THE PASSIVE QUADRATURE VOLTAGE CONTROLLED OSCILLATOR* 109

FIGURE 5.21: *TUNING RANGE OF THE PQVCO PASSIVE NETWORK GIVEN BY* Ω_H/Ω_L *VERSUS THE COUPLING FACTOR* (*K*) *FOR MULTIPLE VALUES OF* A *COMPARED TO THAT OF THE AQVCO* 110

FIGURE 5.22: *PASSIVE NETWORK CORRESPONDING TO THE PASSIVE QUADRATURE VOLTAGE CONTROLLED OSCILLATOR WITH THE SERIES RESISTANCE* (R_S) *CONSIDERED* 111

FIGURE 5.23: *THE RATIO OF THE QUALITY FACTOR IN THE HIGH RESONANCE MODE TO THAT IN THE LOW RESONANCE MODE AS A FUNCTION OF THE TUNING RANGE GIVEN BY THE FREQUENCY RATIO OF THE HIGH RESONANCE MODE TO THE LOW RESONANCE MODE FOR AQVCO AND PQVCO WITH MULTIPLE VALUES OF A* 112

FIGURE 5.24: *THE RATIO OF THE QUALITY FACTOR IN THE HIGH RESONANCE MODE TO THE QUALITY FACTOR OF THE INDUCTOR AT THE SAME FREQUENCY AS A FUNCTION OF THE TUNING RANGE GIVEN BY THE FREQUENCY RATIO OF THE HIGH RESONANCE MODE TO THE LOW RESONANCE MODE FOR AQVCO AND PQVCO WITH MULTIPLE VALUES OF A* 113

FIGURE 5.25: *PASSIVE QUADRATURE VOLTAGE CONTROLLED OSCILLATOR 2ND ORDER EQUIVALENT CIRCUIT* 114

FIGURE 5.26: *PHASE NOISE PLOTS FOR PASSIVE DUAL-RESONANCE QVCO* 115

FIGURE 5.27: *QUADRATURE PHASE ERROR VERSUS MISMATCH IN (A) RESONANCE FREQUENCY , (B) TANK RESISTANCE AND (C) BIAS CURRENT OF THE TWO DUAL-RESONANCE CORES IN THE CASE OF AQVCO (Q=15, AND K=0.25) AND PQVCO WITH A=0.5,1,2* 116

FIGURE 6.1: *DIE PHOTO OF (A) ACTIVE COUPLED QVCO AND (B) PASSIVE COUPLED QVCO* 117

FIGURE 6.2:*MIXER AND LOW PASS FILTER AS SIMPLE PHASE DETECTOR*.....119

FIGURE 6.3: *FIRST ORDER PLL AS A PHASE NOISE MEASUREMENT SETUP* 119

FIGURE 6.4: *DELAY LINE DISCRIMINATOR AS A PHASE NOISE MEASUREMENT SETUP* 120

FIGURE 6.5: *E5052B SIGNAL SOURCE ANALYZER CONNECTED TO E5053A MICROWAVE DOWN-CONVERTER* [29] 122

FIGURE 6.6: *RAW COLLECTED PHASE NOISE DATA FOR (A) ACTIVE COUPLED QVCO AND (B) PASSIVE COUPLED QVCO FOR OFFSET FREQUENCIES RANGING FROM 1 KHZ TO 10MHZ SUPERPOSED FOR MULTIPLE FREQUENCY POINTS COLLECTED OVER THE FULL TUNING RANGE OF EACH QVCO*.....123

FIGURE 6.7: *PHASE NOISE MEASURED FOR (A) ACTIVE COUPLED QVCO AND (B) PASSIVE COUPLED QVCO AT AN OFFSET FREQUENCY OF 1MHZ COLLECTED OVER THE FULL TUNING RANGE OF EACH QVCO, WITH CURRENT CONSUMPTION OF THE QVCO NOTED FOR EACH ARRANGEMENT OVER DIFFERENT FREQUENCY RANGES THAT WAS USED IN THE MEASUREMENT*.....124

FIGURE 6.8: *QUADRATURE UPCONVERSION ARCHITECTURE USED IN QUADRATURE PHASE ACCURACY MEASUREMENT CONSIDERING DIFFERENT CIRCUIT NON-IDEALITIES THAT REQUIRE TO BE MEASURED/CALIBRATED* (A_I, A_Q, Φ_{IFE}, Φ_R) 125

FIGURE 6.9: *IMAGE REJECTION OF A QUADRATURE UP/DOWN CONVERTER AS A FUNCTION OF PHASE ERROR AND I/Q CHANNELS GAIN MISMATCHES* 127

FIGURE 6.10: (*A*) *MAXIMUM IMAGE REJECTION* R_{PMAX} *AS A FUNCTION OF MAXIMUM IMAGE REJECTION ANGLE* (Φ_{IFPMAX}), *PHASE ERROR* (Φ_E) *AND SMALL SIGNAL APPROXIMATION* (*GIVEN BY*(*6.10*)) *FOR THREE DIFFERENT AMPLITUDE IMBALANCE VALUES* (*A=0.5,0.7,0.9*). (*B*) *PHASE ESTIMATION ERROR CONTOURS* ($\Phi_E - \Phi_{IFPMAX}$) *OF THE MAXIMUM IMAGE REJECTION* R_{PMAX} *AS A FUNCTION OF MAXIMUM IMAGE REJECTION ANGLE* (Φ_{IFPMAX}) *PLOT* 129

FIGURE 6.11: *QUADRATURE UPCONVERSION MEASUREMENT SETUP PICTURE WITH PARTS AND TEST EQUIPMENT MARKED* 130

FIGURE 6.12: *RAW COLLECTED IMAGE REJECTION VS. IF PHASE SWEEP DATA FOR* (*A*) *ACTIVE COUPLED QVCO AND* (*B*) *PASSIVE COUPLED QVCO WITH PHASE ESTIMATION ERROR CONTOURS GIVEN IN FIGURE 6.10* (*B*) *MARKED ON EACH PLOT* 131

FIGURE 6.13: *PHASE ERRORS OF* (*A*) *ACTIVE COUPLED QVCO AND* (*B*) *PASSIVE COUPLED QVCO CALCULATED AS THE MAXIMUM IMAGE REJECTION ANGLE IN THE PHASE SWEEPS PRESENTED IN FIGURE 6.12* 132

FIGURE 6.14: FOM_{PN}, FOM_T *AND* FOM_{T2} *OF THE* (*A*) *ACTIVE COUPLED QVCO AND* (*B*) *PASSIVE COUPLED QVCO EVALUATED FOR AN OFFSET FREQUENCY OF 1MHZ OVER THE FULL TUNING RANGE* 133

LIST OF TABLES

TABLE 1: *PHASE NOISE EVALUATED FOR THE LC-TANK AT 10KHZ, 1MHZ FOR A NUMBER OF CASES*.....41

TABLE 2: *PHASE NOISE EVALUATED FOR THE QUADRATURE LC-TANK AT 1MHZ*.....49

TABLE 3: *PHASE NOISE EVALUATED FOR THE QUADRATURE LC-TANK AT 1MHZ USING VERLIOG-A G_M DESCRIBED BY FIGURE 2.29*.....51

TABLE 4: *PHASE NOISE EVALUATED FOR THE LC-TANK AT 10KHZ, 1MHZ FOR A NUMBER OF CASES FOR DUAL-RESONANCE CIRCUIT*.....76

TABLE 5: *PHASE NOISE EVALUATED FOR THE LC-TANK AT 10KHZ, 1MHZ FOR A NUMBER OF CASES FOR DUAL-RESONANCE CIRCUIT*.....79

TABLE 6: *PHASE NOISE EVALUATED FOR INDUCTOR AND CAPACITOR QUALITY FACTOR DOMINATED LC-TANK, LOW AND HIGH MODE DUAL-RESONANCE VCOS AT 1MHZ*.....82

TABLE 7: *IMPACT OF ALTERNATIVE TUNING METHODS ON CMOS SWITCHED CAPACITIVE TUNING PARAMETERS*.....91

TABLE 8: *PERFORMANCE COMPARISON WITH STATE-OF-ART WIDEBAND VCO DESIGNS*.....134

Chapter 1
INTRODUCTION

1.1. Background

Reconfigurable RF circuits are important for implementing multi-standard radios and cognitive radios. Multi-standard radios allow for higher integration in end-user products such as cell phones and tablets. Higher integration can save power, area and cost, while cognitive radio enables a more efficient use of the spectrum.

High-quality, wide-tuning quadrature voltage controlled oscillators (QVCOs) are necessary to provide the local oscillator (LO) signal for up and down conversion in multi-standard and cognitive radios.

LC-tank voltage controlled oscillators have become one of the most popular oscillators for signal generation in CMOS integrated RF transceivers. This is attributed to their simple design, start-up conditions and competitive phase noise performance. It has been shown that they outperform differential Colpitts in phase noise performance for a given power consumption and swing specs [1]. However, LC-tank oscillators suffer more significantly from the impact of parasitic capacitances that limit their tuning range and dominate at high frequencies.

Quadrature signal generation has become an integral part of modern transceivers. Quadrature down conversion is necessary in direct conversion receivers, and for image rejection in full integrated heterodyne receivers. This has driven significant innovation in quadrature generation circuits.

Quadrature techniques, ranging from passive hybrid couplers and poly-phase filters to active master-slave flip-flop divide-by-2 circuits, have been used to obtain quadrature. Quadrature couplers suffer from their relatively large size factor, which scales down with frequency.

Quadrature poly-phase filters suffer from delay mismatches and narrow frequency selectivity, which can be tuned and calibrated with additional overhead. On the other hand, quadrature dividers provide accurate wideband I/Q generation, with a small size factor. However, they consume more power than the aforementioned techniques because they require an oscillator operating at twice the desired frequency, and an active divider.

Alternatively, active quadrature VCO oscillators have been widely used to produce quadrature by coupling two voltage controlled oscillators using a quadrature loop. However, these architectures suffer from increased phase noises due to:

1) Frequency shift away from resonance, increasing the losses of the tank[2]
2) AM to PM noise modulation due to quadrature [3]
3) Additional noise induced by the active transistors used to obtain quadrature

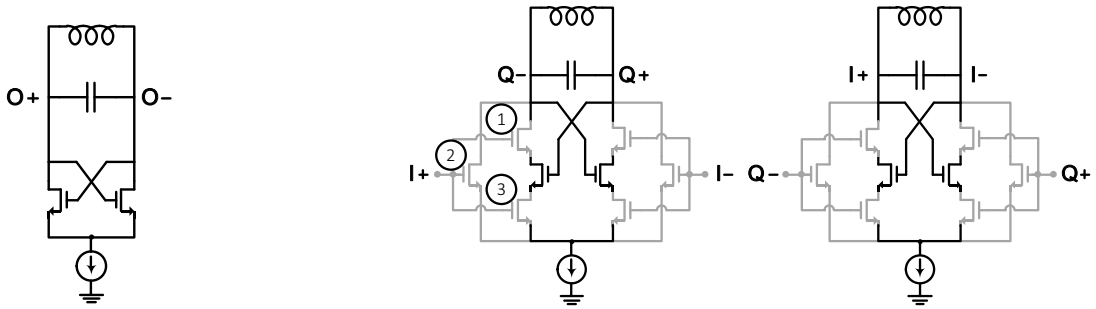

(a) (b)

Figure 1.1: (*a*) *Conventional basic LC-tank VCO and modified in (b) to implement quadrature in 3 different actively coupled architectures.*

Three such architecture were compared in [4], which are presented in Figure **1.1** (b). The architectures trade off coupling strength for improved phase noise. The paper shows an advantage to using architectures (1) and (2) due to current sharing between the oscillation and quadrature transistors which leads to reduced noise contribution from the additional transistors.

However, at higher frequencies, parasitic nodes can present significantly low impedances creating parallel noise paths and rendering these architectures less beneficial.

To alleviate limited tuning range and active quadrature disadvantages, passive circuit techniques have been deployed: dual/multi-resonance mode resonators and passive quadrature coupling respectively. Over the last 10 years these techniques have evolved separately and more recently a number of works have deployed both techniques to achieve widest tuning range possible for quadrature oscillators.

Dual-resonance is the technique by which a coupled resonator is used as the passive load of a VCO. In LC-tank VCOs, frequency tuning is commonly achieved by tuning the capacitive component of the tank. The range of capacitive tuning is limited by technology, parasitics, and the required quality factor. Dual-resonance increases the tuning range by using the same capacitive tuning to tune the resonator at two different resonance modes, corresponding to two different frequency ranges. An extended tuning range is achieved by selecting two overlapping frequencies ranges. Since coupled resonators are often based on a coupled inductor, it's possible to implement such structures with little area overhead, but with added complexity.

One of the earlier works to apply dual-resonance to VCOs is presented in [5]. Two principle circuit topologies were discussed: one and two port oscillation. While one port oscillation requires resonator's asymmetry to do mode switching, the two port structure uses active feedback to pick the resonance mode for symmetric and asymmetric resonators. A later work that used these principles in a quadrature VCO was presented in [6]. This work used asymmetry in the coupled resonator's tuning in order to implement mode switching. It also used active parallel quadrature coupling in order to implement quadrature. A further expansion on the original work was presented in[7], in which additional control was added by tuning the capacitive coupling

between the two resonators in an attempt to equate the impedance magnitudes of the passive network in both operating modes.

Passive quadrature coupling is a technique to obtain quadrature without the use of active devices. It's based on building VCOs around passive resonance architectures that inherently provides 90^{o} phase shift.

One of the earliest passive quadrature coupling works was presented in [8] in which two VCOs were coupled using two transformers. Other passive quadrature coupling structures have relied on capacitive coupling. In [9], capacitive coupling of the second harmonics of the outputs of two VCOs is used to generate quadrature. This theory was further investigated in [10], in which a study of phase error vs. nonlinearity was performed and better quadrature phase accuracy was obtained using bi-directional nonlinear switches in series with the capacitive coupling.

Passive quadrature coupling can also be implemented by designing the passive network to provide quadrature. This can be thought of as a tunable poly-phase oscillator. An early example of this was presented in [11]. This work can be considered an extension on the design in [8] with explicit analysis of phase noise, noise figure and phase error for a transformer coupled quadrature oscillator. Similar to [8], it presents no multi-mode resonance tuning.

More recently, similar passive structures have been extended to also support dual-resonance mode. In [12], such a structure was implemented using four capacitive coupled LC resonator tanks. In [13] and [14], the four separate resonators were replaced with two coupled resonators and they again employed capacitive coupling in the quadrature loop. While these works provided performances comparable to that of stand-alone VCOs, with enhanced tuning ranges, they employed relatively complex active device structures to control mode selection, and they focused

mainly on low frequencies at which the inductances dominate the quality factors of the resonance tanks.

1.2. Thesis Contribution and Organization

This work extends the state-of-the-art by demonstrating two quadrature oscillators: a) an active-quadrature, dual-resonance, symmetric-resonator oscillator with a less complex mode selection technique compared to [13] and [14] and b) a passively coupled quadrature, dual-resonance oscillator that employs four coupled resonators.

Both architectures make use of the same elementary passive devices. They combine several tuning methods including dual-resonance and switched capacitive tuning in order to minimize phase-noise while achieving wideband tuning. Theoretical analyses and simulations indicate significantly lower phase noise of the passively coupled QVCO at higher frequencies compared to the actively coupled QVCO. This thesis aims to provide design insights into these architectures, and validates these insights through the design and measurement of circuit prototypes in 65 nm CMOS. The specific contributions of this thesis are:

A. Circuit Contributions:

1) Proposing two novel wide-tuning quadrature voltage controlled oscillator architectures that use coupled resonators capable of dual-resonance operation to maximize the tuning range, and tuning them using simple and robust frequency selection techniques. The topologies use active transistors and passive coupled inductors to achieve quadrature.
2) The fabrication and characterization of the aforementioned circuits and the comparison of their performance to the state-of-art presented in the literature.

3) The novel use of phase change switches as an alternative to CMOS switches in switch capacitor tanks, leading to an improved capacitor bank quality factor for a given tuning range.

B. Analytical and Theoretical Contributions:

1) Providing an in depth analysis of the dual-resonance small signal modeling. This is achieved by using equivalent representations of coupled resonators that allow for reducing the complex circuits into the more familiar second order circuits, which allows for deriving all the derivation of familiar second-order circuit attributes such as quality factor of a coupled resonator and startup conditions and simple phase noise analysis.
2) Understating the dual-resonance large signal linear time variant (LTV) behavior using impulse sensitivity function to study the impact of different passive and active device noises on the overall phase noise performance and using that in combination with the (LTV) phase noise model to derive overall phase noise of the dual-resonance oscillator.
3) Extending the previous analysis the two proposed quadrature architectures and using that to compare and contrast the advantages of the two, showing the superior phase noise performance of the passive structure.
4) Analyzing the quadrature phase error due to the different architecture parameters.
5) Quantifying the possible improvement in capacitor bank's quality factor with the use of phase change switches in place of CMOS switches, and highlighting the importance of pursuing phase change switch integration into a CMOS process.

C. Measurement Methods Contributions:

1) Describing a novel method for accurate off chip phase error measurement using discrete components and phase shifters, which requires no calibration and can readily provide

phase error results with no processing using developed phase error measurement accuracy plots.

The thesis is organized in 5 chapters. In addition to the introduction the thesis is broken up into the following chapters:

- *Chapter 2 provides background material into the operation of wide tuning QVCOs*. It analyzes a basic LC-oscillator, presenting the concepts of oscillation, startup, phase noise and its different models and quadrature. Each subject is explored with a number of examples as a basis for further investigation of the two advanced QVCO architectures.
- *Chapter 3 describes the two proposed QVCO architectures*, namely the active and passive coupled dual-resonance quadrature VCOs. This chapter extends the analysis presented in the Chapter 1 to the dual-resonance oscillator and the two QVCO architectures providing a complete analysis including equivalent tank quality factors, startup conditions, phase noise and phase noise contributors as described by impulse sensitivity functions (ISFs). Additionally, the chapter presents the analysis of the phase error of the passive and active QVCOs as a function of multiple circuit non-idealities.
- *Chapter 4 focuses on the optimization of the design of passive resonators and the advantages of using Phase Change switching as part of this design.* It studies the trade-off between quality factor and tuning range for a number of passive tuning components. The chapter identifies the advantages of using switched capacitor tuning as a major part of passive tuning, and expresses the quality factor of such arrangement in terms of the bandwidth of the used switch. This quantifies the advantage of using switches with large bandwidths, such as those associated with phase change material switches.

- *Chapter 5 presents the fabricated devices and their measurement results*. It describes the methods used for obtaining the performance metrics, namely phase noise, tuning range, power consumption and quadrature phase error and presents the measurement results for each. A comparison with state-of-art circuits is presented based on the aforementioned performance metrics and the figure of merits (FOMs) derived based on them.

Chapter 2

WIDE-BAND TUNING QVCOS BACKGROUND

2.1. Introduction

This chapter introduces the fundamental concepts needed to study a quadrature voltage controlled oscillator. The chapter introduces the concept of oscillation and its numerous mathematical representations, in both nonlinear and linearized forms, based on an *LC*-tank oscillator. The chapter used the *LC*-tank oscillator to demonstrate the concepts of (1) start-up, (2) phase noise and (3) quadrature. It also briefly discusses non-conventional methods that were used in the literature to expand the tuning range of VCOs, namely multi-mode resonance and capacitive degeneration.

In examining the start-up condition, three methods are considered: Barkhausen's criterion, root locus method, and Nyquist stability criterion. The methods are described as three ways to determine the conditions required to obtain and maintain an oscillation. These concepts are applied to the *LC*-tank oscillator.

In examining phase noise, the general concept of phase noise is introduced and defined, and the motivation for quantifying phase noise is expressed. The linear time variant method of studying phase noise is explained and the corresponding concept of impulse sensitivity function as a method of understanding the different contributors to phase noise is applied to the *LC*-tank oscillator.

2.2. Voltage Controlled Oscillator (VCO) Basics

Oscillation is the process in which a conserved amount of energy is transformed indefinitely from one form to another at a fixed rate. Oscillation can be observed in many types of systems.

In electric circuits, oscillation can be realized by an *LC* resonator, which transforms energy between electric energy stored in a capacitor (*C*) and magnetic energy stored in an inductor (*L*). An ideal lossless resonator can oscillate indefinitely once excited with an initial current or voltage.

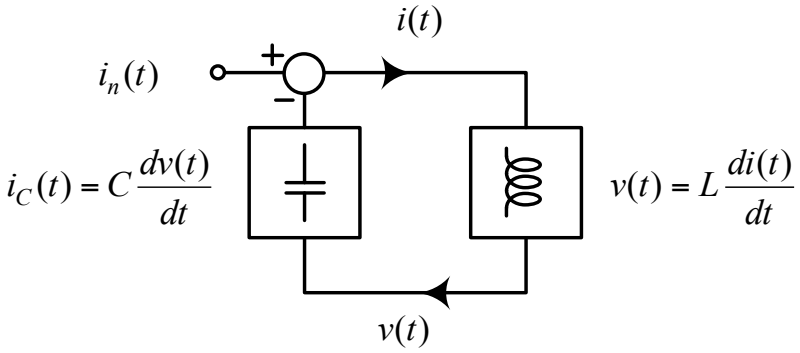

Figure 2.1: *LC oscillator system diagram*

Considering the lossless LC resonator in Figure **2.1**, the differential equation representing this system and the general solution of the differential equation are given by equations (2.1) and (2.2), respectively.

$$i(t) + LC\frac{d^2 i(t)}{dt^2} - i_n(t) = 0 \tag{2.1}$$

$$i(t) = C_0 \cos(\omega_0 t) + C_1 \sin(\omega_0 t) + i_P(t) \tag{2.2}$$

where ω_0 is the oscillation frequency($\frac{1}{\sqrt{LC}}$), C_0 and C_1 are constants given by the initial voltage and current conditions in the circuit and $i_P(t)$ is the particular solution of the differential equation for the given input $i_n(t)$, which is equal to 0 for no input.

Due to energy dissipated due to resistive losses, oscillation requires the periodic addition energy from external source in order to compensate for the dissipated energy. If a loss is introduced in the system in Figure **2.1** by adding a series resistor, the system's differential equation becomes:

$$i(t) + LC\frac{d^2I(t)}{dt^2} + RC\frac{dI(t)}{dt} - i_n(t) = 0 \tag{2.3}$$

The homogenous solution of this differential equation is given by:

$$i(t) = \left(C_0 e^{\sqrt{-\omega_0^2 + \left(\frac{R}{2L}\right)^2}\,t} + C_1 e^{-\sqrt{-\omega_0^2 + \left(\frac{R}{2L}\right)^2}\,t} \right) e^{\frac{-R}{2L}t} \tag{2.4}$$

Equation (2.4) describes a damped system that decays to zero. In order to obtain oscillation, the system requires an active component which can provide periodic energy precisely equal to the energy dissipated in resistance.

This can be achieved by a negative resistance, an element that can provide energy to the circuit. In simple terms, if one were to cancel out the positive resistance of the LC tank with a negative resistance of the same magnitude, then the overall circuit resistance will be zero. This is described in equation (2.5), by adding a negative resistance (R_N) to the aforementioned equation, and equating to the positive resistance (R).

$$i(t) + LC\frac{d^2I(t)}{dt^2} + (R - R_N)C\frac{dI(t)}{dt} - i_n(t) = 0 \tag{2.5}$$

However, if the negative resistance (R_N) exceeds in magnitude the positive resistance (R), the homogenous solution to the differential equation becomes an exponentially growing oscillation as described by:

$$i(t) = \left(C_0 e^{\sqrt{-\omega_0^2 + \left(\frac{R_N - R}{2L}\right)^2}\,t} + C_1 e^{-\sqrt{-\omega_0^2 + \left(\frac{R_N - R}{2L}\right)^2}\,t} \right) e^{\frac{R_N - R}{2L}t} \tag{2.6}$$

While oscillation can be theoretically achieved by linear circuit elements as described in the previous equations, the amplitude of such oscillation is dependent on the initial circuit

conditions, and unless resistance is cancelled precisely, the oscillation will either exponentially decay or exponentially grow.

In practical circuits, fixed oscillation amplitude is needed. In order to achieve that, electric oscillators exploit nonlinearity associated with active circuit components used to implement the negative resistance. An ideal example of such nonlinear negative resistance can be expressed by its conductance transfer function $i_{OUT} = -i_0 sign(v_{IN})$, which is shown in Figure **2.2**.

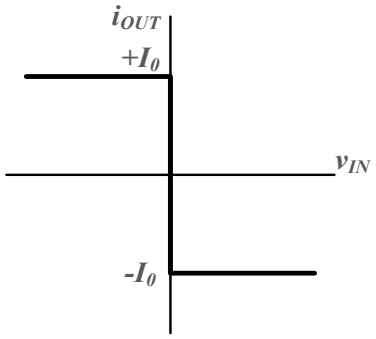

Figure 2.2: *Ideal nonlinear negative conductance transfer function*

An oscillation can be formed by placing this nonlinear negative resistance in parallel with a lossy LC resonator as shown in Figure 2.3 (a). In order to study such a circuit, it is customary to linearize it, by considering its frequency domain system model shown in Figure 2.3 (b).

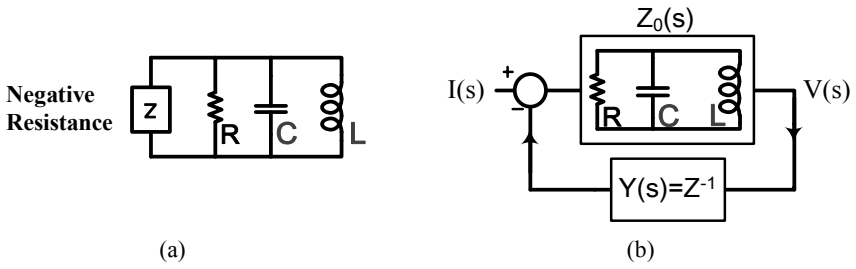

Figure 2.3: (*a*) *A basic RLC oscillator consisting of an RLC resonance tank and an energy compensating impedance* (*Z*)*, and* (*b*) *The system representation of this oscillator*

In order to obtain the linearized conductance Y in Figure 2.3 (b), a sinusoidal waveform (v_{IN}) is applied to the nonlinear conductance as shown in Figure **2.4**. The sinusoidal frequency is chosen

to be the resonance frequency of the LC resonator (ω_0). The Fourier series of the output square current waveform, for an input $v_{IN}(t) = V_0 \sin(\omega_0 t)$, is given by:

$$i(t) = -\frac{4I_0}{\pi} \sum_{n=1,3,5,\ldots} \frac{1}{n} \sin(n\omega_0 t) \tag{2.7}$$

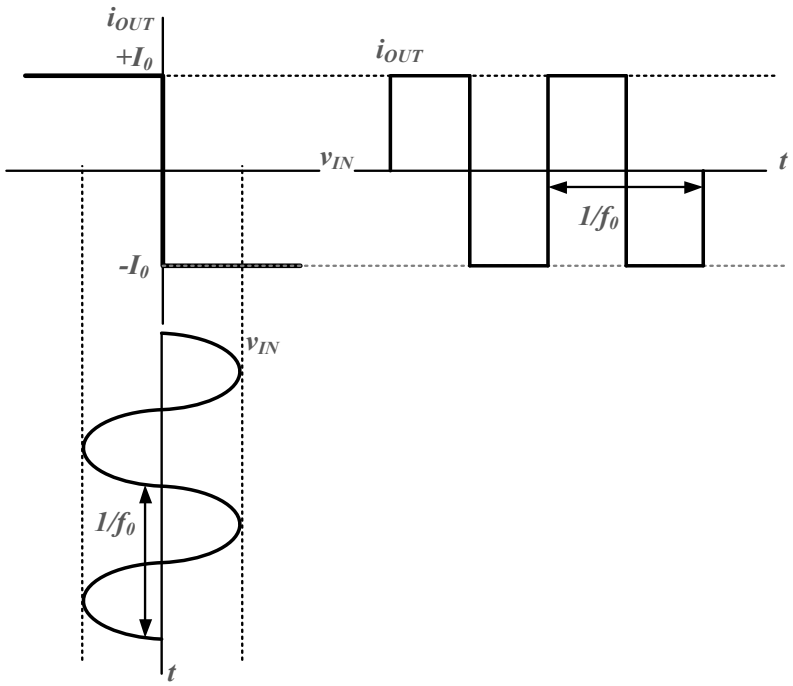

Figure 2.4: *Voltage input and current output waveforms of ideal nonlinear conductance*

Given the band-pass nature of the LC resonator, 3rd,5th and higher order harmonic terms in equation (2.3) should get attenuated and can be discarded. Therefore, the linearized conductance of the negative resistance at resonance is given by the following describing function:

$$Y(s) = \frac{4I_0}{\pi V_0} \tag{2.8}$$

Therefore, a linear transfer function ($H(s)$) can be used to describe the system in Figure 2.3 (b):

$$H(s) = \frac{V(s)}{I(s)} = \frac{Z_0(s)}{1 + Y(s)Z_0(s)} \tag{2.9}$$

Note that this is simply the impedance of the parallel R, L, C, Z elements. $Z_0(s)$ can be rewritten:

$$Z_0(s) = \frac{sR\omega_0 / Q}{s^2 + s\omega_0 / Q + \omega_0{}^2} \tag{2.10}$$

While the negative resistance described in Figure **2.2** and Figure 2.3, is theoretically easy to analyze, in reality it is impossible to obtain such a step transfer function. A real negative resistance can be realized using cross coupled active CMOS devices as in Figure **2.5**.

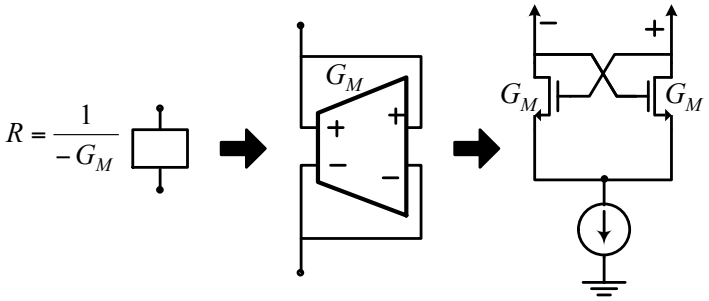

Figure 2.5: *Negative resistance realized using cross coupled transconductance*

Without going into details with regards to the conductance transfer function which depend on the CMOS device used, a few characteristics of such transfer function can be given, and are true regardless of the CMOS device used. A generic transfer function of the conductance is depicted in Figure **2.6**.

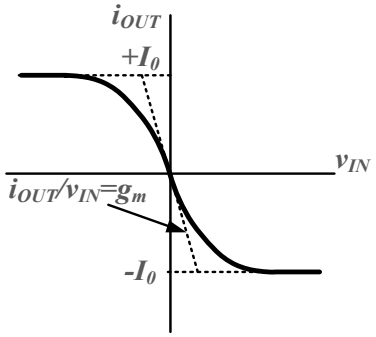

Figure 2.6: *Conductance transfer function of a generic non-ideal negative resistance*

For such a generic transfer function, the conductance depends on the amplitude of the swing (V_0). For a small V_0, the conductance of the negative resistor is simply given by the small-signal

transconductance of the CMOS devices $Y(s)=-g_m$. For a large V_0, the output waveform resembles a square wave, and the conductance's describing function $Y(s)=I_{\omega 0}/V_0$, where $I_{\omega 0}$ is the amplitude of the first harmonic of the periodic current waveform, which approaches $Y(s)=4/\pi(I_0/V_0)$ for an ideal square wave. These two values provide the minimum and maximum asymptotes for the conductance value versus the amplitude of the swing (v_0). The corresponding effective large signal transconductance is denoted G_M, where $Y(s)=-G_M$.

2.3. VCO Tuning

Tuning range is defined as the ratio of maximum to minimum oscillation frequencies of the VCO. The tank's quality factor is in general inversely proportional to the tuning range. Therefore, wider tuning range results in higher phase noises. A more detailed analysis of the tank's quality factor dependence on tuning range is given in Chapter 4.

Conventionally, some form of capacitive tuning is utilized to tune VCOs. Chapter 4 describes different capacitive tuning methods. This section, on the other hand, aims at introducing two methods that have been used to extend the tuning range of VCOs beyond that achievable by basic capacitive tuning. The two methods are: capacitive degeneration and multi-mode resonance.

2.3.1. Capacitance Degeneration

In order to overcome the limited frequency tuning imposed by parasitic capacitance, which becomes more dominant at higher frequencies, negative capacitance was introduced [15]. In addition, it has been shown that such technique provides finer frequency tuning and allows for using larger inductors which enhances the oscillator's performance[16]. The basic principle uses a source degeneration capacitance as shown in Figure **2.7**.

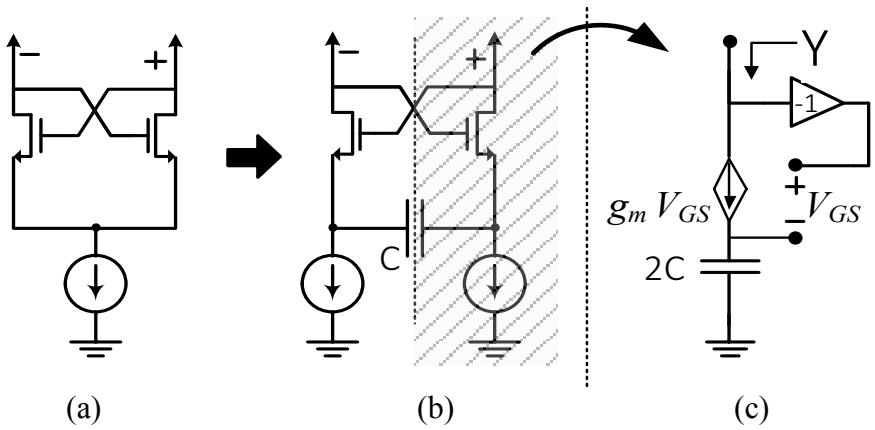

Figure 2.7: *Modification of* (*a*) *differential pair negative resistance to implement* (*b*) *a negative capacitance using source degeneration and* (*c*) *the corresponding half-circuit small signal model*

Using the small signal model shown in Figure **2.7** (c), one can derive the effective conductance (Y) seen at the single ended output of the differential pair as:

$$Y = -\left(\frac{4C^2\omega^2}{g_m{}^2 + 4\omega^2C^2}\right)g_M - \left(\frac{2g_m{}^2}{g_m{}^2 + 4\omega^2C^2}\right)j\omega C \tag{2.11}$$

Note that the differential conductance is $Y/2$. As long as the capacitance is large enough ($\omega C > g_m$), this will have no significant impact at reducing the negative resistance while providing additional negative capacitance to the tank. For a large capacitor value or at higher frequencies, the negative capacitance term becomes $-\left(\frac{2g_m{}^2}{4\omega^2C^2}\right)j\omega C$. This can be considered a negative capacitance with a scaling factor $2g_m{}^2/(4\omega^2C^2)$at a given frequency or a gyrator with effective inductance $C/g_m{}^2$.Under such operating conditions, this cannot be used for cancelling parasitic capacitance, thought it can provide fine tuning with effective inductance steps of $\Delta C/g_m{}^2$.

2.3.2. Multi-Mode Resonance

Multi-mode resonance uses coupled resonators as means to generate widely separated resonances compared to those of the original (uncoupled) resonators. This can be viewed as a complex pole

splitting action. Consequently, this creates widely separated tuning bands and reaches higher frequencies.

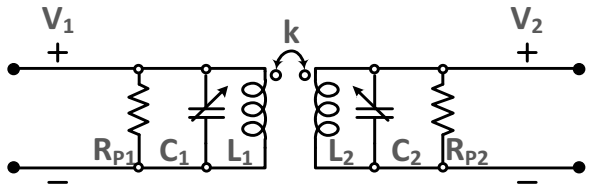

$$Z = \begin{pmatrix} Z_{11} & Z_{12} \\ Z_{21} & Z_{22} \end{pmatrix}$$

Figure 2.8: *An inductively coupled resonator*

For the inductively coupled resonator in Figure 2.8 we can express the Z-matrix as follows:

$$Z = \frac{1}{\Delta}\begin{pmatrix} \left(s^3 + \left(\frac{\omega_2}{Q_2}\right)s^2 + \left(\frac{{\omega_2}^2}{1-k^2}\right)s\right)L_1{\omega_1}^2 & \frac{k}{1-k^2}\sqrt{L_1L_2}\,{\omega_1}^2{\omega_2}^2 s \\ \frac{k}{1-k^2}\sqrt{L_1L_2}\,{\omega_1}^2{\omega_2}^2 s & \left(s^3 + \left(\frac{\omega_1}{Q_1}\right)s^2 + \left(\frac{{\omega_1}^2}{1-k^2}\right)s\right)L_2{\omega_2}^2 \end{pmatrix} \tag{2.12}$$

$$\Delta = s^4 + \left(\frac{\omega_1}{Q_1} + \frac{\omega_2}{Q_2}\right)s^3 + \left(\frac{\omega_1}{Q_1}\frac{\omega_2}{Q_2} + \frac{{\omega_1}^2 + {\omega_2}^2}{1-k^2}\right)s^2 + \frac{1}{1-k^2}\left(\frac{\omega_1{\omega_2}^2}{Q_1} + \frac{\omega_2{\omega_1}^2}{Q_2}\right)s + \frac{{\omega_1}^2{\omega_2}^2}{1-k^2}$$

Where ${\omega_{1,2}}^2 = 1/(L_{1,2}C_{1,2})$ are the resonator's uncoupled resonance frequencies and $Q_{1,2} = R_{P1,2}/(\omega_{1,2}L_{1,2})$ are their quality factors. Assuming an infinite quality factors the resonance frequencies of the coupled resonator are found to be:

$${\omega_{H,L}}^2 = \frac{\left({\omega_1}^2 + {\omega_2}^2\right) \pm \sqrt{\left({\omega_1}^2 + {\omega_2}^2\right)^2 - 4{\omega_1}^2{\omega_2}^2\left(1-k^2\right)}}{2\left(1-k^2\right)} \tag{2.13}$$

For symmetric tanks ($\omega_1 = \omega_2$), equation to:

$${\omega_{H,L}}^2 = \frac{1}{1 \pm k}{\omega_{1,2}}^2 \tag{2.14}$$

2.4. Start-Up Condition

The condition to obtain a sustainable oscillation for the system described in (2.9), can be reached using a number of system criteria:

2.4.1. Barkhausen's Criterion

Barkhausen's Criterion provides a necessary but not sufficient condition for oscillation:

$$\begin{aligned} &| Y(s)Z_0(s) | = 1 \\ &\angle Y(s)Z_0(s) = 2\pi n, n \in Z \end{aligned} \tag{2.15}$$

2.4.2. Root Locus Method

The root locus method traces roots of the characteristic equation in the complex plane:

$$1 + \mathrm{K}Y(s)Z_0(s) = 0, \mathrm{K} : 0 \to \infty \tag{2.16}$$

The condition necessary for oscillation is that the roots cross to the right half plane. Since right half plane roots of the characteristic equation represent right half plane poles of the closed loop system, the system is unstable.

2.4.3. Nyquist Stability Criterion

The number of unstable closed-loop poles (Z) of the system $H(s)$ is equal to the number of unstable open-loop poles (P) of $Y(s)Z_0(s)$ plus the number of clock-wise encirclements (N) of the complex point -1+0j of the Nyquist plot of $Y(s)Z_0(s)$. The Nyquist plot is the complex plot of $Y(s)Z_0(s)$ as "s" is swept along the complex contour in Figure 2.9 (a). The sweep from -∞j to ∞j along the imaginary axis is a simple frequency sweep of $s=j\omega$ as the frequency (ω) is swept from -∞ to ∞, while the angular sweep of $s= Ae^{j\varphi}$ ($A\to \infty$) from π/2 to -π/2 will map to a single point in the Nyquist plot as long as $Y(s)Z_0(s)$ is proper or strictly proper (Denominator is of equal or

higher order to Numerator of the transfer function).The stability criterion is summed up in the following simple equation:

$$Z = N + P \tag{2.17}$$

Nyquist criterion provides stability information in the form of phase margin (from the phase at which the Nyquist plot crosses the unity circle) and gain margin (from the magnitude of the Nyquist plot crossing the real axis) as shown in Figure 2.9 (b).

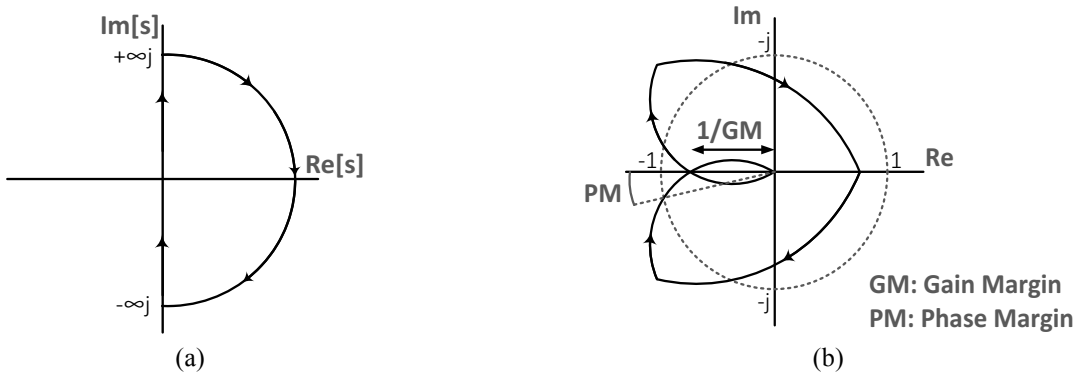

Figure 2.9: *(a) Contour of values of "s" swept to generate the Nyquist plot, and (b) an example Nyquist plot with gain and phase margins marked on the plot*

2.4.4. The Start-Up Condition of the Basic VCO

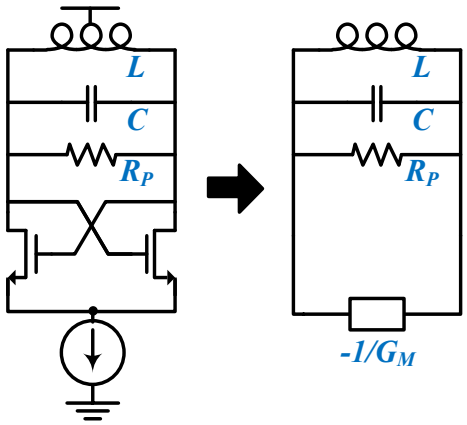

Figure 2.10: *Cross coupled oscillator schematic and equivalent small signal circuit*

In a cross coupled oscillator, the negative resistance appears in parallel with the LC tank due to the need to provide a DC bias current for the CMOS devices which can't be achieved if a series capacitance is inserted. As shown previously, this circuit would oscillate if the total resistance is less than or equal to zero.

A parallel resistance (R_P) is introduced to represent an equivalent theoretical lumped resistance that models the resistance in both the inductance and the capacitance. Under high quality factor assumption of both inductance and capacitance, the resistance R_P is related to the total series resistance in the RLC at resonance (ω_0) as $R_P \approx R_S Q^2$, where:

$$Q = \frac{\omega_0 L}{R_S} = \frac{1}{\omega_0 R_S C} = \frac{1}{R_S}\sqrt{\frac{L}{C}} \tag{2.18}$$

Similarly, the quality factor of the parallel RLC tank can be defined as:

$$Q = \frac{R_P}{\omega_0 L} = \omega_0 R_P C = R_P\sqrt{\frac{C}{L}} \tag{2.19}$$

The startup condition hence becomes:

$$R_P \,//\, \frac{-1}{G_M} = \frac{R_P}{1 - G_M R_P} \le 0 \quad \text{or} \quad G_M > \frac{1}{R_P} \tag{2.20}$$

For the basic VCO, we recall that the resonator has $Z_0(s) = \frac{sR\omega_0 / Q}{s^2 + s\omega_0 / Q + \omega_0{}^2}$ and that $Y(s)$=-G_M. In order to apply the root locus method, the describing equation is: $1 - G_M Z_0(s) = 0$. The root locus traces the poles of the describing equation as G_M is swept from 0 to ∞. This yields the following describing equation:

$$s^2 + s\frac{\omega_0}{Q}s(1 - G_M R) + \omega_0{}^2 = 0 \tag{2.21}$$

The poles corresponding to this equation are given by:

$$s = \left(\frac{G_M R - 1}{2Q} \pm j\sqrt{1 - \left(\frac{G_M R - 1}{2Q} \right)^2} \right) \omega_0 = \omega_0 e^{\pm j \cos^{-1}\left(\frac{G_M R - 1}{2Q} \right)} \tag{2.22}$$

These poles can plotted on the complex s-plane as shown in Figure 2.11. As apparent from the expression and the plot, the poles cross to the right half plane for any positive $\frac{G_M R-1}{2Q}$, or equivalently if G_M is greater than $1/R$.

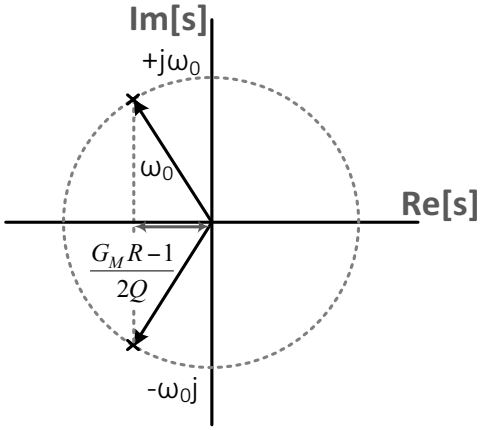

Figure 2.11: *Complex conjugate poles of the LC-tank VCO in the complex s-plane*

On the other hand, the Nyquist Criterion requires the creation of the Nyquist plot of the function $T(s) = -G_M Z_0(s)$. The Nyquist plot can be analytically constructed by considering the four points: $\{T(s=0),\ T(s=\infty j),\ Re[T(s=j\omega)]=0,\ Im[T(s=j\omega)]=0\}$. The points are summarized as follows:

$$\begin{aligned}
&& T(s=0) &= 0 \\
&& T(s=\infty j) &= 0 \\
\mathrm{Re}\left[T(s=j\omega)\right] = \frac{-\left(\frac{\omega}{\omega_0}\right)^2}{Q^2\left(1-\left(\frac{\omega}{\omega_0}\right)^2\right)^2+\left(\frac{\omega}{\omega_0}\right)^2} G_M R = 0 \quad &\rightarrow \quad T(s=0) &= 0 \\
\mathrm{Im}\left[T(s=j\omega)\right] = \frac{-Q\left(\frac{\omega}{\omega_0}\right)\left(1-\left(\frac{\omega}{\omega_0}\right)^2\right)}{Q^2\left(1-\left(\frac{\omega}{\omega_0}\right)^2\right)^2+\left(\frac{\omega}{\omega_0}\right)^2} G_M R = 0 \quad &\rightarrow \quad T(s=0) &= 0 \\
&& T(s=\omega_0) &= -RG_M \\
&& T(s=-\omega_0) &= -RG_M
\end{aligned} \tag{2.23}$$

$$\frac{d}{d\omega}\mathrm{Im}[T(s=\omega_0)] = \frac{d}{d\omega}\mathrm{Im}[T(s=-\omega_0)] = \frac{2G_M QR}{\omega_0} \tag{2.24}$$

The resulting plot is shown in Figure 2.12. The Nyquist plot as given by (2.23) and (2.24), starts from the point 0+0j and crosses $-G_M R$+0j twice with a positive imaginary gradient (clockwise) in both cases. Since $T(s)$ has no unstable poles by qualitative reasoning (the passives are lossy for any Q<∞), then for Z=N+P to be greater than 0, N has to be greater than 0. This condition can only occur if $-G_M R$<-1 or equivalently, G_M> 1/R. If P=2 for Q=∞, then the circuit is unconditionally unstable and it can oscillate for any G_M as expected.

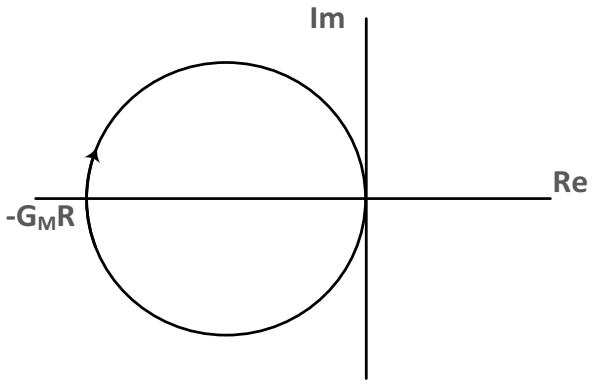

Figure 2.12: *Nyquist plot*

2.4.5. VCO Start-Up Summary

The transfer function $H(s)$ can be simplified with the assumption that $Y(s)$ is a real value ($-G_M$) and the impedance $Z_0(s)$ is the ratio of two polynomials of s: $Z_0(s) = \frac{N(s)}{D(s)}$

$$H(s) = \frac{Z_0(s)}{1 - G_M Z_0(s)} = \frac{N(s)}{D(s) - G_M N(s)} \tag{2.25}$$

Based on this and the previous discussion of startup conditions we can come up with the following set of equations that would satisfy start-up based on the Nyquist and the Root Locus criteria. Note that these conditions are compatible. Both equations can be further broken into real

and imaginary parts to provide two sets of equations whose solution yields the resonance frequency and the startup condition.

Root Locus	$D(j\omega) - G_M N(j\omega)$	$\mathrm{Re}[D(j\omega)] = G_M \mathrm{Re}[N(j\omega)]$ $\mathrm{Im}[D(j\omega)] = G_M \mathrm{Im}[N(j\omega)]$	
Nyquist Criterion	$-G_M Z_0(j\omega) = -1 + 0j$	$\mathrm{Im}[Z_0(j\omega)] = 0$ $\mathrm{Re}[Z_0(j\omega)] = \frac{1}{G_M}$	(2.26)

The two conditions share the assumption that the complex variable *s* is only swept along the imaginary axis ($j\infty$). As shown in Figure 2.13 (a), in the root locus plot, we are only interested in the poles when they are crossing from the left half plane to the right half plane so we only sweep along the imaginary axis. We then solve describing equation as given in (2.26). The equation can be further broken into imaginary and real parts to generate two equations. In the Nyquist plot displayed in Figure 2.13 (b), we are making an assumption that $-G_M Z_0(j\omega)$ has no right half plane poles, which is a reasonable assumption for any lossy resonator. Given that assumption, if the Nyquist plot of $-G_M Z_0(j\omega)$ crosses the point -1+0j (in a CW fashion), then the system is unstable. Similar to the root locus case, this equation can be further broken into imaginary and real parts.

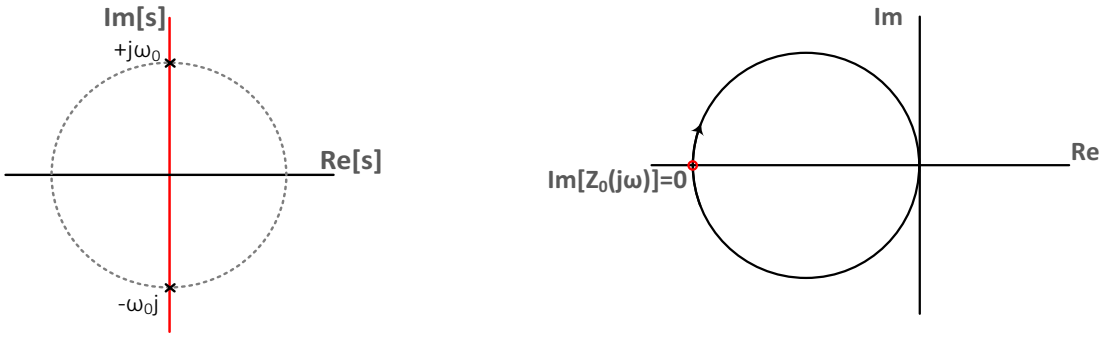

Figure 2.13: *(a) the s-plane is swept along the imaginary axis for both root locus and Nyquist plot methods as given by equation (***2.26***), and (b) The Nyquist plot that corresponds to start-up condition in equation (***2.26***) with the implicit assumption that $-G_M Z_0(j\omega)$ has no right half plane poles*

2.5. Phase Noise

2.5.1. The importance of phase noise: Spectral skirting and reciprocal mixing

An ideal sinusoidal oscillator's voltage waveform is given by $V(t) = A\cos(\omega_0 t + \phi_0)$, where A is a constant amplitude, ω_0 is the oscillation frequency and ϕ_0 is the initial phase. Such an ideal oscillator can be represented in the frequency domain by a single impulse as shown by the "Desired" signal highlighted in Figure 2.14.

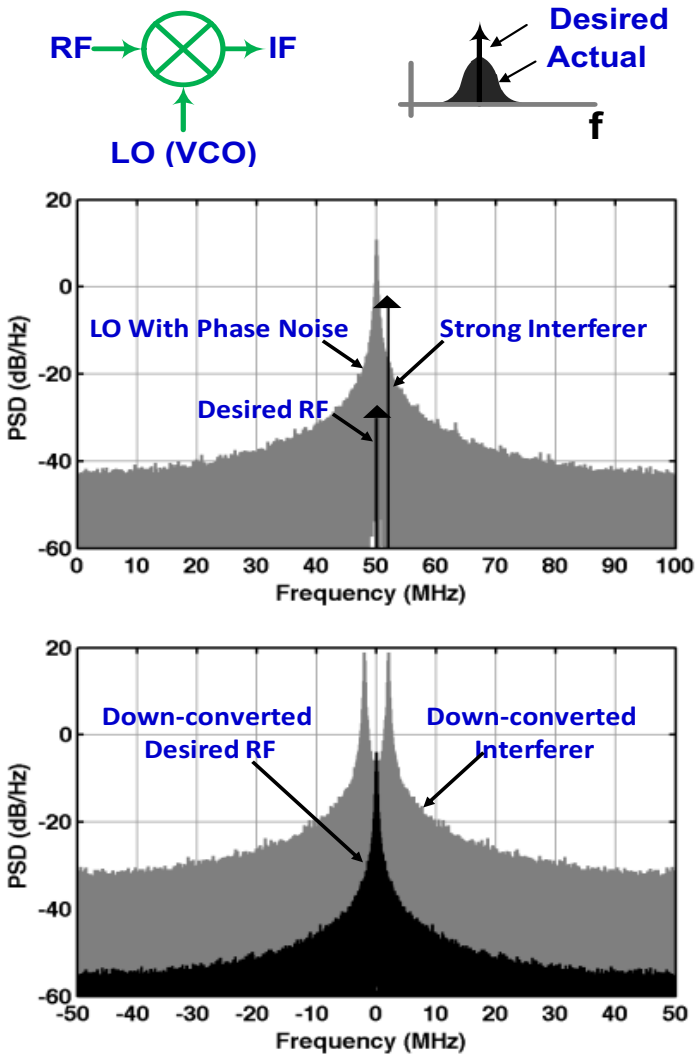

Figure 2.14: *Spectral skirting resulting from phase noise corrupting the down conversion of a desired received signal by an undesired blocker*

However, in a real voltage oscillator, the oscillation waveform is more generally given by $V(t) = A(t) f(\omega_0 t + \phi(t))$, where *f(x)* is a periodic function, and the amplitudes $A(t)$ and the added phase $\phi(t)$ fluctuate with time. These fluctuations are a result of different circuit noise sources presenting themselves at the oscillation node. Phase fluctuations known as *phase noise* can be represented in the frequency domain by sidebands appearing close to the desired oscillation frequency as captured by the "Actual" signal highlighted in Figure 2.14. This is known as spectral skirts. Therefore phase noise disperses the signal power over a wide frequency range rather than a single frequency tone.

In radio receivers, small desired signals are accompanied by large, unwanted interferers. Spectral skirts resulting from phase noise in the LO signal causes reciprocal mixing of the interferers down to the same frequency as the desired signal, thus corrupting the received desired signal as highlighted in Figure 2.14.

Phase noise $L(\Delta f)$ is defined as the power spectral density (PSD) of the phase fluctuation term ($\varphi_n(t)$) in (2.27). Phase noise can also be approximated by the single side band PSD of the voltage waveform, by taking the ratio of the PSD (measured at a given frequency offset from the center oscillation frequency) to the total carrier power as in equation (2.28).

The later definition of phase noise is only true for phase noise greater than amplitude noise, so that phase noise dominates the voltage spectrum, yet small enough so that the small angle approximations are valid. This can be seen in Figure 2.15, where both spectra are plotted for comparison.

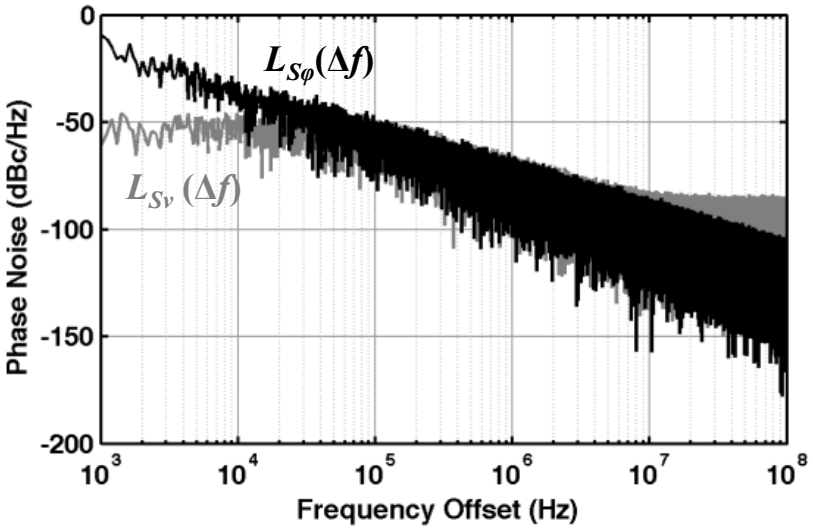

Figure 2.15: *Signal Spectrum and Phase spectrum vs. offset frequency as ways to determine phase noise*

$$V_{VCO}(t) = (V_0 + V_n(t))f(\omega_0 t + \varphi_n(t) + \varphi_0) \quad \text{where } f \text{ is periodic}$$
$$V_{VCO}(t) = (V_0 + V_n(t))\cos(\omega_0 t + \varphi_n(t) + \varphi_0) \quad \text{For a sinusoidal oscillation} \tag{2.27}$$

$$L(\Delta f) = \frac{S_{\varphi_n}(\Delta f)}{2} \approx \frac{S_{v,SSB}(\Delta f)}{\int S_v(\Delta f)df} \tag{2.28}$$

2.5.2. Leeson's LTI phase noise equation

In his partially empirical work, Leeson highlights that the phase noise spectrum of a feedback LTI oscillator is comprised of three major regions as depicted in Figure 2.16 [17].

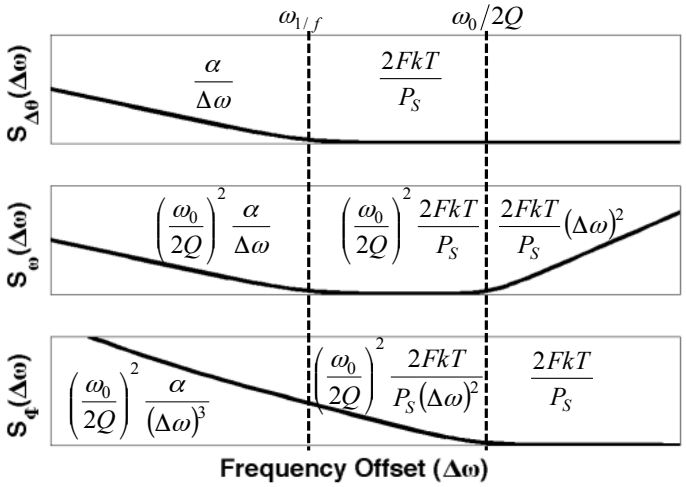

Figure 2.16: *Phase noise plot as described by Leeson [17]*

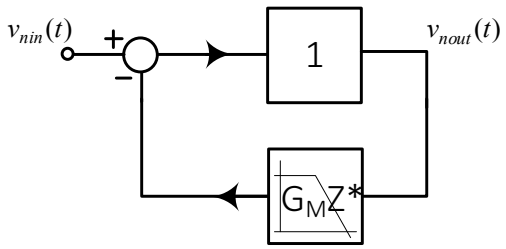

Figure 2.17: *LC oscillator equivalent baseband LTI system diagram*

In arriving at this conclusion, Leeson assumes that the oscillator is an LTI system whose equivalent baseband operation can be captured by the filter depicted in Figure **2.17**. The equivalent cutoff frequency ω_{3dB} is determined from the definition of the quality factor Q of a passive resonator, $Q = \dfrac{\omega_0}{2\omega_{3dB}}$, where ω_0 is the resonance frequency.

The input noise $v_{nin}(t)$ is noise resulting from circuit devices and it has a period to period phase noise given by $\Delta\theta$ and it has a spectrum equivalent to that of the voltage noise divided by the mean power (assuming small angle approximations). This spectrum is depicted in Figure 2.16 ($S_{\Delta\theta}(\Delta\omega)$) and it accounts for thermal white noise as well as flicker $1/f$ noise. The output period to period phase noise is the given by the input spectrum shaped by the equivalent transfer function:

$$H(\Delta\omega) = \frac{1}{1 + \dfrac{G_M Z_0^{\,*}}{1 + j\Delta\omega/\omega_{3dB}}} \approx \frac{1}{1 + \dfrac{1}{1 + j\Delta\omega/\omega_{3dB}}} \tag{2.29}$$

Where $G_M Z_0^*$ can be estimated by 1 at steady state operation of the oscillator where amplitude is kept constant. The frequency noise at the output can be related to the period to period noise at the

output, by the phase definition of quality factor $Q = \frac{\omega_0}{2}\left|\frac{\Delta\theta}{\Delta\omega}\right|$. Consequently, the added frequency noise ($S_\omega(\Delta\omega)$) is given by:

$$S_\omega(\Delta\omega) = \left(\frac{\omega_0}{2Q}\right)^2 |H(\Delta\omega)|^2 S_{\Delta\theta}(\Delta\omega) \tag{2.30}$$

Finally accumulated phase can be derived from frequency by taking the time integral, and the phase spectrum $S_\Phi(\Delta\omega)=S_\omega(\Delta\omega)/(\Delta\omega)^2$. This results in the following expression for the phase noise of a feedback tuned tank LTI oscillator:

$$L(\Delta\omega) = 10Log\left(\frac{2kT}{P_S}F\left(1+\left(\frac{\omega_0}{2Q\Delta\omega}\right)^2\right)\left(1+\frac{\Delta\omega_{1/f}{}^3}{\Delta\omega}\right)\right) \tag{2.31}$$

Where k is Boltzmann's constant, T is absolute temperature, P_S is the signal power at the oscillator's active element inputs, ω_0 is the resonance frequency, $\Delta\omega$ is the offset frequency, Q is the loaded quality factor of the passives. While the equation in its full form was not stated by Leeson, the plots he provide, which are replicated in Figure 2.16, indicate $\Delta\omega_{1/f}$ is the $1/f$ frequency cutoff of the input noise sources and F is an empirical parameter known as the device excess noise number. However, it has been clarified in the literature that both $\Delta\omega_{1/f}$ and F are empirically fit parameters that cannot be derived in the manner explained in the previous analysis[18].

2.5.3. Hajimiri's linear time-variant phase noise model

In his model, Hajimiri argues the LTI assumption, is incorrect and leads to being unable to correctly predict the performance of the system without obtaining the empirical parameters $\Delta\omega_{1/f}$ and *F apriori* [18]. In developing an alternative model, the oscillator is modeled as a linear time-variant (LTV) system. If an impulse current is injected at any node in the circuit, it will create a

voltage step proportional to the injected current. Such a voltage step can result in step in the amplitude or phase (or both) of the oscillation waveform. The oscillation's phase response to this current impulse ($h_\Phi(t,\tau)$) is periodic time-variant and is given by:

$$h_\Phi(t,\tau) = \frac{\Gamma(\omega_0\tau)}{q_{\max}} u(t-\tau) \tag{2.32}$$

where $\Gamma(\omega_0\tau)$ is known as the impulse sensitivity function (ISF) which is a periodic function that captures the magnitude of the oscillator's phase step in response to an injected current impulse at time τ, $q_{\max}=CV_{\max}$ is the maximum charge swing across the tank's capacitor and $u(t)$. Being a periodic function, the ISF can be written in terms of its Fourier series coefficients as:

$$\Gamma(\omega_0\tau) = \frac{C_0}{2} + \sum_{n=1}^{\infty} C_n \cos(n\omega_0\tau + \varphi_n) \tag{2.33}$$

Using the LTV model, an arbitrary oscillator's $1/f^2$ phase noise $L_{1/f^2}(\Delta\omega)$ evaluated at offset frequency $\Delta\omega$ from its resonant frequency ω_0 is expressed as:

$$L_{1/f^2}(\Delta\omega) = 10Log\left(\frac{\sum_m \Gamma_{rms,m}^2 \overline{i_{n,m}^2}/\Delta f}{2q_{\max}^2 \times (\Delta\omega)^2}\right) \tag{2.34}$$

where $\overline{i_{n,m}^2}/\Delta f$ is the power spectral density of the mth noise source, $\Gamma_{rms,m}^2$ is the root mean-square of the ISF. And the oscillator's $1/f^3$ phase noise $L_{1/f^3}(\Delta\omega)$ is given by:

$$L_{1/f^3}(\Delta\omega) = 10Log\left(\frac{\sum_m c_{0,m}^2 \left(\overline{i_{n,m}^2}/\Delta f\right)\left(\omega_{1/f,m}\right)}{4q_{\max}^2 \times (\Delta\omega)^3}\right) \tag{2.35}$$

Where $\omega_{1/f,m}$ is the $1/f$ noise corner of the mth noise source similar to before. This gives a closed form expression of the relationship between the $1/f$ noise corner of the source and the $1/f^3$ phase noise corner.

The impulse sensitivity function of a differential oscillator, oscillating with a sinusoidal waveform, to the noise of resonance tank's resistances, can be well approximated by a sinusoid in quadrature with its oscillation waveform and with magnitude equal to the inverse of the number of resonators in the oscillator (*N*) [19].

The overall noise term ($\sum \Gamma_{rms,m}^2 \overline{i_{n,m}^2} / \Delta f$) due to cyclostationary and non-cyclostationary thermal noise sources can be expressed as $\alpha k_B T / R$ where α is a constant the depends only on the architecture and operating region of the transistors, k_B is Boltzmann's constant, T is absolute temperature and R is the tank's equivalent parallel resistance.

For LC oscillators, the value of α was derived in [1] to be simply (1+γ), where γ is the noise factor of the oscillation transistors, where the transistor's noise power is modeled as $\overline{i_{n,ds}^2} = 4k_B T \gamma g_m \Delta f$.

For a current-limited oscillator, equation (2.34) can be expressed as:

$$L(\Delta\omega) = 10Log\left(\alpha k_B T \frac{1}{Q_{TANK}^3[\omega_0]} \times \frac{1}{L} \times \frac{1}{(2I_B)^2} \times \frac{\omega_0}{(\Delta\omega)^2} \right) \qquad (2.36)$$

where I_B is the tank's bias current, L is the tank's inductance and $Q_{TANK}[\omega_0]$ is the tank's quality factor at resonance. Equation (2.36) defines the theoretical relationship between the four performance metrics: resonant frequency, tuning range, phase noise, power consumption.

The bias current (I_B) in equation (2.36) is directly proportional to the DC power consumption of the oscillator $P = I_B V_{DD}$, where V_{DD} is the oscillator's supply voltage. Phase noise is inversely proportional to the power consumption as long as the oscillator is operating in the current-limited regime. When the oscillator enters the voltage-limited regime, its voltage swing becomes independent of the bias current I_B and equation (2.36) becomes invalid. For best phase noise

performance, oscillators are typically designed to operate at the edge of the voltage-limited regime where equation (2.36) is still valid [20].

Phase noise is directly proportional to resonant frequency if the oscillator's tank inductance and quality factor are maintained constant. However, the assumption that the term $Q_{TANK}^{3}[\omega_0]L$ is constant is not correct. This can be seen in the plot of maximum $Q_L^3\ (\omega_0)L$ for a number of inductor configurations in the 65 nm CMOS presented in Figure **4.1**.

2.5.4. The simulation of the impulse sensitivity function

The evaluation of the ISF function can yield significant insight into the output phase noise of an oscillator. The typical method to compute the ISF uses its original definition; by injecting a transient impulse current at a specific node and observing the corresponding steady-state phase shift. This method requires long simulations. An alternative method proposed by Pepe [21] uses frequency domain simulation to compute the ISF. This is accomplished by observing the output voltage waveform of the oscillator with a tonal noise input at the noise node. The paper [21] shows that the output fundamental oscillation waveform for an input noise tone at ω_m frequency offset from the at all n-harmonics $i_n(t) = \sum_n I_n \cos\left((n\omega_0 - \omega_m)t\right)$ is given by:

$$V_{VCO}(t) = V_0\left(\cos(\omega_0 t + \varphi_0) + \sum_n \frac{C_n I_n}{4q_{\max}\omega_m}\begin{pmatrix}+\cos\left((\omega_0 - \omega_m)t + \pi + \varphi_0 - \varphi_n\right)\\ +\cos\left((\omega_0 + \omega_m)t + \varphi_0 + \varphi_n\right)\end{pmatrix}\right) \qquad (2.37)$$

where C_n, φ_n are the ISF parameters in (2.33) and the other parameters correspond to the standard sinusoidal oscillation waveform as defined in (2.27). In Cadence SpectreRF simulator, this corresponds to a periodic steady state simulation (PSS) followed by a periodic transfer function (PXF) simulation. From the PSS simulation, the steady state amplitude and initial phase (V_0 and φ_0 respectively) are found. From the PXF simulation, the amplitudes at frequency offset

$\omega_0 \pm \omega_m$ and phases $\varphi_0 \pm \varphi_n$ are found, which allows the computation of parameters C_n, φ_n for the considered n^{th}-harmonics.

The extracted parameters are used in (2.33) to compute the ISF as approximated up to the nth considered harmonic. Since q_{max} is equal to V_0C, where C is the total loaded capacitance of the tank, the amplitude of the output modulated tones are independent of the amplitude V_0 but require the knowledge of the total capacitance. The loaded capacitance (including that from transistors) can be found from the oscillation frequency as $1/\omega_0^2 L$. The PSS-PXF simulation method is both more time efficient and more robust than the original transient simulation.

2.5.5. Impulse sensitivity function of a basic LC oscillator

The method for evaluating phase noise using PSS and PXF simulations has been discussed previously. Firstly, this method is applied to the basic LC-oscillator shown in Figure **2.18**.

The circuit consists of two CMOS transistor biased with an ideal 2mA tail current source and loaded with an ideal RLC load. The RLC load is selected to have a Q of 15 at a resonance frequency of 10GHz. Due to the CMOS devices' parasitic capacitance, the resonance frequency drops to 9.83GHz and the quality factor at resonance becomes 15.28.

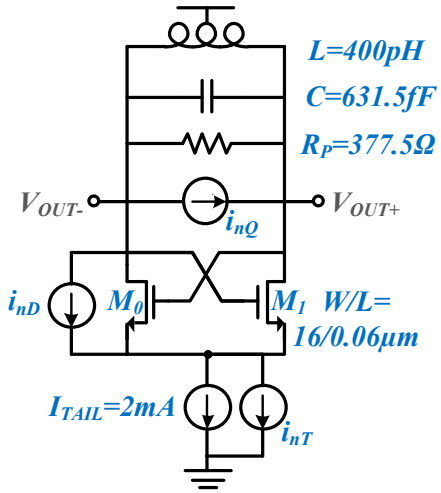

Figure 2.18: *Cross coupled LC-oscillator schematic with noise sources of interest highlighted (i_{nQ}, i_{nD}, i_{nT})*

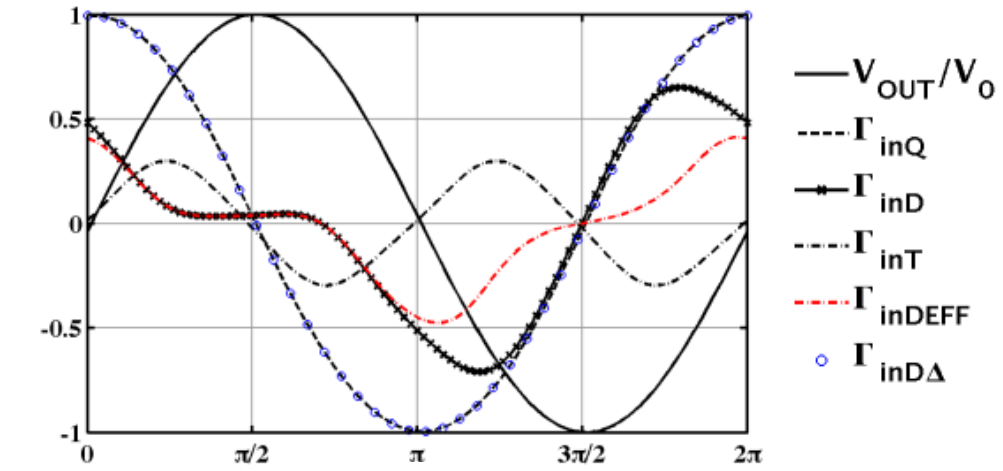

(a)

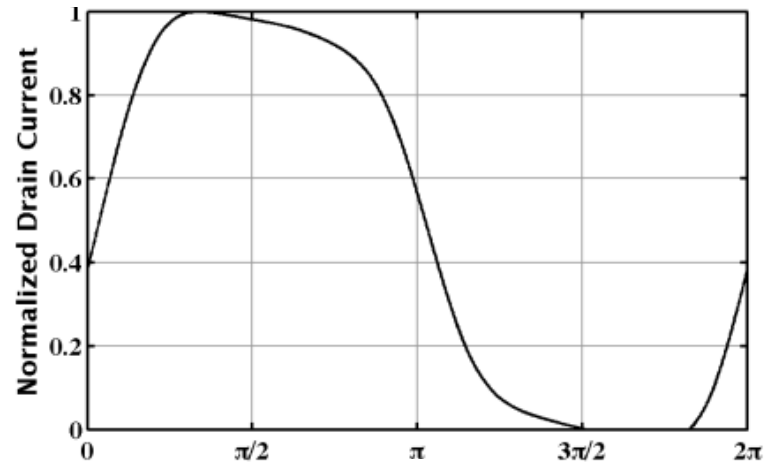

(b)

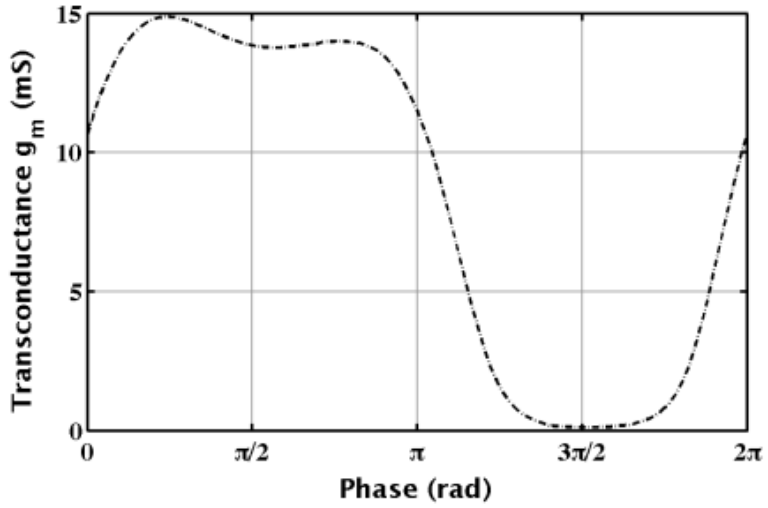

(c)

Figure 2.19: *(a) The normalized output voltage waveform and the Impulse sensitivity function of the output phase to noise injected at the three noise sources (i_{nQ}, i_{nD}, i_{nT}) as indicated in Figure* 2.18 *and (b) The normalized drain current and (c) transconductance of transistor M_0*

The three noises sources of interest are (1) the tank noise (i_{nQ}) generated by the loaded LC tank parasitic impedance (R_P), (2) the cross-coupled transistor noise (i_{nD}) and (3) the tail transistor noise (i_{nT}). The ISF plots are shown in Figure 2.19. The voltage and current results are normalized to 1 by dividing each waveform by the amplitude, while the ISF are presented as is. The time is normalized in the form of phase. The evaluated ISF functions are:

(1) *The tank noise ISF* (Γ_{inQ}) is approximately a sinusoid with amplitude equal to 1 and a phase offset of π/4 from the output voltage waveform. This result has been explored in the literature [19] and can be summarized for an oscillator, which consists of *n*-tanks, and whose sinusoidal output waveform is given by $v_{OUT}(t)=V_0\cos(\omega_0 t)$ as:

$$\Gamma = \frac{\cos(\omega_0 t + \frac{\pi}{2})}{n} \tag{2.38}$$

The tank noise ISF (Γ_{inQ}) is maximum during differential output voltage zero-crossing since all injected current noise contributes to phase noise rather than amplitude noise. The ISF is minimum when the voltage is maximum, as all current swings contribute to amplitude fluctuations rather than phase fluctuations. This can be best understood by observing the state-space of the voltage and current in the tank as the oscillation takes place as in Figure 2.20.

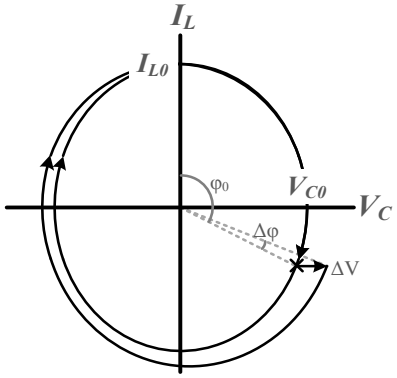

Figure 2.20: *The state-space of the single LC-tank oscillator as defined by the voltage across the capacitor (V_C) and the current inside the inductor (I_L): A charge injection results in a voltage step (ΔV), which can cause a phase shift ($\Delta\varphi$), while the oscillation amplitude eventually returns to V_{C0} limited by circuit nonlinearities [18]*

As shown in Figure 2.20, an impulse current results in a voltage step (ΔV). The voltage step can result in a phase shift ($\Delta\varphi$). If the voltage step occurs at phase $\varphi_0=k\pi+\pi/2$ then no phase step occurs and the impulse sensitivity is 0. If the occurs at phase $\varphi_0= k\pi$ then maximum phase step occurs and the impulse sensitivity is maximum.

(2) *The transistor noise ISF* (Γ_{inD}) follows Γ_{inQ} closely while the transistor is off as all the noise generated couples directly to the output and the sensitivity is only impacted by the output voltage and phase. On the other hand, as the transistor turns on and starts conducting, the sensitivity to the noise source drops as the noise current starts flowing into the transistor's low impedance rather than getting channeled to the output node.

(3) *The differential transistor noise ISF* ($\Gamma_{inD\Delta}$) given by the difference between the two ISFs from transistors M_0 and M_1. Is equal to the tank noise ISF (Γ_{inQ}). This ISF will be used for deriving closed form expression of the phase noise from the differential pair.

(4) *The effective transistor noise ISF* (Γ_{inDEFF}) captures the impact of the large signal swing on the noise generated by transistors M_0 and M_1 and effectively their overall noise contribution at the output. The thermal current noise power density of a CMOS transistor is approximately:

$$\overline{i_n^2}/\Delta f = 4kT\gamma g_m \tag{2.39}$$

The parameter γ is equal to 2/3 for long-channel transistors and can be larger than that for short channel transistors. Since g_m, which is depicted in Figure 2.19 (c) is deterministic and varies periodically during the oscillation cycle; the noise is cyclostationary and can be described as:

$$i_n(t) = i_{n0}(t)\sqrt{g_m(\omega_0 t)} \qquad \text{Where } \overline{i_{n0}^2}/\Delta f = 4kT\gamma \tag{2.40}$$

Hence, the cyclostationary thermal noise can be decomposed into a product of a stationary thermal noise i_{n0}^{2}'/Δf, and the deterministic periodic function $\sqrt{g_m(\omega_0 t)}$. The effective ISF of thermal noise i_{n0}^{2}'/Δf is therefore given by the product:

$$\Gamma_{inDEFF} = \sqrt{g_m(\omega_0 t)}\Gamma_{inD} \tag{2.41}$$

Similarly, an effective ISF can be defined for the differential transistor noise as:

$$\Gamma_{inD\Delta EFF} = \sqrt{G_M(\omega_0 t)}\Gamma_{inD\Delta} \tag{2.42}$$

The differential transistor noise can be derived as $\frac{di_{diff}}{dv_{diff}}$, where v_{diff} is the differential voltage at the input (gates) of the differential pair, and I_{diff} is the differential output current. Assuming that the transistors operate as switches, for a sinusoidal input differential voltage (v_{diff}), the effective differential current (i_{diff}) switches between $I_T/2$ and $-I_T/2$ where I_T is the tail current, and is in phase with the voltage. This assumes that transistors do not introduce a phase shift or equivalently, the transistors have a much larger bandwidth than the operating frequency.

One way to approximate such switching nonlinearity is using a hyperbolic tangent (*tanh*) function, where the periodic voltage and current can be expressed as:

$$\begin{aligned} v_{diff}(\phi) &= V_0 \cos(\phi) \\ i_{diff}(\phi) &= I_0 \tanh\left(g_{m0} v_{diff}(\phi)\right) = I_0 \tanh\left(g_{m0} \frac{V_0}{I_0} \cos(\phi)\right) \end{aligned} \tag{2.43}$$

where $I_0=I_T/2$, g_{m0} is the small signal transconductance and V_0 is the voltage amplitude. This is depicted in Figure 2.21, for a $K=g_{m0}V_0/I_0=1, 10$.

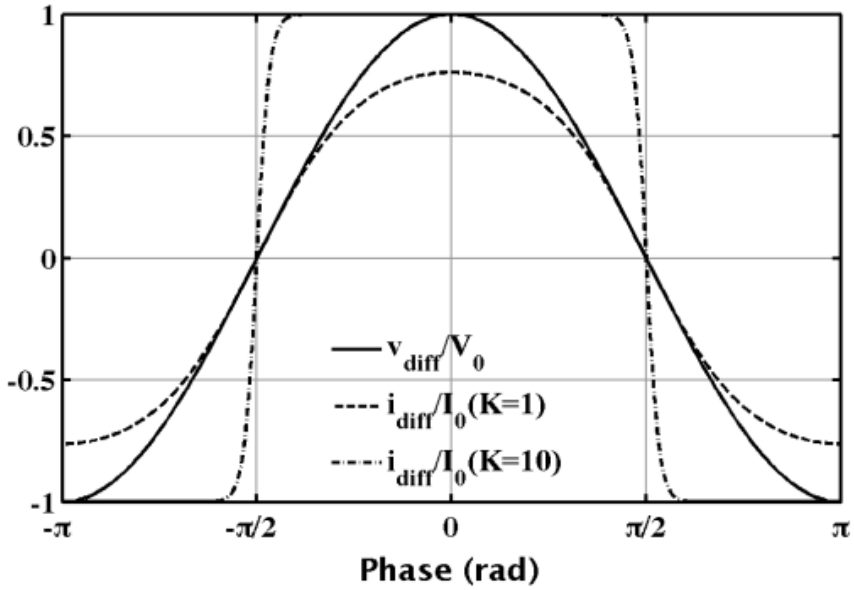

Figure 2.21: *Normalized periodic oscillating differential voltage* (v_{diff}) *and switching current* (i_{diff}) *waveforms captured by a hyperbolic tangent* (*tanh*) *function*

The resulting differential transconductance is:

$$G_M(\phi) = \frac{di_{diff}(\phi)}{dv_{diff}(\phi)} = g_{m0}\,\mathrm{sech}\left(g_{m0}\frac{V_0}{I_0}\cos(\phi)\right)^2 \tag{2.44}$$

As g_{m0} grows much larger than I_0/V_0, in the case of an ideal switch, the differential transconductance approaches:

$$G_M(\phi) = 2\frac{I_0}{V_0}\left(\delta\left(\phi+\tfrac{\pi}{2}\right)+\delta\left(\phi-\tfrac{\pi}{2}\right)\right) \tag{2.45}$$

This provides a very good estimate to be used in closed form expression evaluation of ISF, and it's independent of the exact type on the nonlinearity (exponential or *tanh*) since it assumes ideal switching. This is depicted in Figure 2.22 as $G_M(\Phi)$ for $K=g_{m0}V_0/I_0$=1, 2,5,10,100 showing how $G_M(\Phi)$ approaches a Dirac delta function. As $G_M(\Phi)$ approaches a Dirac delta, only the ISF value of the output node at π/2 and –π/2 becomes significant.

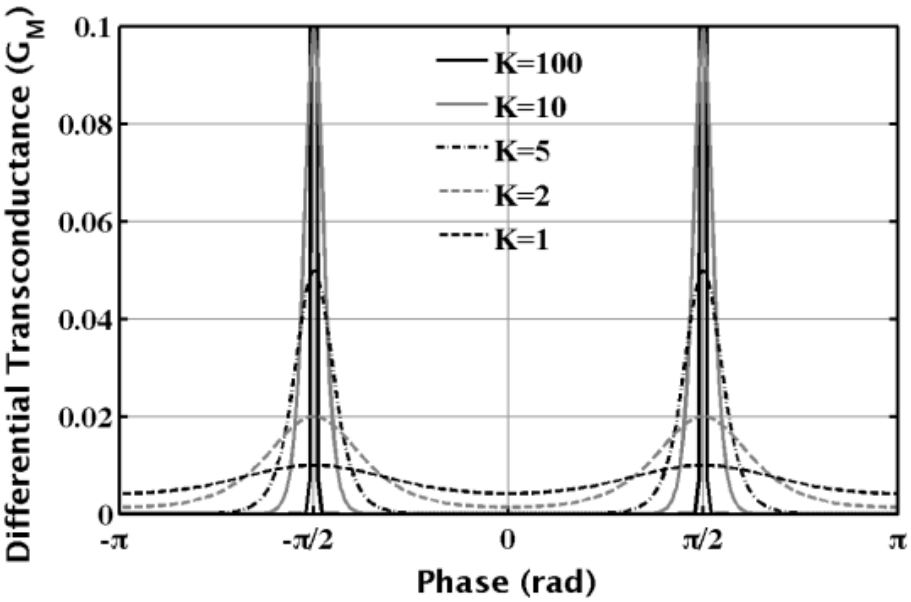

Figure 2.22: *Effective differential transconductance* (G_M) as a function of phase, showing how as the value of $K=g_{m0}V_0/I_0$ increases, the transconductance approaches a Dirac delta.

Given that $\Gamma_{inD\Delta} = \frac{1}{n}\sin(\omega_0 t)$, the effective ISF is:

$$\Gamma_{inD\Delta EFF} = \frac{1}{n}\sqrt{2\frac{I_0}{V_0}}\left(\sin\left(\phi+\tfrac{\pi}{2}\right)+\sin\left(\phi-\tfrac{\pi}{2}\right)\right) \tag{2.46}$$

$$\Gamma_{inD\Delta EFF,rms}{}^2 = \frac{1}{n}\frac{2}{\pi}\frac{I_0}{V_0} \tag{2.47}$$

which can be written in terms of the first harmonic of the switching current $I_{\omega 0}=4I_0/\pi$:

$$\Gamma_{inD\Delta EFF,rms}{}^2 = \frac{1}{2n}\frac{I_{\omega 0}}{V_0} = \frac{I_{\omega 0}}{V_0}\Gamma_{inD\Delta,rms}{}^2 = \frac{1}{R_p}\Gamma_{inD\Delta,rms}{}^2 \tag{2.48}$$

The same result is presented in [22], using a Fourier expansion of the transconductance. While both approaches yield the same estimate for a non-quadrature ISF, only this method is able to capture the impact of quadrature ISF on the overall effective ISF as will be discussed later.

(5) *The tail current noise ISF* is impacted by two mechanisms: The output waveform voltage and phase which defines its sensitivity to any injected current at that node (namely Γ_{inQ}) and the

current splitting between the two legs of the differential pair. The assumption is that the tail current is an ideal current source and hence there should be no consideration for noise current splitting between the current source itself and the output nodes. When both diff-pair transistors are equally conducting, the noise from the tail transistor will appear as a common mode noise component at the output rather than a differential noise component and hence the differential output would be least sensitive to the noise during these transitions and that should correspond to ISF nulls. Since the currents splits equally when the differential voltage at the output is 0, this corresponds to maximum $\Gamma_{inQ,}$ and vice versa. Hence the two aforementioned contributors to the impulse sensitivity of the tail transistor are in quadrature. Since the overall ISF is the result of the product of these two processes, the overall ISF is the product of two in quadrature processes, which translate to a waveform with twice the frequency of Γ_{inQ} and a lower amplitude. The sinusoidal nature of Γ_{inT} seen in Figure 2.19, indicate that both processes contribute equally to the overall ISF.

2.5.6. ISF-based phase noise derivation for the basic LC oscillator

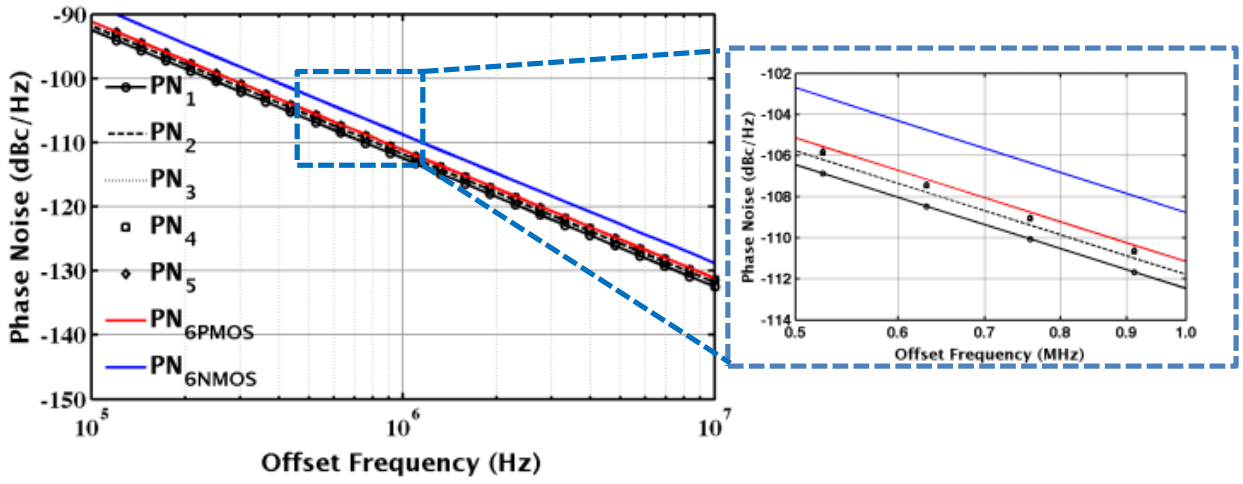

Figure 2.23: *Phase noise plots for circuit shown in Figure* **2.18**

The phase noise is obtained from the ISF functions according to equation (2.34) and plotted in Figure **2.23**. The plot contrasts a number of cases for which phase noise is computed/simulated. The cases are given by:

(1) PN_1: A closed form expression of the phase noise considering the thermal noise from the transistors M_0, M_1 and R_P as:

$$L_{1/f^2}(\Delta\omega) = 10Log\left(\frac{\Gamma_{inQ,rms}^2\left(\frac{4k_bT}{R_P}\right) + \Gamma_{inD\Delta,rms}^2\left(\frac{4k_bT\gamma}{R_P}\right)}{2(CV_0)^2 \times (\Delta\omega)^2}\right) \tag{2.49}$$

$$L_{1/f^2}(\Delta\omega) = 10Log\left(\frac{\frac{1}{2}\left(\frac{4k_bT}{R_P}\right) + \frac{1}{2}\left(\frac{4k_bT\gamma}{R_P}\right)}{2(Q)^2 {I_{\omega 0}}^2}\left(\frac{f_0}{\Delta f}\right)^2\right) \tag{2.50}$$

where Boltzmann's constant k_b=1.38·10^{-23} m^{2}kg s^{-2}K^{-1} , the temperature T=300K and the design parameters Q=15.275, R_P=377.5, f_0=9.833 GHz and γ=1. The first harmonic of the output switching current can be estimated as $2/\pi I_B$ where I_B is the bias current (2mA).

(2) PN_2: A closed form expression of the phase noise given by equation (2.49), with all parameters as before but using the output voltage amplitude (V_0) from simulation.

(3) PN_3: Phase noise expression from the ISF and voltage plots depicted in Figure 2.19.

(4) PN_4: Simulated PN using a Cadence SpectreRF PSS and PNOISE simulations using same circuit schematic and device models with only thermal noise.

(5) PN_5: Simulated PN using a Cadence SpectreRF PSS and PNOISE simulations using same circuit schematic and device models with thermal and 1/f noise.

(6) PN_{6PMOS} , PN_{6NMOS}: Simulated PN using a Cadence SpectreRF PSS and PNOISE simulations using same circuit schematic and device models with thermal and 1/f noise with a non-ideal (transistor based) tail current source using both PMOS and NMOS tail current bias current architectures as shown in Figure **2.24**.

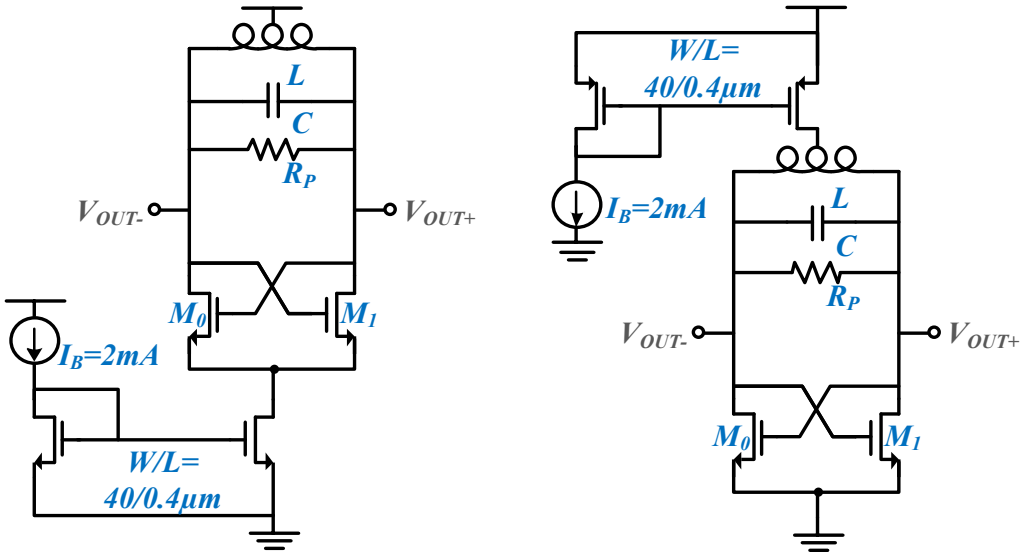

(a) (b)

Figure 2.24: *(a) NMOS and (b) PMOS based current biasing circuit*

Since the values of phase noise are very close for a number of the plots, their values are tabulated for 10 kHz and 1 MHz offset frequencies in Table 1.

Table 1: *Phase noise evaluated for the LC-tank at 10kHz, 1MHz for a number of cases*

	PN@10kHz dBc/Hz	**PN@1MHz** dBc/Hz
PN_1	-72.4338	-112.434
PN_2	-71.759	-111.759
PN_3	-71.1166	-111.117
PN_4	-71.4337	-111.433
PN_5	-69.7595	-111.389
PN_{6PMOS}	-70.6955	-111.13
PN_{6NMOS}	-65.8468	-108.741

Based on the results in Figure **2.23** and Table 1 the following can be concluded:

(1) The theoretically estimated phase noise is accurate within 1.5 dBc/Hz (PN_1 vs. PN_4).

(2) The estimate is improved by using the actual output voltage which drops the error by 0.7 dBc/Hz, indicating that the first harmonic amplitude of the tank current is not as large as $4/\pi I_B$ which is expected given the shape of the current waveform in Figure 2.19 (b).

(3) The evaluation of phase noise from the ISF and voltage plots matches almost exactly the simulated phase noise (PN_3 vs. PN_4) which validates the ISF simulations.

(4) The introduction of $1/f$ (PN_4 vs. PN_5) did not have significant impact at 1 MHz since the $1/f^3$ corner frequency is less than 1 MHz . The impact is more pronounced at 10 kHz.

(5) The increase of Phase noise due to PMOS biasing is significantly less than that due to the NMOS tail current (0.3dBc/Hz vs. 2.3dBc/Hz at 1MHz). It's expected for the PMOS biasing to introduce less noise since it has lower thermal and flicker noise and does not drive the differential devices into deep triode.

2.6. Quadrature Considerations

When extending the previous phase noise analysis to quadrature VCOs, additional consideration must be given to the quadrature implementation. Quadrature outputs are typically obtained by placing two identical VCOs inside a quadrature loop. The 90^o phase shift is obtained by introducing an excess 180^o phase shift inside the loop and ensuring that the only possible mode of oscillation in that case is if both signals outputs are in quadrature. Several quadrature implementation techniques have been studied in the literature. Many of these implementations can be modeled by extending the linearized LC-tank oscillator model in Figure **2.10** to the linearized quadrature LC-tank oscillator model in Figure **2.25**.

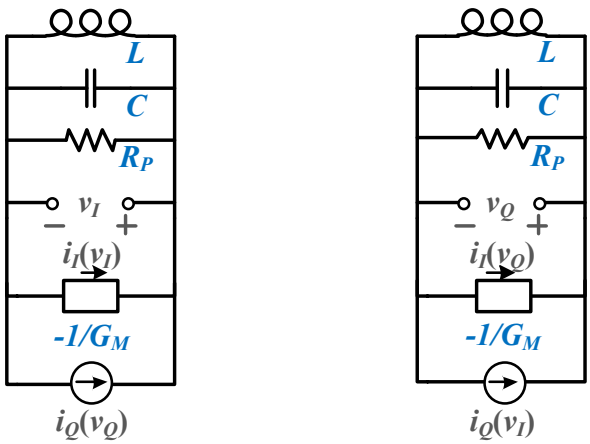

Figure 2.25: *Linearized quadrature LC-tank oscillator model*

In such model, the quadrature loop injects a current phasor (i_Q) that is at angle (typically perpendicular) to the VCOs internal positive feedback current phasor (i_I) in both coupled oscillators. This can be captured by considering the current phasors and their summation as depicted in Figure **2.26**.

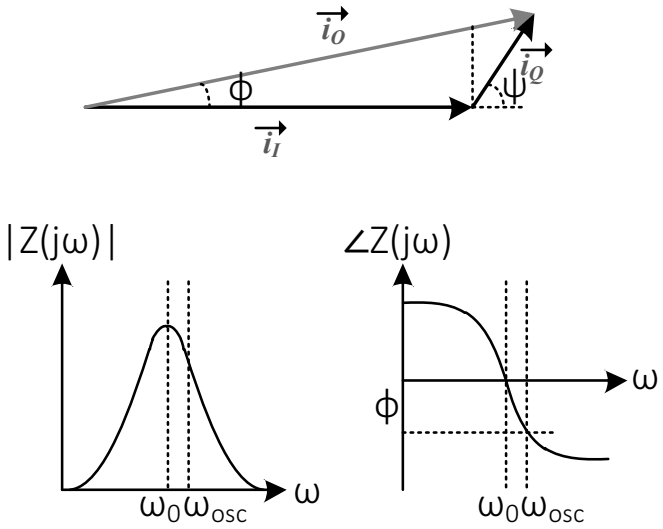

Figure 2.26: *Quadrature current phasors summing up at the oscillation nodes and causing a frequency shift from the natural oscillation frequency of the LC- tank*

As can be seen in Figure **2.26**, the addition of the two phasors (i_Q , i_I) can only happen if there is a phasor (i_O) that sums the two currents at the LC-tank. Since the voltage across the tank is in

phase with (i_I), then the phase between the voltage across the tank and the current through it is Φ. Therefore, adding up the two current phasors, results in a frequency shift equal to [23]:

$$\omega_{OSC} = \omega_0 \left(1 \pm \frac{1}{2Q} \frac{\frac{I_Q}{I_I} |\sin(\Psi)|}{1 + \frac{I_Q}{I_I} |\cos(\Psi)|} \right) \tag{2.51}$$

where I_Q and I_I are the magnitudes of the in-phase and quadrature vectors (i_Q , i_I) and they usually correspond to the tail bias current of the corresponding transistors. For the common case where the angle between the phasors (Ψ=90^o), the expression simplifies to:

$$\omega_{OSC} = \omega_0 \left(1 \pm \frac{1}{2Q} \frac{I_Q}{I_I} \right) \tag{2.52}$$

This frequency shift degrades phase noise by converting the current phasor's amplitude noise into phase noise. Furthermore, as frequency is shifted away from the tank's resonant frequency, the tank's effective quality factor at the oscillation frequency is reduced. In addition, additional noise is introduced from the devices used to implement the quadrature loop. The frequency shift can be reduced by reducing the injected quadrature current. However, this directly impacts the quadrature phase error, which is defined as the offset of the I/Q phase difference from 90^o.

In [4], three QVCO architectures are compared to identify the trade-off between phase noise and phase error. These architectures were presented in Figure **1.1**. The architectures were: 1) Parallel QVCO, where the quadrature devices appear in parallel to the in-phase devices. 2) Top-Series QVCO, where the quadrature devices appear in series with the in-phase devices and are placed between the output nodes and the in-phase devices. 3) Bottom-Series QVCO, where the quadrature device appears in series with the in-phase device but placed between the in-phase device and the tail current source. The study shows that using Top-Series/Bottom-Series QVCO can yield a phase noise increase of less than 1dBc/Hz at 2GHz when compared to a VCO that

doesn't implement quadrature. Additionally, the study shows that using the Parallel QVCO yields a much worse result, which is 3dBc/Hz higher than the phase noise obtained using the Top-Series/Bottom-Series QVCOs.

As an alternative, passive quadrature injection has been presented in [8],[11],[6]. One embodiment of this technique employs transformers to create the 90^o phase shift [11]. Coupled LC resonators are fourth-order systems capable of providing up to 360^o phase shift and can be designed to provide the highest quality factor defined as $\frac{\omega_0}{2}\left|\frac{d\phi}{d\omega}\right|$ in the vicinity of 90^o phase shift. Hence, if a loop is formed to contain two such identical transformers in addition to a 180^o phase shift it's possible to obtain quadrature without introducing additional phase noise. The phase error is dependent only on the matching between the two transformers in the quadrature loop.

There has been two works that attempted to fully quantify the impact of the quadrature on phase noise using: (1) Extended Adler's equation work by Mirzaei et al [23] and (2) ISF based approach by Andreani [24]. Both works reach same conclusions, however, Andreani's work is better fitted as an extension to the previous ISF based noise analysis introduced in the previous sections. The fundamental and most significant conclusion presented in [24] is that for the quadrature oscillator, and specific case where $\Psi=90^o$, the ISF given by equation (2.38), which corresponds to a sinusoidal output waveform ($v_{OUT}(t)=V_0\cos(\omega_0 t)$), is rewritten as:

$$\Gamma = \frac{\cos(\omega_0 t + \frac{\pi}{2} + \theta)}{n\cos(\theta)}$$
$$\theta = \arctan\left(\frac{I_Q}{I_I}\right) \tag{2.53}$$

The second significant conclusion of [24] is that the oscillation amplitude is independent of the coupling strength (I_Q/I_I). By combining the two previous works, one can postulate that the angle (θ) can be extended for a general case where $\Psi \neq 90^o$ as $\theta = \arctan(k)$, where:

$$k = \frac{\frac{I_Q}{I_I}|\sin(\Psi)|}{1 + \frac{I_Q}{I_I}|\cos(\Psi)|} \tag{2.54}$$

Given the ISFs, an ISF based closed form expression for phase noise can be derived by considering the thermal noise from three noise sources: (1) the tank noise (Γ_{inQ}), (2) the in-phase devices ($\Gamma_{inD\Delta EFF-I}$) and (3) the quadrature devices ($\Gamma_{inD\Delta EFF-Q}$):

(1) Γ_{inQ} is given by (2.53), and its root mean square value is $\Gamma^2_{inQ,rms} = \frac{1}{2n^2\cos^2(\theta)} = \frac{1+k^2}{2n^2}$. This indicates that the noise from the tank increases as $1/\cos^2(\theta)$ due to quadrature. It must be noted that there is still a noise improvement by the fact that quadrature couples two oscillators (n=2) at the expense of burning twice the power.

(2) $\Gamma_{inD\Delta EFF-I}$ is given by the product $\Gamma_{inQ}\sqrt{G_{MI}(\phi)}$

$$\Gamma_{inD\Delta EFF-I}(\phi) = \frac{\cos(\phi + \frac{\pi}{2} + \theta)}{n\cos(\theta)} \sqrt{2\frac{I_I}{V_I}\left(\delta\left(\phi + \tfrac{\pi}{2}\right) + \delta\left(\phi - \tfrac{\pi}{2}\right)\right)} \tag{2.55}$$

The corresponding root mean square $\Gamma^2_{inD\Delta I,rms}$

$$\Gamma^2_{inD\Delta EFF-I,rms} = \frac{1}{n^2}\frac{2}{\pi}\frac{I_I}{V_I} = \frac{1}{2n^2}\frac{I_{I\omega 0}}{V_I} = \frac{1}{R_p}\Gamma^2_{inQ,rms} \tag{2.56}$$

This simplification is only correct due to the swing being independent of θ. This indicates that the noise contribution from the in-phase devices is the same as that in the case without quadrature as given by equations (2.47) and (2.48), ignoring the noise improvement due to coupling two oscillators. Furthermore, this noise is independent of the strength of the coupling.

(3) $\Gamma_{inD\Delta EFF-Q}$ is given by the product $\Gamma_{inQ}\sqrt{G_{MQ}(\phi)}$, where the differential large signal transconductance of the quadrature devices (G_{MQ}) is derived similar to G_{MI}:

$$G_{MQ}(\phi) = 2\frac{I_Q}{V_Q}\left(\delta(\phi) + \delta(\phi - \pi)\right) \tag{2.57}$$

where I_Q in this case is the bias current of the coupling devices, equal to half the tail current of the coupling devices and V_Q is the voltage amplitude on the quadrature node which is typically equal to amplitude on the in-phase node (V_I). The ISF is therefore given by:

$$\Gamma_{inD\Delta EFF-Q}(\phi) = \frac{\cos(\phi + \frac{\pi}{2} + \theta)}{n\cos(\theta)}\sqrt{2\frac{I_I}{V_I}\frac{I_Q}{I_I}\left(\delta(\phi) + \delta(\phi - \pi)\right)} \tag{2.58}$$

The corresponding root mean square $\Gamma^2_{inD\Delta Q,rms}$

$$\Gamma^2_{inD\Delta EFF-Q,rms} = \frac{1}{n^2}\frac{2}{\pi}\frac{I_I}{V_I}\frac{I_Q}{I_I}k^2 = \frac{1}{2n^2}\frac{I_{I\omega 0}}{V_I}\frac{I_Q}{I_I}k^2 = \frac{1}{R_p}\frac{I_Q}{I_I}k^2\Gamma^2_{inQ,rms} \tag{2.59}$$

The overall phase noise closed form expression, derived from the previous ISFs is:

$$L_{1/f^2}(\Delta\omega) = 10Log\left(\frac{2\left(\Gamma^2_{inQ,rms}\left(\frac{4k_bT}{R_P}\right) + \Gamma^2_{inD\Delta I,rms}(4k_bT\gamma) + \Gamma^2_{inD\Delta Q,rms}(4k_bT\gamma)\right)}{2(CV_0)^2 \times (\Delta\omega)^2}\right)$$

$$L_{1/f^2}(\Delta\omega) = 10Log\left(\frac{\left(1 + k^2 + \gamma\left(1 + \frac{I_Q}{I_I}k^2\right)\right)\left(\frac{4k_bT}{R_P}\right)}{8(Q)^2 {I_{\omega 0}}^2}\left(\frac{f_0}{\Delta f}\right)^2\right) \tag{2.60}$$

In order to verify this conclusion, a test circuit is created and simulated, similar to the analysis performed on the LC-tank oscillator in Chapter 2.5.6 for the quadrature oscillator shown in Figure **2.27**. For this circuit $\Psi=90^o$ and $k=I_Q/I_I=1$.

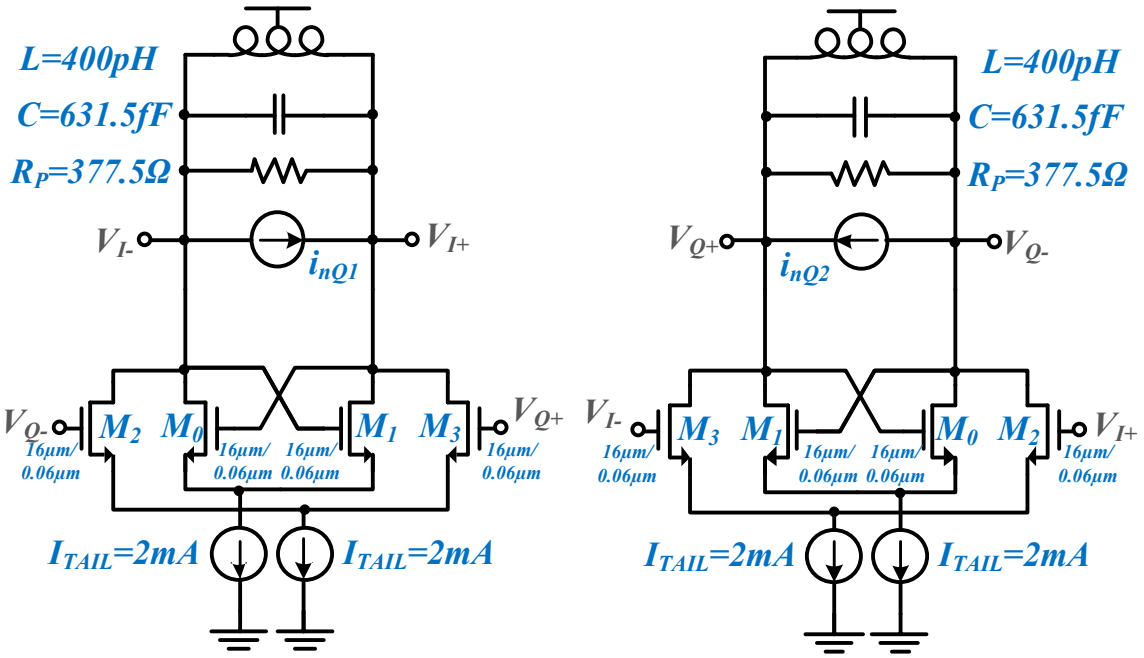

Figure 2.27: *Quadrature LC-oscillator schematic in low resonance mode with noise sources of interest highlighted* (i_{nQ1}, i_{nQ2})

The phase noise is depicted in Figure **2.28** and Table 2.

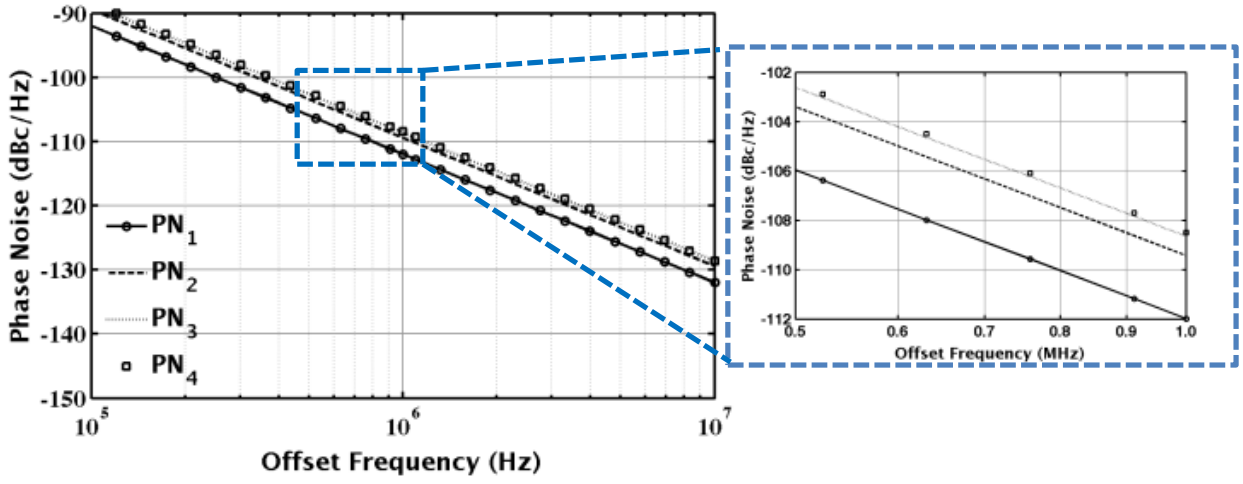

Figure 2.28: *Phase noise plots for circuit shown in Figure* **2.27**

Table 2: *Phase noise evaluated for the quadrature LC-tank at 1MHz*

	Settings	Noise Sources	PN@1MHz dBc/Hz
PN_1	Expression (2.50) (Hand calculation)	Thermal	-111.987
PN_2	Expression (2.49) (simulated oscillation amplitude)	Thermal	-109.431
PN_3	Expression (2.34) (simulated GM and ISF)	Thermal	-108.644
PN_4	Simulated PSS+PNOISE - ideal tail current	Thermal	-108.498

The theoretical expression captures the thermal noise correctly once the amplitude is corrected from the $2I_{TAIL}R_P/\pi$ estimation to the actual voltage swing. In order to study the impact from coupling strength on the phase noise, the coupling strength is swept. In order to avoid having to resize transistors, to maintain current density, this simulation was performed using a Verilog-A model of the transistor that uses the tanh nonlinearity as described by equation (2.43). The exact Verilog-A code is presented in Figure **2.29**.

```
module Diff_GMC (vin_p, vin_n, iop, ion) ;
 input vin_p, vin_n;
 output iop, ion;
 electrical vin_p, vin_n, iop, ion ;


 parameter real gm = 1;
 parameter real IT = 1e-6;
 parameter real kb=1.38e-23;
 parameter real gamma=1;
 parameter real ennoi=0;

    real vin, outp, outn;

    analog begin

      vin =V(vin_p) - V(vin_n);

    outp = IT/2 - IT/2*tanh(2*gm/IT*vin)
                + white_noise(ennoi*4*kb*$temperature*gamma*gm/pow(cosh(gm*vin/IT),2),"thermal");
    outn = IT/2 + IT/2*tanh(2*gm/IT*vin)
                + white_noise(ennoi*4*kb*$temperature*gamma*gm/pow(cosh(gm*vin/IT),2),"thermal");

    I(iop) <+  outp;
    I(ion) <+  outn;
    end
endmodule
```

Figure 2.29: *Verilog-A code for a differential tanh-G_M used to replace transistors in simulation*

Using the model, the same simulation shown in Figure **2.27** is repeated and the resulting ISFs are shown in Figure 2.30, and the corresponding phase noise is shown in Figure **2.31** and tabulated in Table 3 at 1MHz. The theoretical result *PN1* matches that of the real transistor circuit (with a slight difference due to frequency shift resulting from real transistor parasitics). The rest of the phase noise expressions match each other to a great degree as expected.

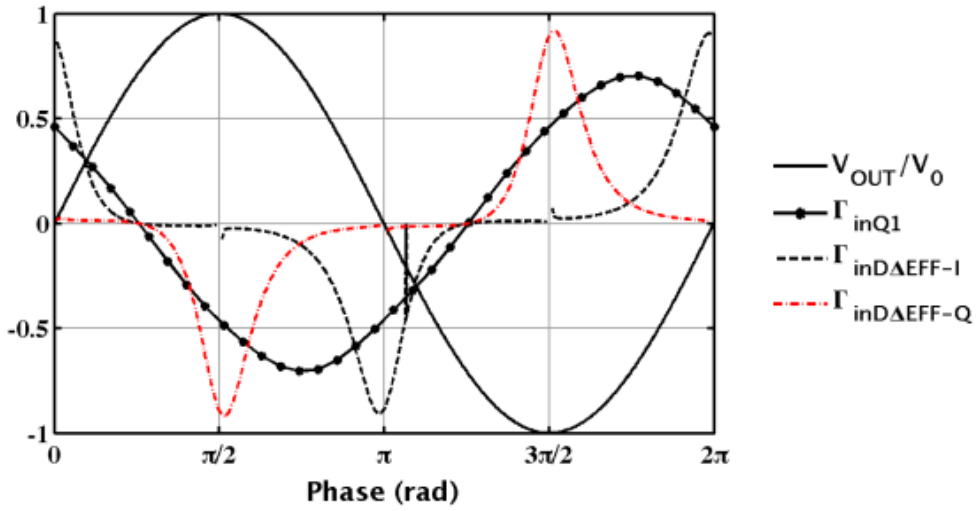

Figure 2.30: *The normalize output voltage waveform and the Impulse sensitivity function of the output phase to noise injected at the noise sources indicated in Figure* 2.27*using Verilog-A* G_M *as described by Figure* 2.29

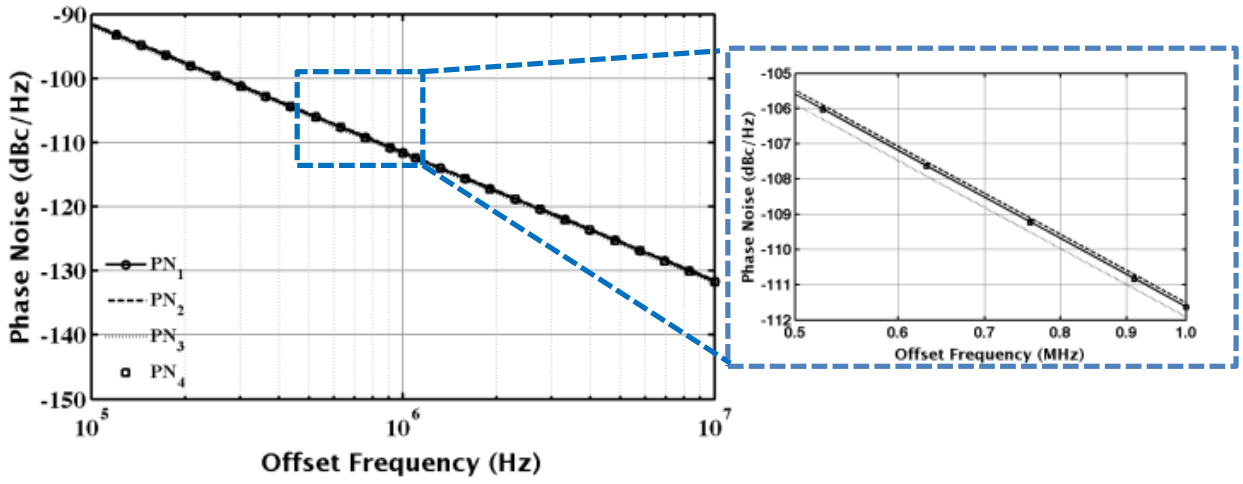

Figure 2.31: *Phase noise plots for circuit shown in Figure* **2.27***using Verilog-A* G_M *as described by Figure* **2.29**

Table 3: *Phase noise evaluated for the quadrature LC-tank at 1MHz using Verilog-A G_M described by Figure* 2.29

	Settings	Noise Sources	PN@1MHz dBc/Hz
PN_1	Expression (2.50) (Hand calculation)	Thermal	-111.625
PN_2	Expression (2.49) (simulated oscillation amplitude)	Thermal	-111.516
PN_3	Expression (2.34) (simulated GM and ISF)	Thermal	-111.919
PN_4	Simulated PSS+PNOISE - ideal tail current	Thermal	-111.643

Using the aforementioned model and quadrature circuit, the coupling strength k, which is in this case equal to I_Q/I_I is swept. The observable increase in phase noise matches the expected behavior from the theoretical expression very well, and it diverges slightly at higher coupling factors as simulated ISFs diverge from theoretical ISFs due to diverging from ideal switching condition. It's important to note that at coupling strength close to 0.1, the quadrature has theoretically little impact on the phase noise.

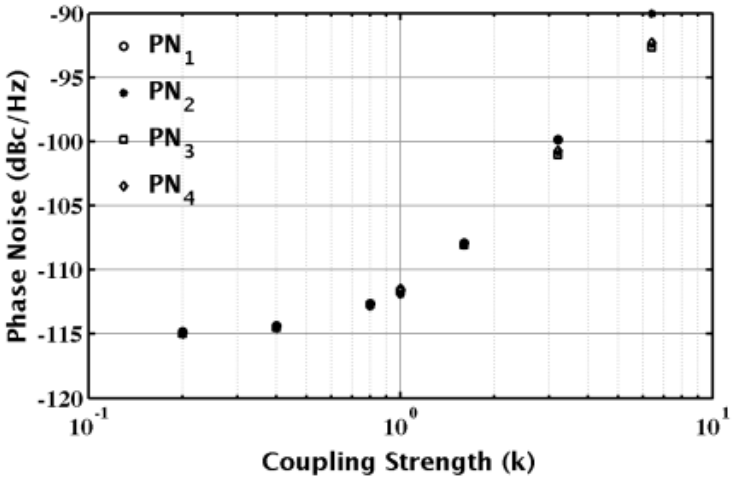

Figure 2.32: *Phase noise sweep versus $k=I_Q/I_I$, for circuit shown in Figure* **2.27***using Verilog-A G_M as described by Figure* **2.29**

From the previous discussion it appears that a weaker coupling is advantageous. However, a weaker coupling has two disadvantages: (1) Narrower locking range between the two quadrature oscillators. If the quadrature oscillators unlock then neither quadrature, nor the 3dB phase noise

improvement due to coupling two oscillators can be obtained. (2) Quadrature phase error. The quadrature phase error refers to the divergence of the quadrature angle of the desired 90° angle. The 90° angle is guaranteed by the symmetry between the two oscillating cores and the path delays that comprise the quadrature oscillator. Any mismatches in this symmetry due to unbalanced layout, or fabrication process and mismatch variation between the two different oscillation cores, will lead to an overall quadrature phase error. An expression for such error was derived using generalized Alder's equations in [23] as:

$$\Delta\varphi = \frac{|\sin(\Psi)|}{\frac{I_Q}{I_I}+|\cos(\Psi)|}\frac{\Delta I}{2I} - \frac{|\sin(\Psi)|}{\frac{I_Q}{I_I}+|\cos(\Psi)|}\frac{\Delta I_Q}{2I_Q} - \frac{1+\left(\frac{I_Q}{I_I}\right)^2+2\frac{I_Q}{I_I}|\cos(\Psi)|}{\frac{I_Q}{I_I}\left(\frac{I_Q}{I_I}+|\cos(\Psi)|\right)}Q\frac{\Delta\omega}{\omega_0} + \frac{\left(1+\frac{I_Q}{I_I}|\cos(\Psi)|\right)|\sin(\Psi)|}{\frac{I_Q}{I_I}+|\cos(\Psi)|}\frac{\Delta R}{R}+\frac{\Delta\Psi}{2} \tag{2.61}$$

where ΔI is the difference between the tail bias currents of the two oscillator cores, ΔI_Q is the difference between the tail bias currents of the two coupling stages between the oscillators, and Q is the quality factor of the LC-tank, $\Delta\omega$ is the difference in the oscillation frequency of the two cores, ΔR is the difference in the parallel resistance of the two LC-tanks and $\Delta\Psi$ is the difference between the extra phase delay in the quadrature path between the two cores. For a Ψ=90° this simplifies to:

$$\Delta\varphi = \left(\frac{I_Q}{I_I}\right)^{-1}\frac{\Delta I}{2I} - \left(\frac{I_Q}{I_I}\right)^{-1}\frac{\Delta I_Q}{2I_Q} - \left(1+\left(\frac{I_Q}{I_I}\right)^{-2}\right)Q\frac{\Delta\omega}{\omega_0} + \left(\frac{I_Q}{I_I}\right)^{-1}\frac{\Delta R}{R}+\frac{\Delta\Psi}{2} \tag{2.62}$$

This shows that aside from the error due to path mismatch captured by $\Delta\Psi$ term, the phase error is inversely proportional to I_Q/I_I which means stronger coupling results in a reduced phase error for the same mismatches between the two cores.

Chapter 3

PROPOSED QVCO ARCHITECTURES AND ANALYSIS

3.1. Introduction

This chapter introduces two new QVCO architectures: an actively coupled dual-resonance QVCO and a passively coupled dual-resonance QVCO. Both architectures use the same core dual-resonance VCO. The chapter analyzes two key aspects of the proposed dual-resonance VCO's, namely startup, and phase noise.

The startup analysis is performed by introducing a network simplification technique that enables the reduction of the 4^{th} order dual-resonator based network into a 2^{nd} order network. With such simplification, the startup condition is readily found based on the theory introduced in Section 2.4.4 for the second order LC-tank VCO. The result is verified for a number of cases using a complete derivation of startup condition of the actual 4^{th} order system using both Nyquist and Root locus methods as summarized in Section 2.4.5.

The phase noise analysis presented in this chapter extends the discussion of Section 2.5.3 to quantify the contributions of three design elements, namely resonator quality factor, oscillation amplitude and device noise to the phase noise of the dual-resonance VCO. The analysis is done in three steps: a) an effective quality factor is derived for the coupled resonator after reducing the fourth-order network to a second-order one, b) the voltage amplitude across the terminals of the resonator is obtained at the edge of the current-limited oscillation regime, and c) the ISF and noise modulating functions for cyclostationary noise sources are obtained in order to compute their contributions to the phase noise of the oscillator.

In order to extend the previous analysis to the two quadrature oscillators, the active quadrature impact introduced in Section 2.6 is extended using the 2nd order equivalent circuit obtained after network simplification. This is quantified using circuit simulations to compute the ISF, which is then used to analytically predict the phase noise, and then using direct phase noise simulations in SpectreRF for the two quadrature oscillators. The phase noise thus obtained is then compared to the phase noise of the dual-resonance single VCO.

Finally, the phase accuracy of the quadrature oscillators is analyzed by considering: a) the constant phase shift introduced by capacitive imbalances in the passive QVCO loop and its frequency dependence, and b) circuit mismatches impact on both active and passive QVCOs as quantified using a series of statistical Monte Carlo simulations.

3.2. The Proposed QVCO Architectures

The current study aims at comparing and contrasting two methods of quadrature coupling; namely, passive and active quadrature coupling when applied to wide-band dual-resonance tuned QVCOs.

As it has been introduced earlier in the quadrature coupling section, passive quadrature coupling, if applied properly, has the advantage of not introducing orthogonal current phasors. Alternatively, it uses coupled resonators to introduce a phase shift, which corresponds to creating a 3rd oscillation loop enforcing the oscillation and improving the circuit's phase noise.

The two architectures studied by this work are shown side by side in Figure **3.1**. The coupled resonance VCO shown in Figure 3.2 is the main building of both architectures. It consists of a coupled resonance tank, a positive feedback transconductance (negative impedance) at one terminal of coupled resonator and a second positive feedback transconductance between the two terminals. The resonator is a two port system that can be represented by its impedance

parameters matrix (Z-matrix). Given the Z-matrix, the system can be simplified into a basic linear feedback system as shown in Figure 3.2.

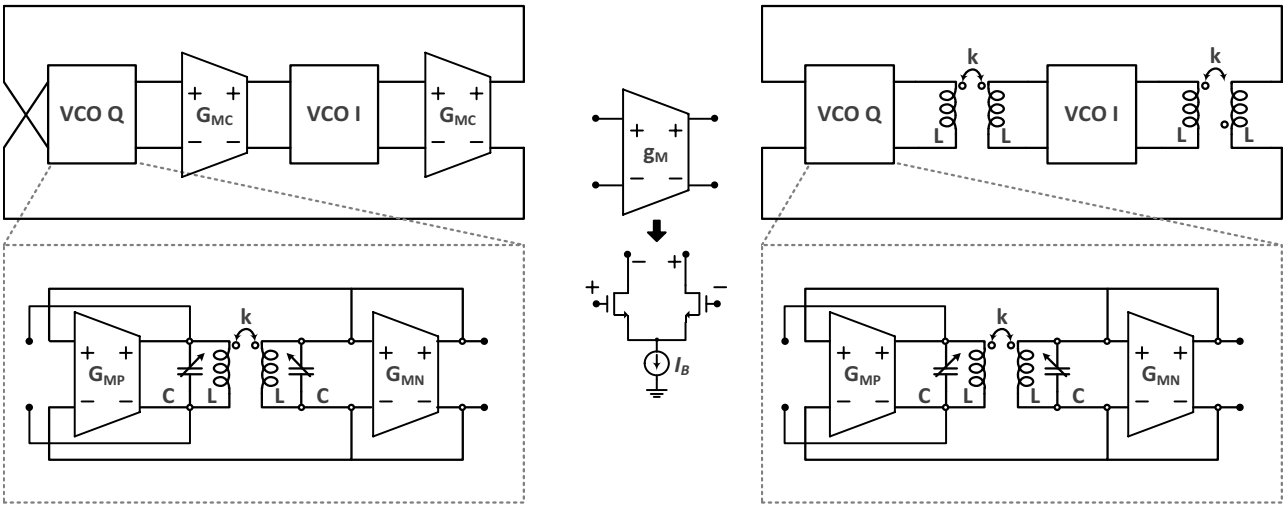

(a) (b)

Figure 3.1: *(a) Passive and (b) active quadrature voltage controlled oscillator architectures with dual-resonance mode coupled resonator tanks*

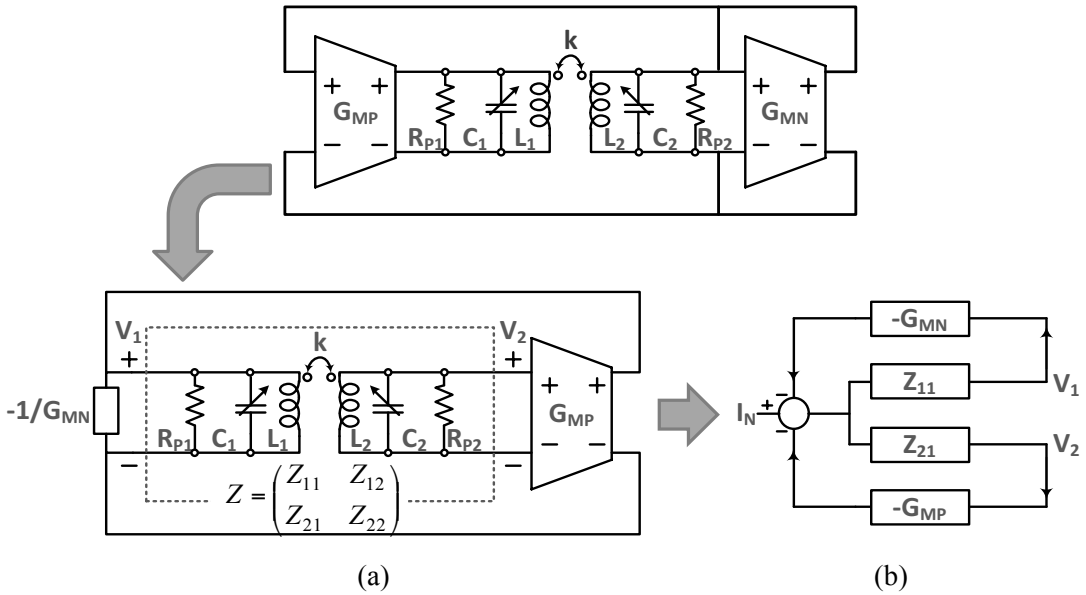

(a) (b)

Figure 3.2: *A coupled resonance oscillator with two transconductance elements forming two feedback loops and the system representation of this circuit*

The coupled resonator VCO can be represented by the following set of system equations:

$$H(s) = \frac{V_1}{I_N}(s) = \frac{Z_{11}(s)}{1 - G_{MP}Z_{21}(s) - G_{MN}Z_{11}(s)}$$
$$H_2(s) = \frac{V_2}{I_N}(s) = \frac{Z_{21}(s)}{1 - G_{MP}Z_{21}(s) - G_{MN}Z_{11}(s)} \quad (3.1)$$
$$\alpha(s) = \frac{V_2}{V_1}(s) = \frac{Z_{21}(s)}{Z_{11}(s)}$$

Note that $H(s)$ and $H_2(s)$ share the same poles and startup condition and differ in the small signal voltage amplitudes only.

3.3. 2nd Order Simplification of a 4th Order Dual-Resonator Network

This section aims at reducing the 4th order dual-resonance circuit to a conventional 2nd order resonator which has been analyzed in Chapter 2. This is achieved by developing a relationship between the voltages on both sides of the resonator, and using an equivalent model for the mutual coupling in the resonator. The combination of the two allows for the shorting of the resonator terminals which yields a 2nd order resonator.

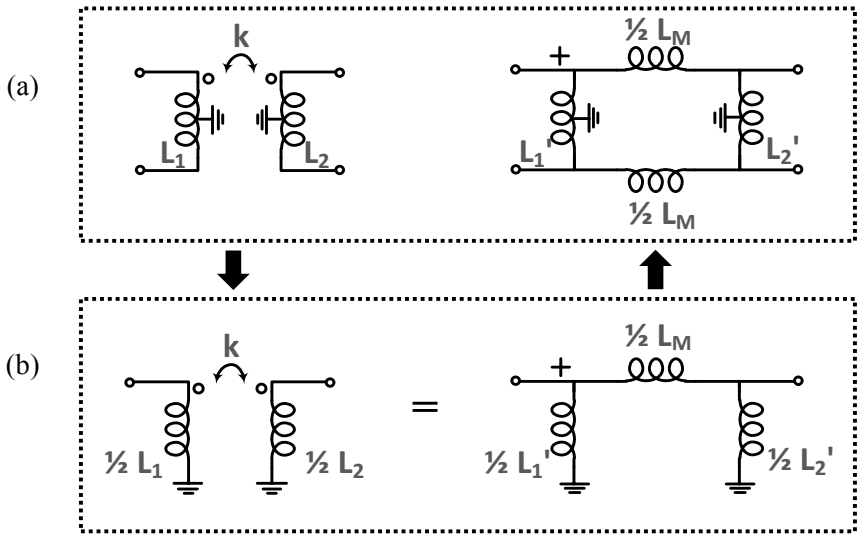

Figure 3.3: (*a*) *Equivalent Pi-model of coupled center-tapped inductors, and* (*b*) *the corresponding half-circuit equivalent models*

The basis of the simplification relies on the equivalent Pi-model of the coupled center-tapped inductors shown in Figure 3.3(a). Due to symmetry around the center tap, the half circuit model, shown in Figure 3.3(b), is considered, and extended to the fully differential case. While this assumption is not always true, it is true for all circuits considered in this work.

The equivalent model parameters are derived by equating the Z-parameters of the two half circuit-models:

$$\frac{1}{2}\begin{pmatrix} L_1 & k\sqrt{L_1L_2} \\ k\sqrt{L_1L_2} & L_2 \end{pmatrix} = \frac{1}{2\left(L_1'+L_2'+L_M\right)}\begin{pmatrix} L_1'\left(L_2'+L_M\right) & L_1'L_2' \\ L_1'L_2' & L_2'\left(L_1'+L_M\right) \end{pmatrix} \tag{3.2}$$

The resultant parameters L_1', L_2', L_M are therefore given by the following equations:

$$L_1' = \frac{1-k^2}{1-\sqrt{L_1/L_2}k}L_1 \qquad L_2' = \frac{1-k^2}{1-\sqrt{L_2/L_1}k}L_2 \qquad L_M = \frac{1-k^2}{k}\sqrt{L_1L_2} \tag{3.3}$$

The coupled center-tapped inductor simplification is applied to the dual-resonance circuit presented in Figure 3.2, and the resultant circuit is shown in Figure 3.4.

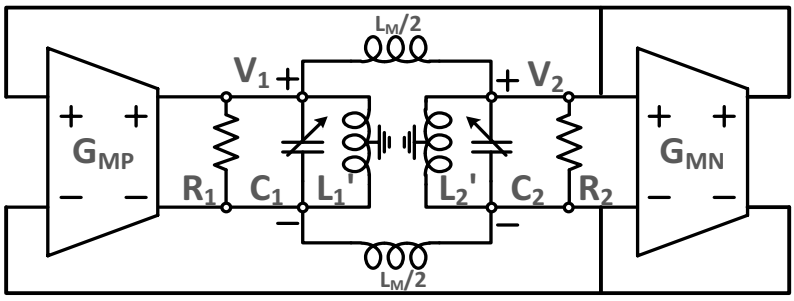

Figure 3.4: *The coupled resonance oscillator with the mutual inductance replaced by the differential Pi-model*

In order to simplify this 4th order circuit to 2nd order equivalent, the nodes V_1 and V_2 need to be reduced to a single node. In order to achieve that, the ratio of the voltage $\alpha = V_2/V_1$ is computed. If α is a real number, the circuit parameters, can be scaled in a manner that sets $V_1=V_2$ while maintaining the impedance seen on one of the two nodes. The two nodes are therefore reduced

into a single node. The reduction is presented over the following steps: (1) the inductors $L_M/2$ are split into two separate inductors at nodes V_1 and V_2, (2) the real voltage ratio (α) is derived, (3) the assumption of real voltage ratio (α) is validated and (4) the circuit parameters are scaled to equate voltages V_1 and V_2.

3.3.1. The Splitting of Inductor L_M

The inductance $L_M/2$ in Figure 3.4 can be eliminated by splitting it into separate impedances. This is achieved, as shown in Figure 3.5, by equating the impedances Z_1 and Z_2 seen at the two terminals of the inductance $L_M/2$.

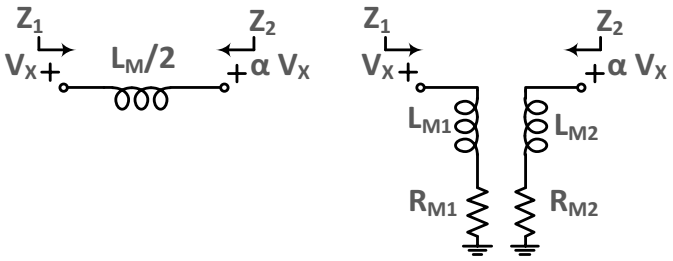

Figure 3.5: *The splitting of a 2-terminal inductance into two single terminal inductances by equating impedances Z_1 and Z_2*

The two impedances are derived as:

$$Z_1 = \frac{sL_M/2}{1-\alpha} \qquad Z_2 = \frac{sL_M/2}{1-\alpha^{-1}} \tag{3.4}$$

For a complex valued voltage ratio (α), the impedances are complex and can be split into inductances and resistances as shown in Figure 3.5, by setting $L_{M1,2}$=Im[$Z_{1,2}$]/ω, and $R_{1,2}$=Re[$Z_{1,2}$]. For a real α, the impedances are imaginary, and the resistances $R_{1,2}$ reduce to zero. In such case, the circuit in Figure 3.4, can be represented by the circuit in Figure 3.6:

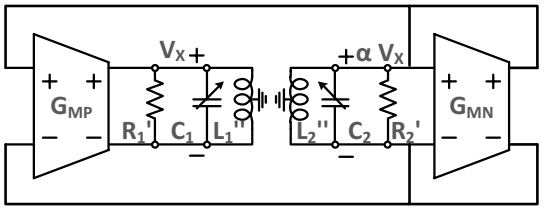

$$L_M = \frac{1-k^2}{k}\sqrt{L_1 L_2}$$

$$L_1'' = \frac{1-k^2}{1-\sqrt{L_1/L_2}\,k} L_1 \,//\, \frac{jL_M}{1-\alpha}$$

$$L_2'' = \frac{1-k^2}{1-\sqrt{L_2/L_1}\,k} L_2 \,//\, \frac{L_M}{1-\alpha^{-1}}$$

Figure 3.6: *The coupled resonance oscillator's Pi model broken into two parts for a given voltage ratio α*

3.3.2. The Derivation of the Voltage Ratio (α)

The voltage ratio has already been given for a general case by equation (3.1) as the ratio of the two impedances $Z_{21}(s)/Z_{11}(s)$ of the coupled resonator network. While this expression is valid at all frequencies, we are mostly interested in evaluating α at resonance. Since there are two resonance frequencies, there are two possible α values for any dual-resonance network.

The values of α at resonance can be found from the circuit in Figure 3.6 by observing that the resonance frequency is the same for every node in the coupled resonator. This indicates that at resonance, $L_1'' C_1 = L_2'' C_2$. Using this equation, and the term $\zeta = \frac{\omega_2}{\omega_1}$, α is found to be:

$$\alpha = \left(\frac{1-\zeta^2}{2k} \pm \sqrt{\left(\frac{1-\zeta^2}{2k}\right)^2 + \zeta^2} \right) \sqrt{\frac{L_2}{L_1}} \tag{3.5}$$

For the case where the inductance ratio is 1, the ratio is plotted in Figure 3.7. Note that there will always be a positive and negative α values, where the positive value is bounded by *1/k* and the negative is unbounded. This can create large unwanted swings.

When considering the special case where the tank is symmetric as before, $\alpha = \pm 1$. These two cases have been presented in the literature as *Odd* and *Even* resonance modes of the coupled resonator.

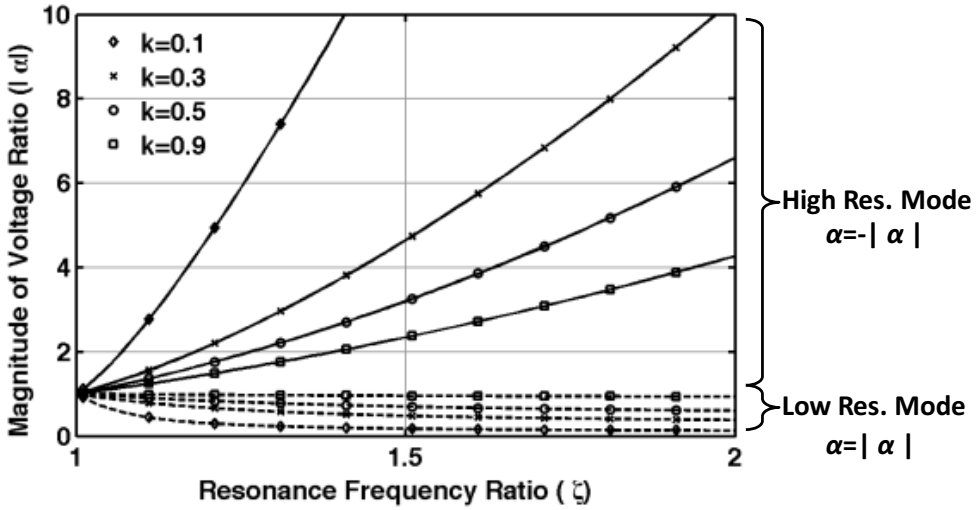

Figure 3.7: *A plot of the voltage swing ratio at the two nodes of the coupled resonance oscillator as a function of the ratio of the resonance frequencies of the two resonators prior to coupling* (ζ) *for 5 mutual coupling factors* (*k*)

3.3.3. The Validity of the Real Voltage Ratio (α) Assumption

The assumption that the voltage ratio (α) is real is justified under infinite quality factor condition. In such condition, all impedances in the circuit are imaginary (inductive or capacitive), and hence the ratio of the voltages, which in turn is a ratio of impedances, is a real number (α). In order to verify this assumption for real circuit components, a Cadence Spectre AC simulations were conducted in which the coupled resonator presented in Figure 3.14 was considered.

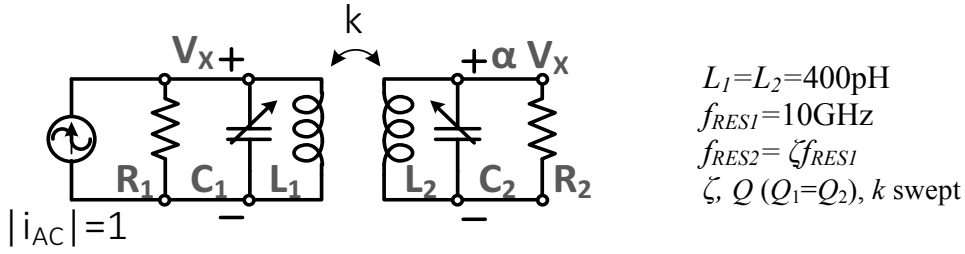

Figure 3.8: *The test structure for validating the real voltage ratio* (α) *assumption*

The first AC simulation computed the phase of voltage ratio (α) over a wide frequency range that includes both resonance frequencies. The second AC simulation computed both the magnitude and the phase of voltage ratio (α) at only the resonance frequencies. In both simulations the

coupling factor k, the quality factor Q and the frequency ratio factor ζ were swept. The results of the first simulation are presented in **Figure 3.9** and **Figure 3.11**, and the results of the second simulation are presented in **Figure 3.10 Figure 3.12**, for k=0.5, 0.3 respectively.

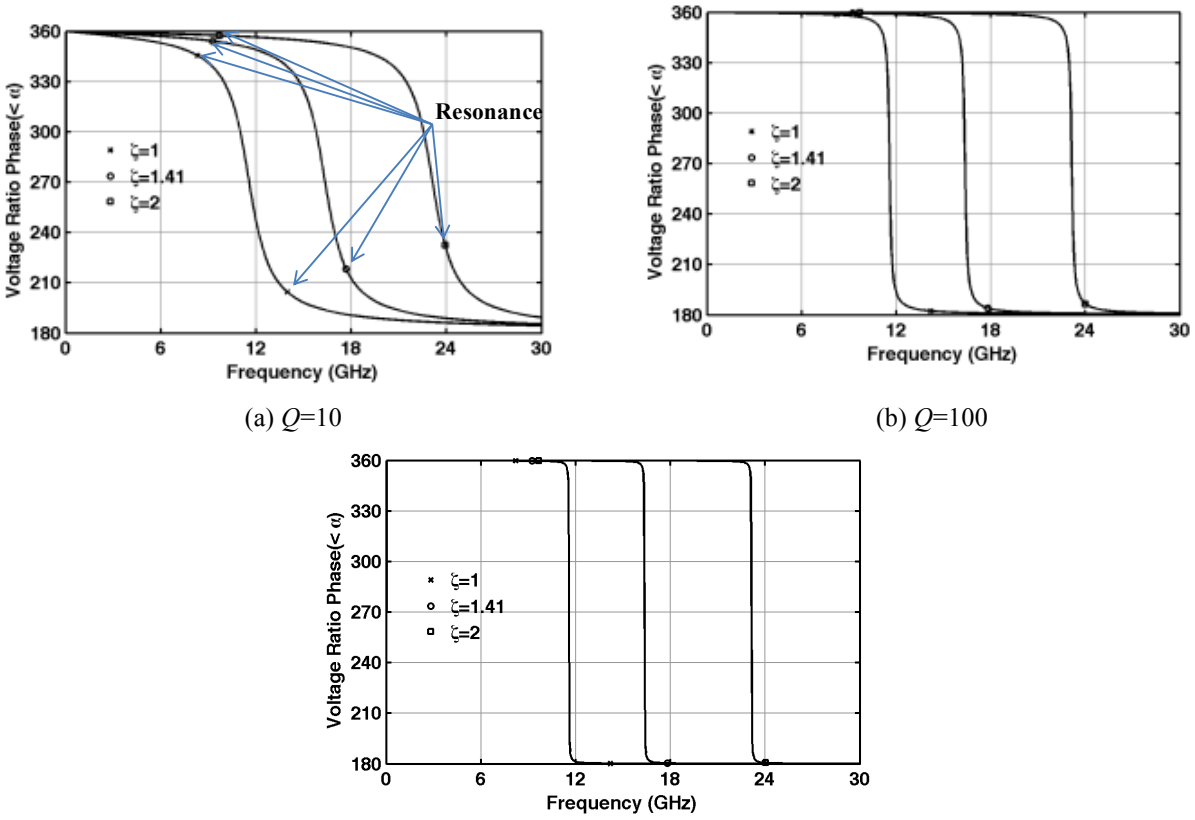

(a) Q=10 (b) Q=100

(c) Q=1000

Figure 3.9: *The phase of the voltage ratio* (α) *vs. frequency for Q=10, 100, 1000 and coupling factor k=0.5. Each plot considers three frequency ratios ζ, and the resonance frequencies are marked*

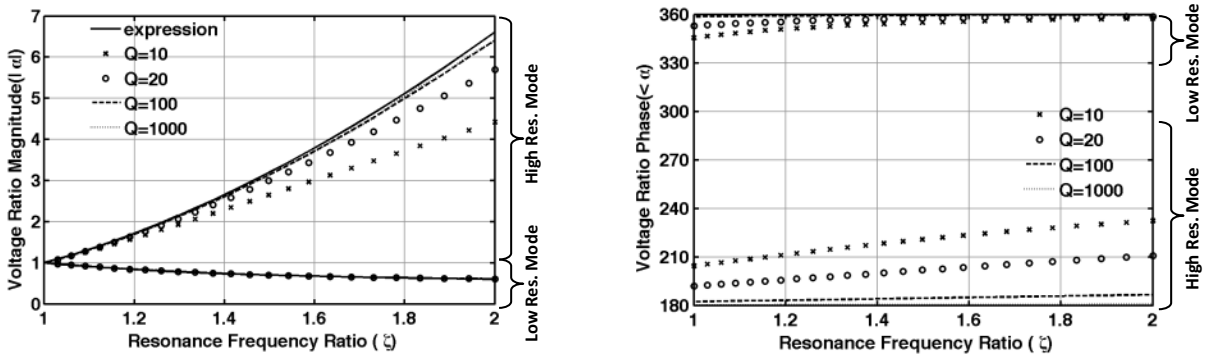

(a) (b)

Figure 3.10: *The* (*a*) *magnitude and* (*b*) *phase of the voltage ratio* (α) *at resonance vs. frequency ratios ζ frequency for Q=10, 20,100, 1000 and coupling factor k=0.5. The plot marked expression is the plot of the α as derived in equation* (*3.4*)

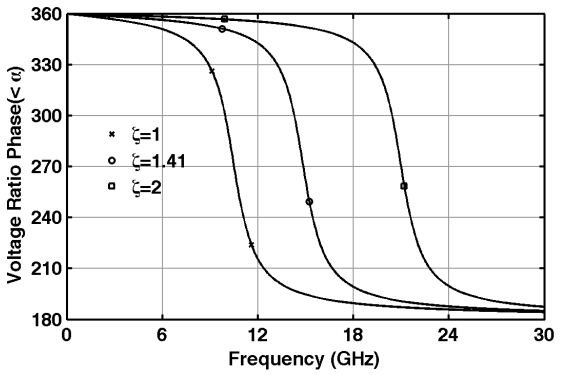

(a) Q=10

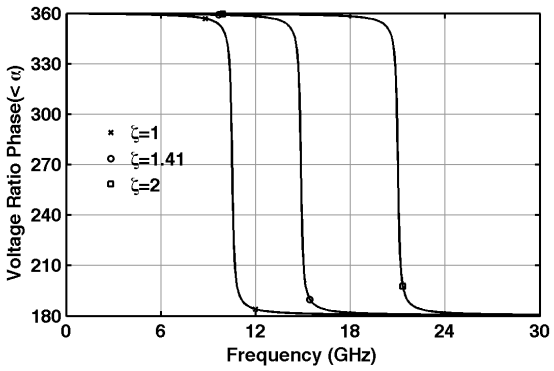

(b) Q=100

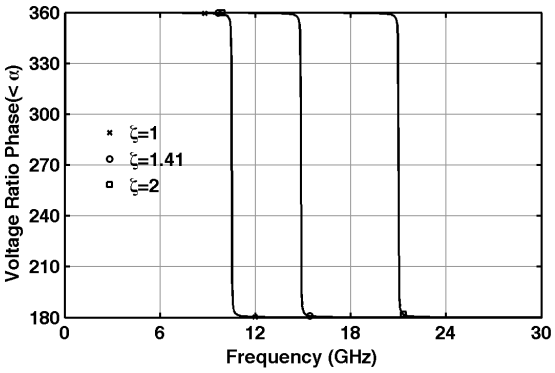

(c) Q=1000

Figure 3.11: *The phase of the voltage ratio* (α) *vs. frequency for Q=10, 100, 1000 and coupling factor k=0.3. Each plot considers three frequency ratios* ζ*, and the resonance frequencies are marked*

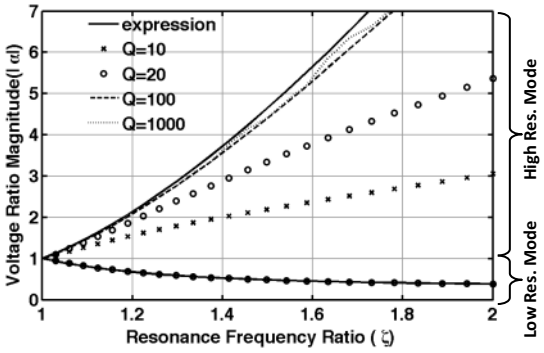

(a)

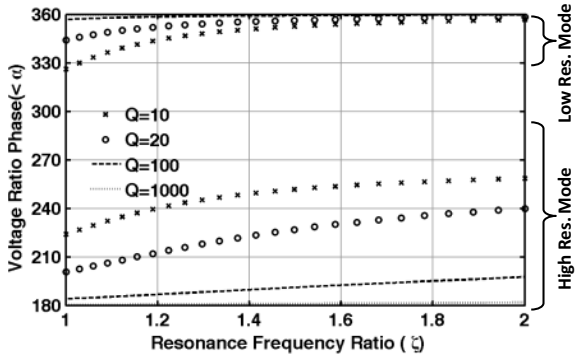

(b)

Figure 3.12: *The* (*a*) *magnitude and* (*b*) *phase of the voltage ratio* (α) *at resonance vs. frequency ratios* ζ *frequency for Q=10, 20,100, 1000 and coupling factor k=0.3. The plot marked expression is the plot of the* α *as derived in equation* (*3.4*)

From the previous simulation, one can conclude that under the high quality factor assumption, the expression in equation (3.4) is correct. However, for realistic quality factors of Q in the range

of 10 to 20, the assumption of a real α is more accurate (1) for lower resonance mode than the higher resonance mode (significantly), (2) for a stronger coupling factor (k), (3) for a higher frequency ratio (ζ) in the case of the lower resonance mode and (4) for a lower frequency ratio (ζ) in the case of the higher resonance mode.

Despite the inaccuracies, the circuit cannot be further reduced into a 2nd order network without the assumption of a real α.

3.3.4. Circuit Parameter Scaling and Final Reduction

The circuit in Figure 3.6 is further reduced by scaling the voltage on both resonance nodes to be equal as shown in Figure 3.13. The voltages on both resonators are set to be equal by scaling the impedances to maintain the same currents. This preserves the overall impedance at one of the nodes. Given equal voltages, the two terminals can be connected. This simplified second order circuit can be used to derive a generalized quality factor parameter as well as startup conditions.

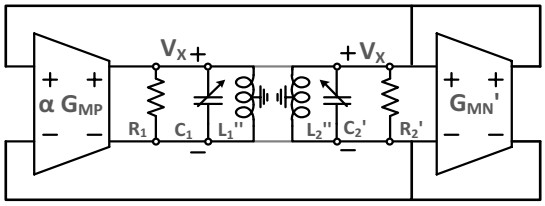

$$L_M = \frac{1-k^2}{k}\sqrt{L_1 L_2}$$

$$L_1'' = \frac{1-k^2}{1-\sqrt{L_1/L_2}\,k} L_1 \,//\, \frac{L_M}{1-\alpha}$$

$$L_2'' = \frac{1}{|\alpha|}\left(\frac{1-k^2}{1-\sqrt{L_2/L_1}\,k} L_2 \,//\, \frac{L_M}{1-\alpha^{-1}}\right)$$

$$R_2' = \frac{1}{|\alpha|} R_2 \quad C_2' = |\alpha| C_2 \quad G_{MN}' = |\alpha| G_{MN}$$

Figure 3.13: *The second order resonator representation of the fourth order coupled resonator*

For a symmetric resonator, the overall expression simplifies to that shown in Figure 3.14. This corresponds to the *Odd* and *Even* modes of resonance. The concept of *Odd* and *Even* modes can be extended to the circuit in Figure 3.14, by observing that for a positive $\alpha>0$, the L_M terms cancel between L_1'' and L_2'', which can be thought of as an even mode. If $\alpha<0$, the L_M terms in L_1'' and

L_2'' are equal and they add up, which can be thought of as an odd mode. This is an indication to weather currents flow through the original L_M'.

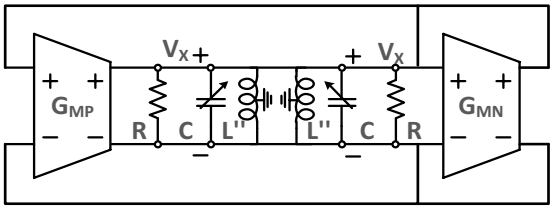

$$L'' = (1+k)L \,//\, \frac{1}{1-\alpha}\frac{1-k^2}{k}L \quad \alpha = \pm 1$$
$$L'' = (1 \pm k)L$$

Figure 3.14: *The second order resonator representation of the fourth order symmetric coupled resonator* (*consisting of two identical resonators coupled*)

3.4. The Resonance Frequency of a Dual-Resonance Oscillator

To verify the validity of the model, and assuming α>0, the resonance frequency is given by:

$$\omega_{H,L} = \frac{1}{\sqrt{(L_1'' \,//\, L_2'')(C_1 \,//\, C_2')}} = \frac{1}{\sqrt{\left(\frac{\left(1-k^2\right)L_1L_2}{L_2 - \alpha k\sqrt{L_1L_2}} \,//\, \frac{\left(1-k^2\right)L_1L_2}{\alpha L_1 - k\sqrt{L_1L_2}}\right)(C_1 + \alpha C_2)}}$$
$$\omega_{H,L} = \sqrt{\frac{\left(1+\zeta^2\right)\omega_1{}^2 \pm \sqrt{\left(1+\zeta^4\right)\omega_1{}^4 + \zeta^2\omega_1{}^4\left(2-4\left(1-k^2\right)\right)}}{2(1-k^2)}} \tag{3.6}$$

This expression matches that previously derived in (2.12), and combines the result is obtained for α<0. This expression is plotted in Figure 3.15.

The plot normalizes the resonance frequency in the high resonance mode to the higher uncoupled resonance frequency, and similarly, normalizes the resonance frequency in the low resonance mode to the low uncoupled resonance frequency ($\omega_H/Max[\omega_{1,2}]$, $\omega_L/Min[\omega_{1,2}]$). The actual high to low resonance frequency ratio (ω_H/ω_L) requires scaling by a factor (ζ). As evident in the plot, a symmetric tank with matching initial frequencies (ζ=1) yields the most frequency separation,

and consequently achieves the highest maximum frequency in the high frequency resonance mode.

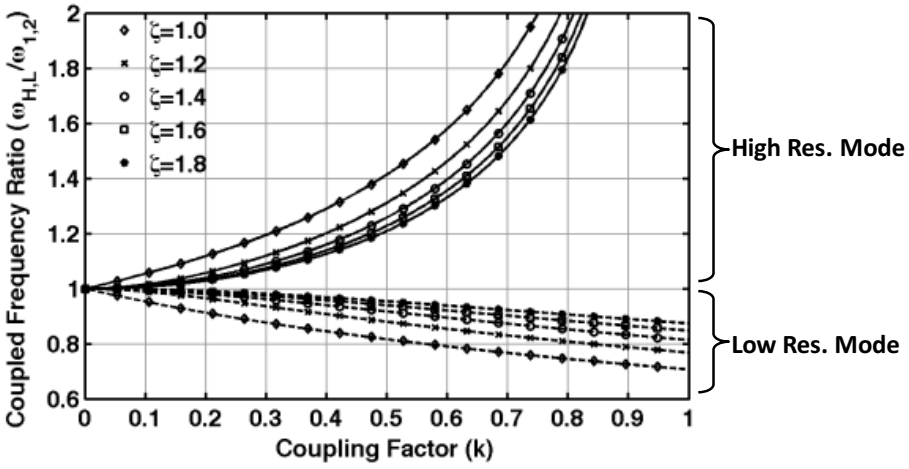

Figure 3.15: *The ratio of the of the coupled resonator's resonance frequencies to the uncoupled resonance frequency ($\omega_{1,2}$) versus the mutual coupling factors (k) for a 6 ratios of the uncoupled resonance ($\zeta = \omega_2/\omega_1$).*

3.5. Effective Quality Factor of Dual-Resonance Oscillator

Given the 2nd order network simplification of the dual resonator, the quality factor of the effective resonator can be derived by considering the overall resistance and capacitance at the merged node:

$$Q_{H,L} = \omega_{H,L}\left(R_1 // R_2'\right)\left(C_1 // C_2'\right) = \omega_{H,L}\frac{R_1 R_2'}{R_1 + R_2'}(C_1 + |\alpha| C_2) \tag{3.7}$$

The parallel tank resistances R_1 and R_2 are lumped parameters, derived from the inductor's and capacitor's parasitic series resistances. The impact of dual-resonance on the overall quality factor depends on whether the capacitance or the inductance dominates the quality factor of the uncoupled resonators. To clarify, a symmetric dual-resonance network can be considered. For the symmetric case, the quality factors are given by:

$$Q_{H,L} = \omega_{H,L}\left(\frac{R}{2}\right)(2C) \tag{3.8}$$

Where $R_1=R_2=R$ is the parallel resistance of the dual resonator, *derived after coupling*. And $C=C_1=C_2$ is the capacitance of the uncoupled resonator. R is therefore the parallel combination of the capacitor's effective parallel resistance, and the coupled inductor's effective parallel resistance. As shown in Figure 3.16, the coupled inductor's effective parallel resistance corresponds to the quality factor of the coupled inductor L'' and not the uncoupled inductor L. Since the resistance R_{LS} remains unchanged, and the effective inductance L'' is $(1 \pm k)\, L$ as given by Figure 3.14. , the quality factor of the coupled inductor ($Q_{L''}$) equals $(1 \pm k)\, Q_L$. The quality factor of the capacitor remains unchanged. The overall quality factor is given by the parallel combination of the two.

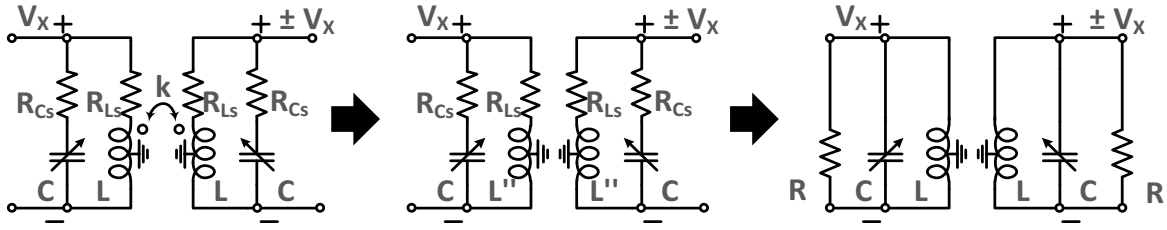

Figure 3.16: *The derivation of the lumped parallel resistance R of a symmetric coupled resonator from the parasitic series resistance of the inductors and capacitors*.

This indicates that at lower frequencies where the inductance quality factor dominates, dual-resonance leads to a boost of the quality factor of one resonance mode, at the expense of the dropping of the quality factor in the other, for a symmetric resonator's case. While at higher (mm-wave frequencies), where the quality factor of the capacitance dominates, this impact is reduced and the coupled quality factor of a symmetric coupled resonator approaches that of the uncoupled one.

A quality factor expression is derived for a non-symmetric coupled resonator where (1) quality factor dominated by inductance Q, (2) the coupled inductors are symmetric ($L_1=L_2=L$ and

$Q_{L1}=Q_{L2}=Q_L$) and (3) The tuning capacitors are different, and α depends on the ratio of the tuning capacitors. In this case, the parallel resistances R_1 and R_2 are given by:

$$R_1 \approx \omega \frac{L_1''}{L_1} L_1'' Q_{L1} \quad R_2' \approx \omega \frac{L_2''}{L_2} L_2'' Q_{L2} \tag{3.9}$$

Where Q_{L1} and Q_{L2} are the quality factor of the uncoupled inductors. The quality factor is therefore given by the expression:

$$Q_{H,L} = \frac{(1 \pm k)^2 (1 \mp \alpha)(1 \mp k)}{\left(1 - 4k\alpha + \alpha^2 + k^2 (1 + \alpha^2)\right)} Q_L \tag{3.10}$$

To appreciate the result, consider the plot in Figure 3.17. A ratio Q_R equal to $Q_{H,1}/Q_L$ is plotted against the swept frequency ratio ζ. The value α is implicitly derived as in (3.5) and Figure 3.7. It can be seen that for low coupling ratio a symmetrical resonator can achieve equal Quality factors in the coupled resonator modes which are close to the original Q_L of the uncoupled resonator.

As coupling factor increases, an enhancement of the quality factor of one resonance mode (low frequency, even mode), comes at the cost of degradation in the quality factor in the other mode. This has been considered in the literature and designs that employ capacitive as well as inductive coupling were suggested[7][13]. However, this can be similarly achieved by creating imbalance in the resonance frequency ratio (ζ).

It is important to note that this imbalance in resonance frequency ratio results in unequal voltage magnitudes at the two resonance nodes. It also results in a reduction in the frequency separation between the high and low resonance modes for the same coupling factor (k).

Even if such imbalance was created, in order to equate the quality factors in the two resonance modes, the resulting quality factor will always be less than that of the original quality factor of the uncoupled inductor.

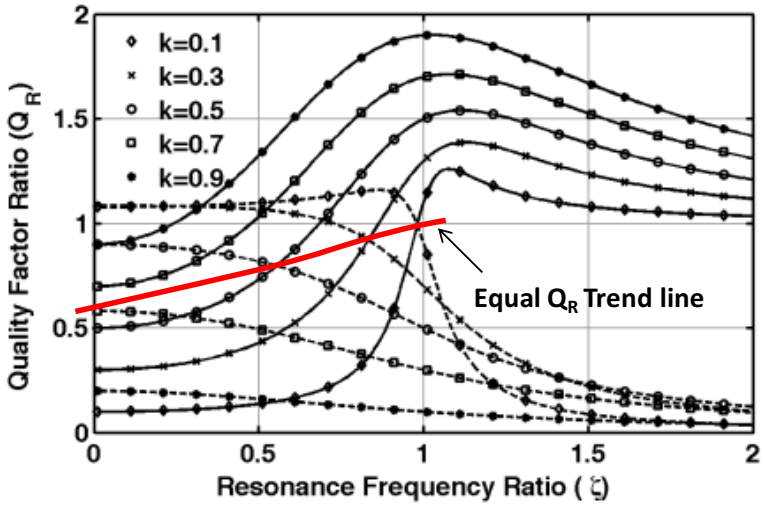

Figure 3.17: *The ratio of the quality factor of a coupled resonator consisting of two identical inductors tuned differently (ζ) to the original quality factor of the inductors when the coupled resonator's quality factor is dominated by that of the inductors*

3.6. Startup Condition of the Dual-Resonance Oscillator

Based on the previous analysis, and using equation (2.20), the startup condition is:

$$G_{MN} + Sign[\alpha]G_{MP} > \frac{R_1 + |\alpha|^{-1} R_2}{R_1 R_2} \tag{3.11}$$

Where R_1, R_2 are defined for the tank whose Q is inductance dominated as before in equation (3.9). For a symmetric dual resonance tank, this simplifies to:

$$G_{MN} + Sign[\alpha]G_{MP} > \frac{2}{R} \tag{3.12}$$

The startup condition of the dual-resonance circuit can also be derived using both Nyquist and root locus methods as summarized in (2.26). Firstly, the overall circuit is broken into two circuits that can be linearly superposed as shown in Figure 3.18.

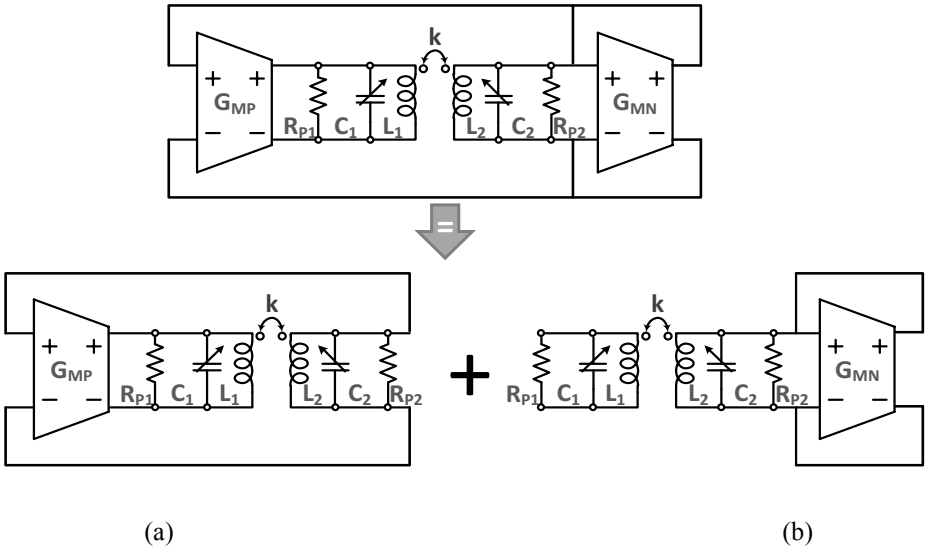

(a) (b)

Figure 3.18: *Decomposing the dual-resonance oscillator into two circuits that can be linearly superposed, namely:* (*a*)*the two terminal negative feedback loop and* (*b*) *the single terminal negative gm loop*

Oscillation is achieved if either of the two loops meets the oscillation condition. These two circuits can be described by their feedback system representations in Figure 3.19 where the Z parameters are given by the:

$$Z = \frac{1}{\Delta}\begin{pmatrix} \left(s^3 + \left(\frac{\omega_2}{Q_2}\right)s^2 + \left(\frac{{\omega_2}^2}{1-k^2}\right)s\right)L_1{\omega_1}^2 & \frac{k}{1-k^2}\sqrt{L_1L_2}\,{\omega_1}^2{\omega_2}^2 s \\ \frac{k}{1-k^2}\sqrt{L_1L_2}\,{\omega_1}^2{\omega_2}^2 s & \left(s^3 + \left(\frac{\omega_1}{Q_1}\right)s^2 + \left(\frac{{\omega_1}^2}{1-k^2}\right)s\right)L_2{\omega_2}^2 \end{pmatrix} \tag{3.13}$$

$$\Delta = s^4 + \left(\frac{\omega_1}{Q_1} + \frac{\omega_2}{Q_2}\right)s^3 + \left(\frac{\omega_1}{Q_1}\frac{\omega_2}{Q_2} + \frac{{\omega_1}^2 + {\omega_2}^2}{1-k^2}\right)s^2 + \frac{1}{1-k^2}\left(\frac{\omega_1{\omega_2}^2}{Q_1} + \frac{\omega_2{\omega_1}^2}{Q_2}\right)s + \frac{{\omega_1}^2{\omega_2}^2}{1-k^2}$$

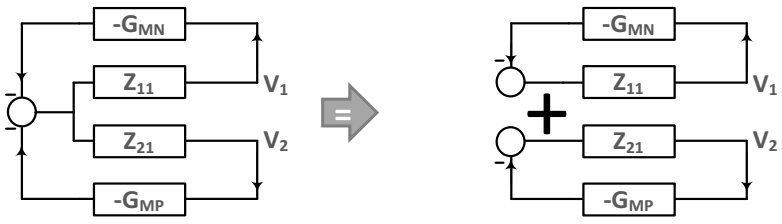

Figure 3.19: *System representation of the linear decomposition where the Z-parameters* (Z_{11},Z_{21}) *are described in* Figure **3.2**

3.6.1. Nyquist Criterion and Root Locus Method

Based on the theory summarized in section 2.4.5, and with reference to the Z-parameters presented in equation (3.13), the startup condition can be given by the combination of G_M and ω at resonance. Since both Nyquist and Root Locus yield the same set of equations, given the restrictions defined in section 2.4, the analysis is combined.

The resonance frequency (ω) and the required G_M for startup of the G_{MP}, Z_{21} loop are given by the following equations:

Root Locus	**Nyquist Criterion**
$\mathrm{Im}[D(Z_{21}(j\omega))] = G_{MP}\,\mathrm{Im}[N(Z_{21}(j\omega))]$	$\mathrm{Re}[Z_{21}(j\omega)] = {G_{MP}}^{-1}$

$$G_{MP} = \frac{1}{k\sqrt{R_1 R_2}}\left(\left(\frac{\omega^2}{{\omega_1}^2}\left(1-k^2\right)-1\right)\sqrt{\frac{\omega_1 Q_1}{\omega_2 Q_2}} + \left(\frac{\omega^2}{{\omega_2}^2}\left(1-k^2\right)-1\right)\sqrt{\frac{\omega_2 Q_2}{\omega_1 Q_1}}\right) \tag{3.14}$$

Root Locus	**Nyquist Criterion**
$\mathrm{Re}[D(Z_{21}(j\omega))] = G_{MP}\,\mathrm{Re}[N(Z_{21}(j\omega))]$	$\mathrm{Im}[Z_{21}(j\omega)] = 0$

$$\omega^2 = \frac{\left({\omega_1}^2 + {\omega_2}^2 + \frac{\omega_1}{Q_1}\frac{\omega_2}{Q_2}\left(1-k^2\right)\right) \pm \sqrt{\left({\omega_1}^2 + {\omega_2}^2 + \frac{\omega_1}{Q_1}\frac{\omega_2}{Q_2}\left(1-k^2\right)\right)^2 - 4{\omega_1}^2{\omega_2}^2\left(1-k^2\right)}}{2\left(1-k^2\right)} \tag{3.15}$$

Under high quality factor approximation, equation (3.15) reduces to (3.6). Similarly, the resonance frequency (ω) and the required G_M for startup the startup of the G_{MN}, Z_{11} loop is given by the following equations:

Root Locus	**Nyquist Criterion**
$\mathrm{Im}[D(Z_{11}(j\omega))] = G_{MN}\,\mathrm{Im}[N(Z_{11}(j\omega))]$	$\mathrm{Re}[Z_{11}(j\omega)] = {G_{MN}}^{-1}$

$$G_{MN} = \frac{1}{R_1}\left(1 + \frac{\frac{\omega_2}{Q_2}\left(\omega^2\left(1-k^2\right) - {\omega_1}^2\right)}{\frac{\omega_1}{Q_1}\left(\omega^2\left(1-k^2\right) - {\omega_2}^2\right)}\right) \tag{3.16}$$

Root Locus	Nyquist Criterion
$\mathrm{Re}[D(Z_{11}(j\omega))] = G_{MN}\ \mathrm{Re}[N(Z_{11}(j\omega))]$	$\mathrm{Im}[Z_{11}(j\omega)] = 0$

$$\left(1-k^2\right)\omega^4 + \left(\left(G_{MN}R-1\right)\left(1-k^2\right)\frac{\omega_1}{Q_1}\frac{\omega_2}{Q_2} - \left({\omega_1}^2+{\omega_2}^2\right)\right)\omega^2 + {\omega_1}^2{\omega_2}^2 = 0 \tag{3.17}$$

One can apply the previous equations to the symmetric tank, with frequencies derived with a high quality factor approximation. The startup conditions are:

$$|\,G_{MP}\,| > \frac{2}{R} \qquad \omega^2 = \frac{1}{1\mp k^2}{\omega_0}^2 \tag{3.18}$$

$$G_{MN} > \frac{2}{R} \qquad \omega^2 = \frac{1}{1\mp k^2}{\omega_0}^2 \tag{3.19}$$

Since G_{MN} is always positive, equation (3.19) indicates that resonance can be achieved using the G_{MN} , Z_{11} loop regardless of the resonance frequency. This could theoretically lead to the presence of multiple resonances at the same time.

On the other hand, G_{MP} can be positive or negative. Equation (3.18) indicates that resonance can be achieved using the G_{MP}, Z_{21} loop for two values of $G_{MP} > 2/R$, and $G_{MP} < -2/R$. These two startup-conditions correspond to two different frequencies, where a positive G_{MP} corresponds to the high frequency resonance mode and the negative G_{MP} corresponds to the low frequency resonance mode. Since α=1 for the high frequency resonance mode and α=-1 for the low frequency resonance mode, the same startup condition can be expressed as $Sign(\alpha)G_{MP} > \frac{2}{R}$ which corresponds to equation (3.12). The sign of G_{MP} is used as to select the resonance-mode.

3.7. Phase Noise of the Dual-Mode Resonance Oscillator (high resonance mode)

The Impulse sensitivity is evaluated, similar to the analysis performed on the LC-tank oscillator in Chapter 2.5.6. Consider the dual resonance circuit shown in Figure **3.20**. For the sake of

simplicity and using an argument of symmetry, only the noises from the half circuit are considered. One should note that since this test circuit relies on a fixed parallel resistance (R_P), it resembles the case where the quality factor of the tank is dominated by the capacitance, and doesn't account for the impact on quality factor which was captured (3.10), which will be considered later.

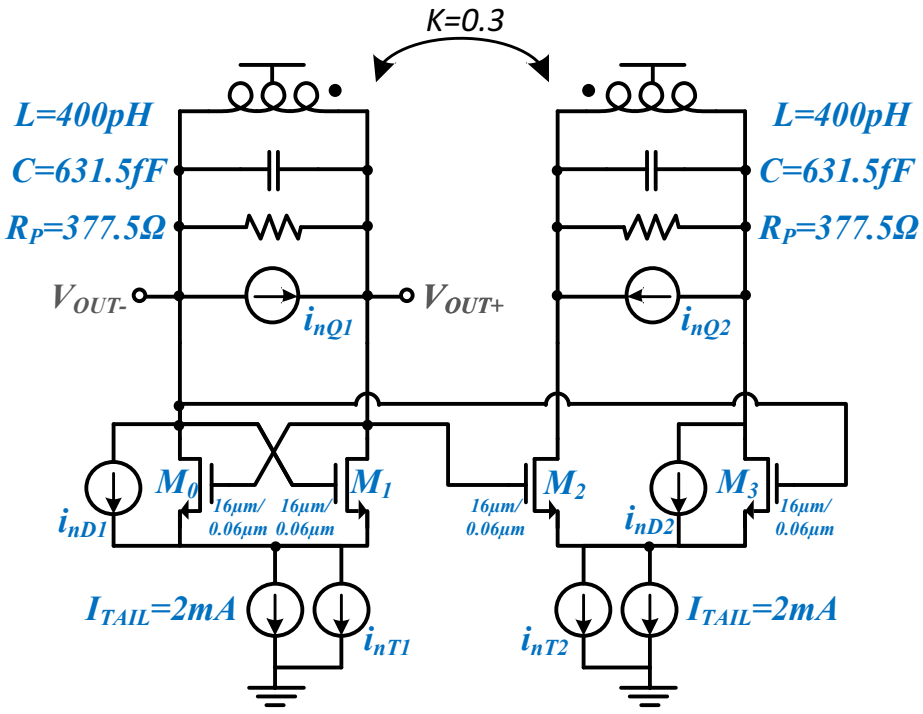

Figure 3.20: *Dual resonance cross coupled LC-oscillator schematic in high resonance mode with noise sources of interest highlighted* (i_{nQ1}, i_{nD1}, i_{nT1}, i_{nQ2}, i_{nD2}, i_{nT2})

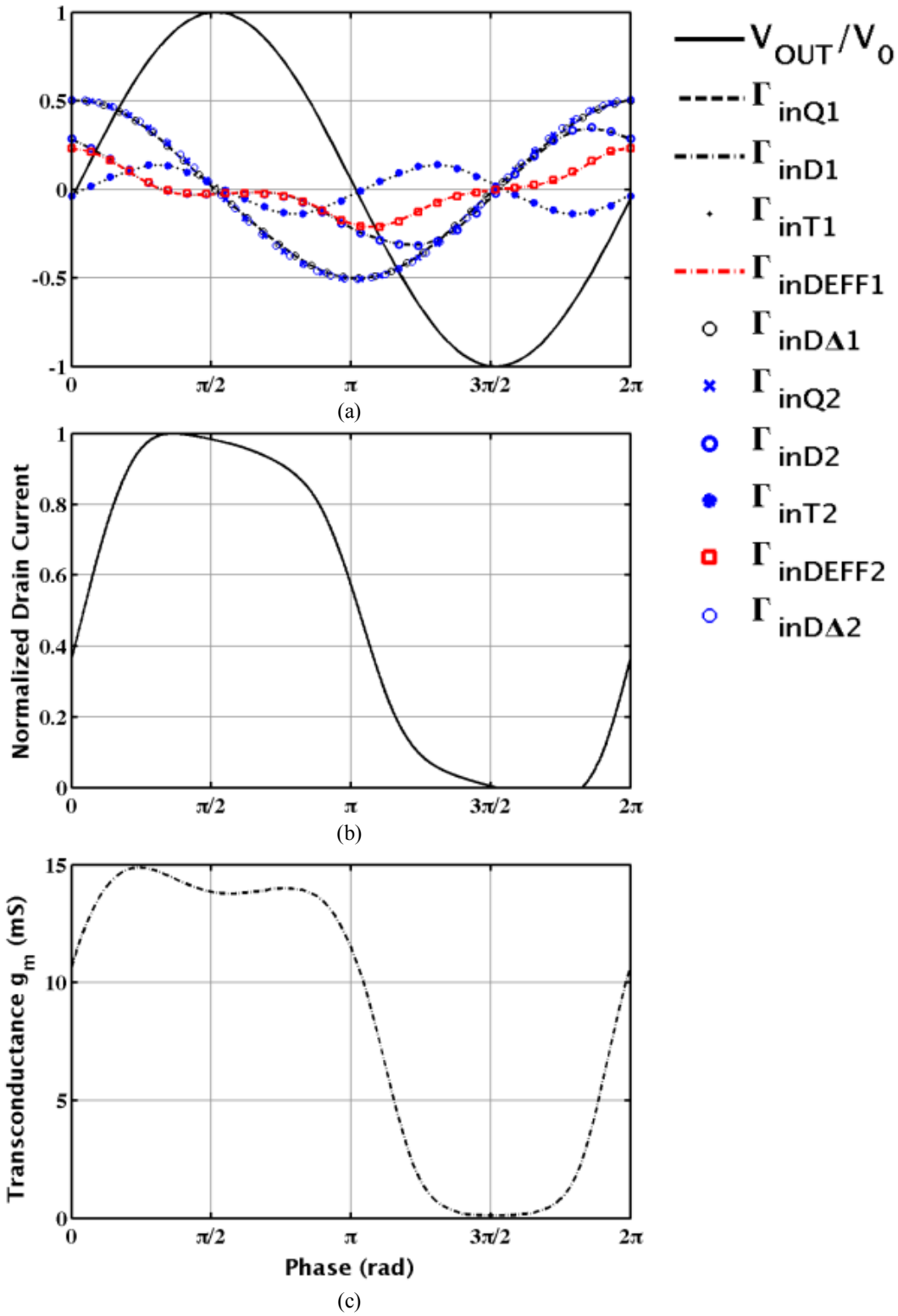

Figure 3.21: (*a*) *The normalize output voltage waveform and the Impulse sensitivity function of the output phase to noise injected at the noise sources indicated in Figure* 3.20 , (*b*) *the normalized drain current of the transistor* M_0 *and* (*c*) *the corresponding transconductance* g_m

The inductance, capacitance and parasitic resistance, as well as the transistors were sized similarly to those in Figure **2.18** to compare the performance of the dual resonance oscillator to the LC-tank oscillator. The ISF plots for the circuit in Figure **3.20** are presented in Figure 3.21. As can be seen in the figure, the ISF for the tanks are

(1) *The tanks noise ISFs* ($\Gamma_{inQ1,2}$) are approximately a sinusoid with amplitude equal to 1 and a phase offset of π/4 from the output voltage waveform with half the amplitude of that of the LC-tank oscillator. This result is expected based on equation (2.38) for n=2.

(2) *The transistors noise ISFs* ($\Gamma_{inD1,2}$) behave the same as that of the LC-tank oscillator scaled by the factor ½ similar to $\Gamma_{inQ1,2}$.

(3) *The differential transistor noise ISF* ($\Gamma_{inD\Delta1,2}$) given by the difference between the two ISFs from transistors M_0 and M_1 for $\Gamma_{inD\Delta1}$, and transistors M_2 and M_3 for $\Gamma_{inD\Delta2}$ are equal to the tank noise ISFs ($\Gamma_{inQ1,2}$).

(4) *The effective transistor noise ISF* ($\Gamma_{inDEFF1,2}$) which captures the impact of the cyclostationary noise from the transistors are the same as those of the LC-tank scaled by a factor of ½. The transconductance and drain current of the transistors are the same of the LC tank. Note that in order to maintain the same output swing twice the current was used in the dual-resonance circuit as that in the basic LC-tank. Since the output voltage is the tail current for each differential pair is the same as that of the LC-tank, the overall transconductance is expected to remain the same.

(5) *The tail current noise ISF* ($\Gamma_{inT1,2}$) behave the same as that of the LC-tank oscillator scaled by the factor ½ similar to all other ISFs.

3.7.1. The 2nd Order Simplification of the test circuit

The dual resonance circuit can be simplified according to the theory discussed in Chapter 3.3. While the analysis was intended for a small signal linear model of the circuit, it can be loosely extended to the circuit schematic with non-linear elements such as transistors, as long as the describing functions of the nonlinear blocks is maintained. For this analysis to be strict, one should consider the different parasitic capacitance of transistors at the two oscillating nodes. If the parasitic capacitance is ignored, the resulting reduction of the circuit in Figure **3.20** is shown in Figure **3.22**.

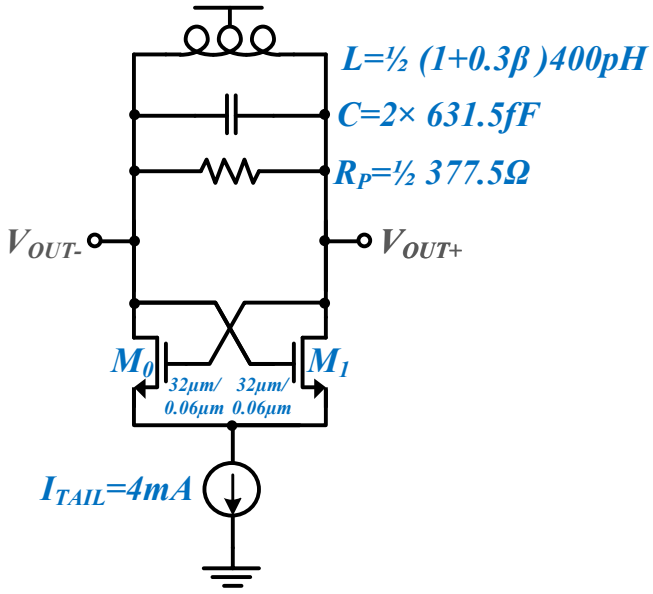

Figure 3.22: *Reduced model of the dual-resonance cross coupled LC-oscillator schematic*

Based on the circuit in Figure **3.22**, the following is the expected performance of dual-resonance circuit in the high resonance mode (β=-1) compared to the LC-tank circuit in Figure **2.18**:

(1) The resonance frequency is √1.42·.

(2) The amplitude is the same (2· the bias current and ½· the tank resistance).

(3) The phase noise is ½· (2· the tank capacitance and ½· the tank resistance).

3.7.2. Phase noise simulation results

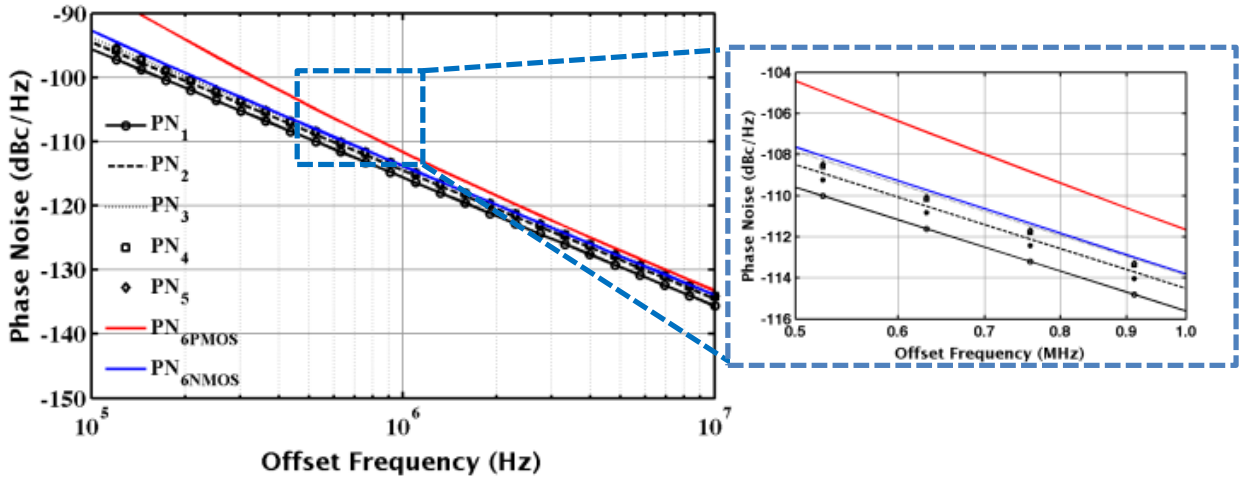

Figure 3.23: *Phase noise plots for circuit shown in Figure* **3.20**

The phase noise is obtained from the ISF functions according to equation (2.34) and plotted in Figure **2.23**. The plots use the same legend as was previously described in Chapter 2.5.6. The results are further tabulated for offset frequencies 10 kHz and 1 MHz in Table 4.

Table 4: *Phase noise evaluated for the LC-tank at 10kHz, 1MHz for a number of cases for dual-resonance circuit*

	Settings	**Noise Source**	**PN@10kHz** dBc/Hz	**PN@1MHz** dBc/Hz
PN_1	Expression (2.50) (Hand calculation)	Thermal	-75.575	-115.575
PN_2	Expression (2.49) (simulated oscillation amplitude)	Thermal	-74.482	-114.482
PN_3	Expression (2.34) (simulated GM and ISF)	Thermal	-73.831	-113.831
PN_4	Simulated PSS+PNOISE - ideal tail current	Thermal	-74.141	-114.139
PN_5	Simulated PSS+PNOISE - ideal tail current	Thermal+1/*f*	-71.891	-114.081
PN_{6PMOS}	Simulated PSS+PNOISE - PMOS bias current source	Thermal+1/*f*	-56.755	-111.621
PN_{6NMOS}	Simulated PSS+PNOISE - NMOS bias current source	Thermal+1/*f*	-68.257	-113.772
PN_7	Simulated 2nd order simplification - ideal tail current	Thermal	-74.432	-114.793

The simulation results agree with the expectations based on the reduced circuit model in this resonance mode.

3.8. Phase Noise of the Dual-Mode Resonance Oscillator (low resonance mode)

The Impulse sensitivity is evaluated, similar to the analysis performed on the LC-tank oscillator in Chapter 2.5.6 for the dual-resonance oscillator operating in the lower resonance mode for the circuit shown in Figure **3.24**.

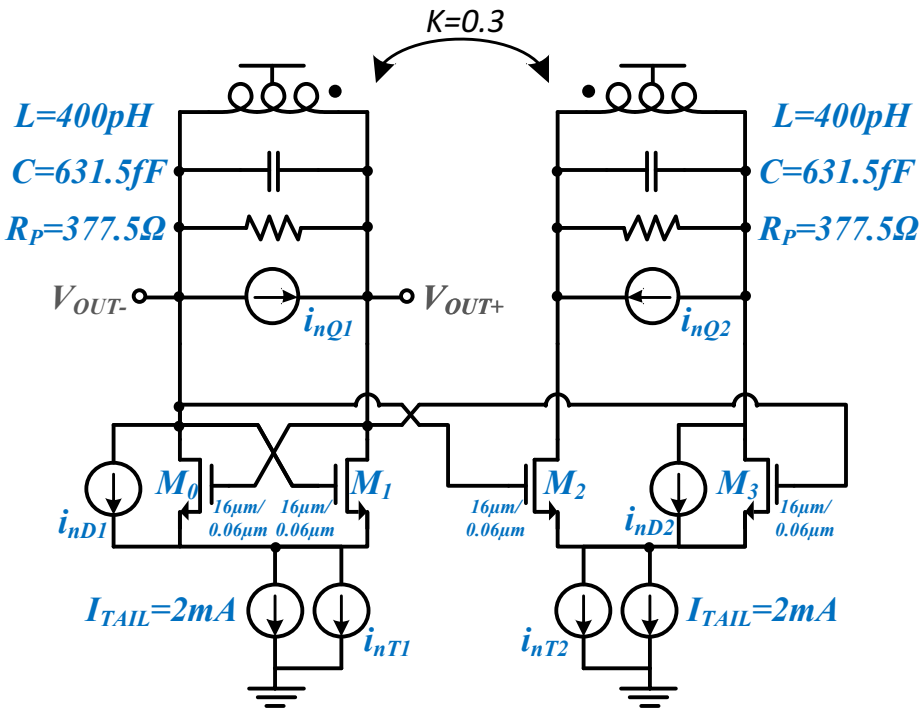

Figure 3.24: *Dual resonance cross coupled LC-oscillator schematic in low resonance mode with noise sources of interest highlighted* (i_{nQ1}, i_{nD1}, i_{nT1}, i_{nQ2}, i_{nD2}, i_{nT2})

Similar to the high resonance mode, the circuit can be reduced to the LC-tank circuit in Figure **3.24**, where β=1 for the low resonance mode. Consequently, the performance of the dual-resonance oscillator compared to the LC-tank circuit in Figure **2.18**:

(1) The resonance frequency is √0.77·.

(2) The amplitude is the same (2· the bias current and ½· the tank resistance).

(3) The phase noise is ½· (2· the tank capacitance and ½· the tank resistance).

The voltage waveforms and ISFs are depicted in Figure 3.25, while the phase noise is depicted in Figure **3.26** and Table 5.

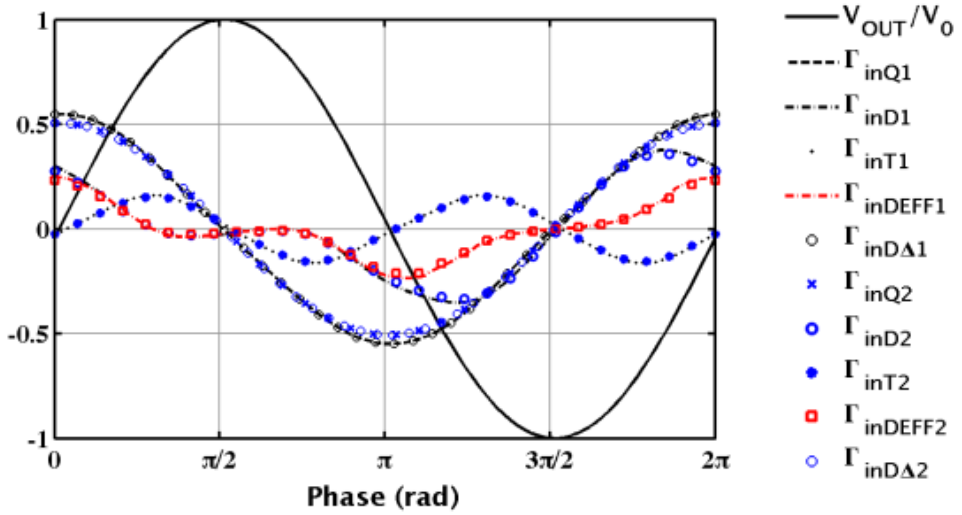

Figure 3.25: *The normalize output voltage waveform and the Impulse sensitivity function of the output phase to noise injected at the noise sources indicated in Figure* 3.24

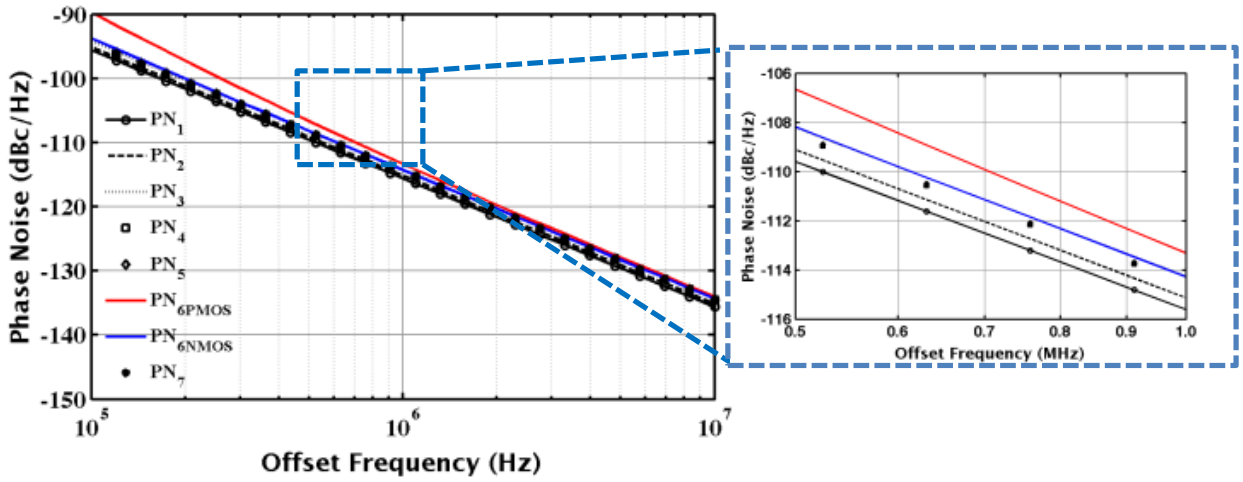

Figure 3.26: *Phase noise plots for circuit shown in Figure* **3.24**

Table 5: *Phase noise evaluated for the LC-tank at 10kHz, 1MHz for a number of cases for dual-resonance circuit*

	Settings	Noise Sources	PN@10kHz dBc/Hz	PN@1MHz dBc/Hz
$\mathbf{PN_1}$	Expression (2.50) (Hand calculation)	Thermal	-75.575	-115.575
$\mathbf{PN_2}$	Expression (2.49) (simulated oscillation amplitude)	Thermal	-75.097	-115.097
$\mathbf{PN_3}$	Expression (2.34) (simulated GM and ISF)	Thermal	-74.205	-114.205
$\mathbf{PN_4}$	Simulated PSS+PNOISE - ideal tail current	Thermal	-74.525	-114.523
$\mathbf{PN_5}$	Simulated PSS+PNOISE - ideal tail current	Thermal+1/*f*	-73.179	-114.485
$\mathbf{PN_{6PMOS}}$	Simulated PSS+PNOISE - PMOS bias current source	Thermal+1/*f*	-61.964	-113.273
$\mathbf{PN_{6NMOS}}$	Simulated PSS+PNOISE - NMOS bias current source	Thermal+1/*f*	-70.657	-114.242
$\mathbf{PN_7}$	Simulated 2nd order simplification - ideal tail current	Thermal	-74.459	-114.456

3.9. Phase Noise of the Dual-Mode Resonance Oscillator Summary

The simulation results in both high and low resonance modes of the dual-resonance oscillator agree with the reduced order model under the condition that the describing functions of the non-linear elements in the circuit can be maintained. That effectively requires consuming twice as much current as a single oscillator, with the advantage of keeping the same voltage swing and halving the phase noise.

Therefore, the phase noise per power consumed ratio of the dual resonance oscillator is the same as that of a basic LC-tank oscillator. However, the maximum allowable power (limited by Voltage) swing is twice as large as that of the LC-tank oscillator. This is only the case under the assumption that the circuit is to be operated at maximum allowable voltage swing (edge of current limited regime). For example, if the dual-resonance circuit is to be operated at the same current consumption as the original LC-tank VCO, the phase noise of the dual-resonance VCO is 2· that of the LC-tank. This is due to the fact that phase noise scales with the total DC bias current (I_{DC}) as approximately $1/I_{DC}^2$. To summarize, for a fixed DC power, the basic LC-tank has a better phase noise to power ratio, however, for a fixed maximum output swing, both VCOs

have the same phase noise to power ratio, and the dual-resonance oscillator has a lower phase noise. This is the general case for power combining oscillators.

This result assumes that the parallel tank resistance (R_P) remains unchanged in both modes and the quality factor of the tank remains unchanged at a given frequency. However, equation (3.10) indicate that the quality factor of the dual-resonance tank scales at a given frequency if its dominated by quality factor of the inductors. Equation (2.49) is rewritten as:

$$L_{1/f^2}(\Delta\omega) = 10Log\left(\frac{(1+\gamma)k_bT}{{I_{\omega 0}}^2} C\left(\frac{\omega_0}{Q}\right)^3\left(\frac{1}{\Delta\omega}\right)^2\right) \tag{3.20}$$

Equation (3.20) is evaluated for the basic LC-tank VCO and for the dual-resonance VCO constructed by combining two LC-tank VCOs, where each tank consists of a parallel Capacitance (C_U) and inductance (L_U) and their series resistances R_{CS} and R_{LS}, as it was done in sections 3.7 and 3.8 where:

1) Quality factor of capacitors dominate Q_C=1/(ω R_{CS} C_U)
2) Quality factor of inductors dominate Q_L= ω L_U / R_{LS}

LC-tank / Q_C dominant	$10Log\left(\frac{(1+\gamma)k_bT}{{I_{\omega 0}}^2} C_U\left({\omega_0}^2 R_{CS} C_U\right)^3\left(\frac{1}{\Delta\omega}\right)^2\right)$
LC-tank / Q_L dominant	$10Log\left(\frac{(1+\gamma)k_bT}{{I_{\omega 0}}^2} C_U\left(\frac{R_{LS}}{L_U}\right)^3\left(\frac{1}{\Delta\omega}\right)^2\right)$
Dual-resonance / Q_C dominant	$10Log\left(\frac{1}{2}\frac{(1+\gamma)k_bT}{{I_{\omega 0}}^2} C_U\left({\omega_0}^2 R_{CS} C_U\right)^3\left(\frac{1}{\Delta\omega}\right)^2\right)$
Dual-resonance / Q_L dominant	$10Log\left(\frac{1}{2}\frac{(1+\gamma)k_bT}{(Q_R)^3 {I_{\omega 0}}^2} C_U\left(\frac{R_{LS}}{L_U}\right)^3\left(\frac{1}{\Delta\omega}\right)^2\right)$

(3.21)

For the symmetric dual-resonance oscillator, created using two symmetric LC-tank oscillators whose oscillation frequency is ω_{LC}, and resonators quality factor Q_{LC}, the equation in (3.21) simplifies to:

Dual-resonance

Q_C or Q_L dominant

$$10Log\left(\frac{1}{2}\frac{(1+\gamma)k_bT}{{I_{\omega 0}}^2}C_U\left(\frac{1}{(1\pm k)}\frac{\omega_{LC}}{Q_{LC}}\right)^3\left(\frac{1}{\Delta\omega}\right)^2\right) \qquad (3.22)$$

This result indicates that, in the case of a symmetric dual-resonator, regardless of whether the quality factor of the inductor or the capacitor dominates, the dual-resonance phase noise and resonance frequency will be $1/2(1\pm k)^3\cdot$ and $1/\sqrt{(1\pm k)}\cdot$ that of the uncoupled resonator respectively.

In order to test this result, two LC-tank VCOs were constructed: (1) series inductor (L_1), resistance (R_{LS}) in parallel with capacitance (C_1) and (2) series capacitor (C_2), resistance (R_{CS}) in parallel with inductance (C_2). For the first VCO, L_1=400 pH and R_{LS} was set to give an inductor quality factor of 15 at 10GHz. Due to parasitic capacitance, and the impact of Q, the effective resonance frequency shifted to 9.83GHz, and the effective quality factor (Q_L) at resonance was 14.75.

For the second VCO, and in order to match the resonance frequency and quality factor with the first VCO, L_2 was set to $(1+Q_L^2)/\ Q_L^2\ L_1$, and $Q_C=\omega_{RES}\ (1+Q_L^2)\ R_{SL}\ C_1 = (C_1\ /C_T)\ Q_L$=14.3, where C_T is the total load capacitance including the parasitic capacitance. Additionally, the capacitance $C_2 = ((1+ Q_C^2) / Q_C^2)\ C_1$ and the resistance $R_{SC} = ((1+ Q_L^2) / (1+ Q_C^2))\ R_{SL}$.

The two VCOs are combined similar to the circuits presented in Figure **3.20** Figure **3.24** to produce the high and low resonance modes. The simulation is conducted using ideal bias current sources and thermal noise only. The result is presented in Figure **3.27** and Table 6.

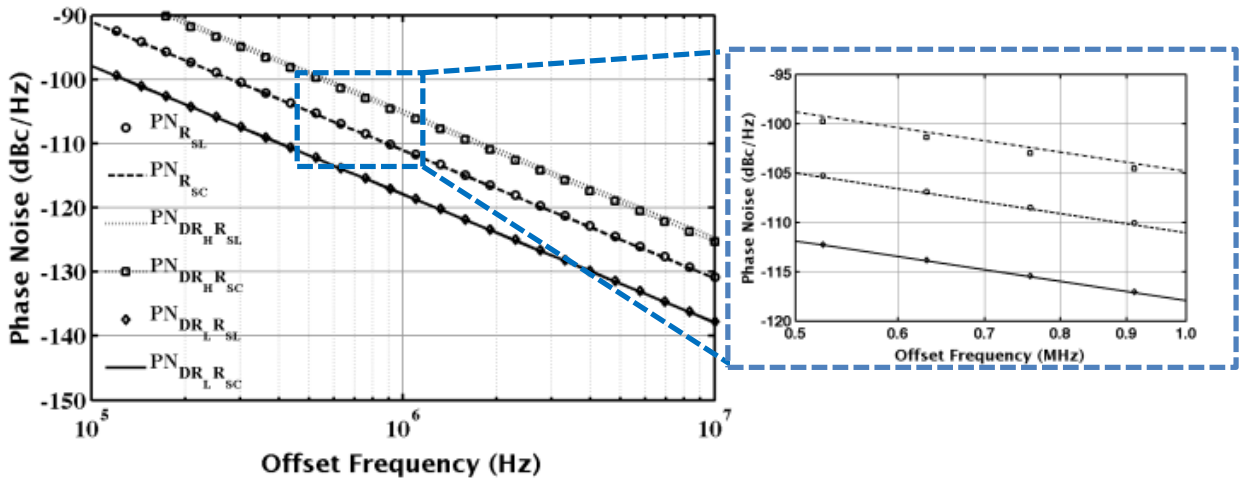

Figure 3.27: *Phase noise comparison of the capacitor quality factor dominated resonator (PN_{RSC}) and the inductance quality factor dominated resonator (PN_{RSL}) in single LC-tank VCO and dual mode resonance in high frequency mode (DR_H) and low frequency mode (DR_L)*

Table 6: *Phase noise evaluated for inductor and capacitor quality factor dominated LC-tank, low and high mode dual-resonance VCOs at 1MHz*

	Tank	Dual Resonance	PN@1MHz dBc/Hz		
			Calculated	Calculated (V_0 from Sim)	Simulated
PN_{RSL}	$(L_1 + R_{SL})//C_1$	None	-112.086	-111.305	-110.839
PN_{RSC}	$L_2//(C_2 + R_{SC})$	None	-112.086	-111.337	-111.001
$PN_{DRH,RSL}$	$(L_1 + R_{SL})//C_1$	Hi-res mode (k=0.3)	-110.449	-105.267	-104.79
$PN_{DRH,RSL}$	$L_2//(C_2 + R_{SC})$	Hi-res mode (k=0.3)	-110.449	-105.686	-105.335
$PN_{DRL,RSL}$	$(L_1 + R_{SL})//C_1$	Lo-res mode (k=0.3)	-118.515	-118.309	-117.808
$PN_{DRL,RSL}$	$L_2//(C_2 + R_{SC})$	Lo-res mode (k=0.3)	-118.515	-118.333	-117.872

The results overall match the prediction that the phase noise will depend on the oscillation mode in a real tank modeled by series resistances, and that the dependence is the same if the quality factor is capacitor dominated or inductor dominated. The main discrepancy is between calculated and simulated results for the high resonance mode, which are matched more accurately by using the output voltage swing from simulation. This is due to lowered output swing that changes $I_{\omega 0}$ and changes the nonlinear G_M from current switching to almost linear operation.

Chapter 4

THE RESONANCE TANK PASSIVES AND PHASE CHANGE SWITCHING

4.1. Introduction

This section introduces the different VCO tuning methods and compares their impact on the tank's quality factor and hence phase noise. Consider a tank comprising a varactor, a switched capacitor array and a fixed inductor, as shown in Figure **4.2**. An expression for the quality factor of a switched capacitor arrays is first derived. This analysis is then employed to compare the impact of alternative tuning methods, including switched inductance, dual-mode resonance and PC switched capacitors.

4.2. The Inductor

Assuming that Q_{TANK} is dominated by the inductor's quality factor (Q_L), the term $Q_{TANK}^3[\omega_0]L$ can be replaced by $Q_L^3[\omega_0]L$. Based on simulation results in a 65 nm CMOS process, the $Q_L^3[\omega_0]L$ term is evaluated for a number of inductor configurations corresponding to oscillators optimized to operate at a range of resonant frequencies. Figure **4.1**(a) depicts the maximum $Q_L^3[\omega_0]L$ for each inductor plotted against the frequency that yields the maximum Q_L. As can be seen in the figure, for a 2 turn inductor which is optimal for use at frequencies below 15 GHz, the $Q_L^3[\omega_0]L$ term drops with frequency while a 1 turn inductor which is optimal for use at frequencies above 15 GHz , the $Q_L^3[\omega_0]L$ increases with frequency. The resulting phase noise dependence on resonant frequency is given by the term $\omega_0 / Q_L^3[\omega_0]L$ is depicted in Figure **4.1** (b). Overall, the phase noise increases with frequency. However, the rate of this increase drops at higher

frequency when single turn inductor configurations are utilized as long as the tank's Q_{TANK} is dominated by the inductor's Q_L.

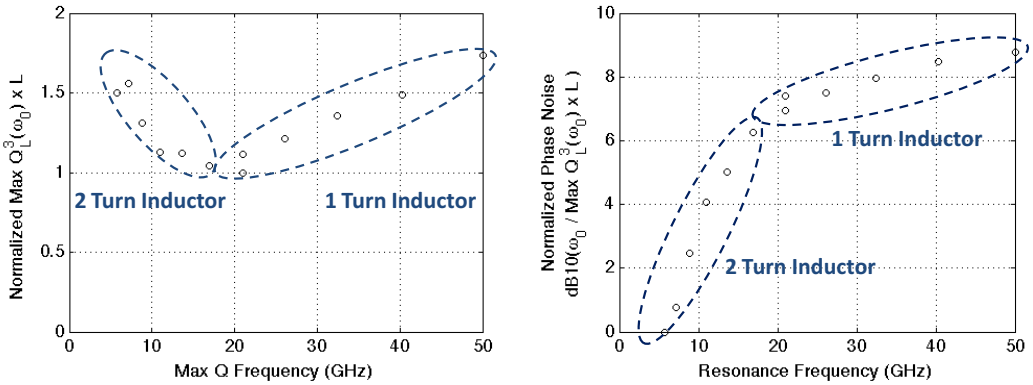

Figure 4.1: (*a*) *Maximum* Q_L^3 $(\omega_0)L$ *for a number of inductor configurations in the 65 nm CMOS process normalized and plotted against the maximum* Q_L *frequency and* (*b*) *The normalized phase noise term* ω_0/Q_L^3 (ω_0) *L plotted against the resonant frequency* (ω_0)

4.3. The Tuned Capacitor

A cross-coupled LC VCO can be tuned by changing the inductance and/or the capacitance. Varactors can be used for continuous tuning, whiles switched inductors and switched capacitors can be used for discrete tuning. Coupled resonators which employ magnetic coupling (using transformers) or electrical coupling (using capacitors) can be used instead, and enable dual resonance modes. By appropriate design, the VCO can be programmed to oscillate in only one of the two modes. One way to switch between the two modes is to change the polarity of the transformer coupling factor (*k*).

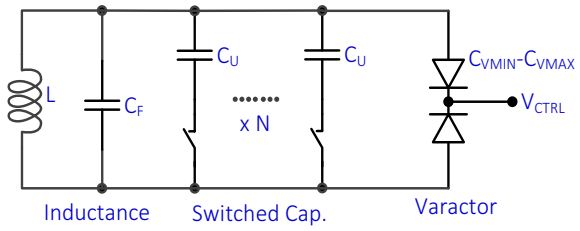

Figure 4.2: *A basic LC tank that consists of a fixed inductor* (*L*)*, a tuning varactor with capacitance ranging from* C_{VMIN} *to* C_{VMAX} *and a switched capacitor array consisting of N identical instances of equal unit capacitance* (C_U)

4.4. Basic LC Tank Design

The LC tank shown in Figure **4.2** uses capacitive tuning only. While the varactor allows for continuous tuning, it suffers from low quality factors. Additionally, the voltage dependence of the C-V characteristic converts amplitude noise into phase noise [25]. The maximum to minimum capacitance ratio of the varactor is fixed and independent of the quality factor. While the varactor cannot be eliminated in most applications, its capacitance should be minimized. If the varactor capacitance is much smaller than the switched capacitor array, the switched capacitor array dominates the quality factor, since the quality factor of two parallel capacitors is:

$$Q_P = \left(\frac{Q_1}{C_1} // \frac{Q_2}{C_2} \right) (C_1 + C_2) \tag{4.1}$$

The operator '//' refers to the parallel combination. To guarantee continuous frequency tuning, the unit capacitance (C_U) has to be smaller than the varactor's tuning capacitance C_{VMAX}-C_{VMIN}. The analysis from this point onwards will only consider the switched capacitor array's quality factor.

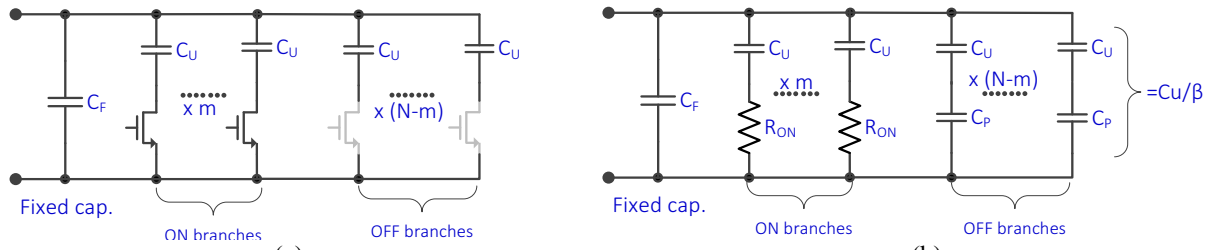

Figure 4.3: (a) *Switched capacitor array with parasitic fixed capacitance* (C_F), *m On branches and N-m Off branches of unit capacitance* (C_U) *and* (*b*) *The equivalent model of the switched capacitor array with CMOS switch parasitic on-resistance* (R_{ON}) *and off-capacitance* (C_P) *considered*

Nanoscale CMOS technologies feature high quality factor capacitors (>100 at mm-wave frequencies) with acceptable density. Such capacitors, switched using MOS switches as depicted in Figure **4.3** (a), can be employed to obtain discrete (switched) tuning. However, the quality factor of such a capacitor array is inversely proportional to the tuning range (*TR*).

In order to understand the tradeoff between tuning range and quality factor, consider the model in Figure **4.3** (b) .The model comprises N unit capacitor (C_U) and CMOS switches, of which m branches are switched on. The MOS switches are modeled by their on-resistance (R_{ON}) in the ON state and by their parasitic capacitances (C_P) in the OFF state, respectively. Qualitatively, in order to obtain a larger tuning range, a large ratio (β) between the maximum capacitance (all CMOS switches on) to the minimum capacitance (all CMOS switches off) is required. To obtain a large β, a wide MOS device is necessary, which is accompanied by a large (C_P). Conversely, choosing a switch with lower widths increases the R_{ON} and degrades the quality factor. The relationship between C_P and R_{ON} for a CMOS device with dimension W/Ln can be expressed as follows:

$$C_P = \frac{C_U}{\beta - 1} = C_{PU} \times W \times Ln \quad , \qquad R_{ON} = \kappa \frac{Ln}{W} = \kappa \frac{(\beta - 1) C_{PU} Ln^2}{C_U} \tag{4.2}$$

where C_{PU} is the unit parasitic capacitance and κ is the on-resistance per square of the CMOS switch. A smaller β is therefore desirable.

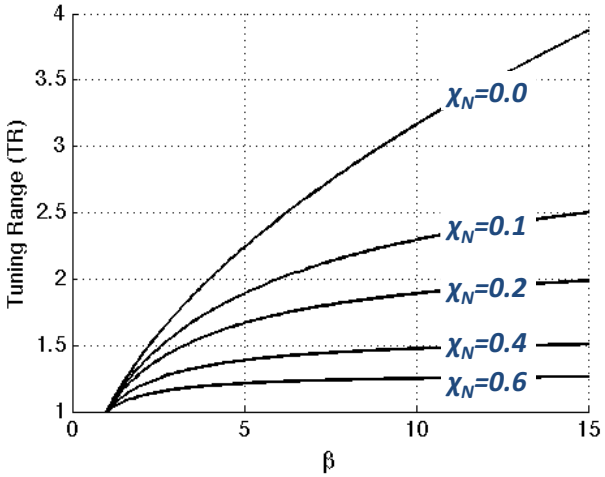

Figure 4.4: *Tuning range as a function of the switched capacitor array's* β (*the ratio of max to min tuning capacitances*) *at a range of* χ_N *values* (*the ratio of the fixed capacitance to the total capacitance*)

In the presence of a fixed capacitance (C_F), a larger β is required to obtain the same tuning range. The fixed capacitance can arise from parasitic capacitance of passive/active devices in the oscillator, parasitic capacitance from the inductor in the tank, varactors, and capacitors switched using "ideal" (e.g., PC) switches. . The tuning range can be expressed in terms of β and C_F as follows:

$$TR = \sqrt{\frac{\beta}{1+\chi_N(\beta-1)}} \quad , \quad \chi_N = \frac{C_F}{NC_U + C_F} \tag{4.3}$$

where χ_N is the ratio of the fixed capacitance to the maximum total capacitance of the tank. This relationship can be better understood by plotting it in Figure **4.4**. The figure indicates that as χ_N (i.e. C_F) increases, a much larger β is required to meet the same tuning range. The figure also indicates that for a given χ_N, a tuning range greater than $1/\sqrt{\chi_N}$ cannot be obtained. Since a smaller β value is desirable, the design can:

a) Use a smaller inductor value to accommodate a larger tuning capacitor.

b) Tightly control the parasitic capacitance.

c) Cancel the parasitic capacitance by introducing negative capacitance[26],[15].

d) Reduce the CMOS switched capacitor array's tuning range by using alternative tuning methods.

4.5. Quality Factor of the CMOS Switched Capacitor Array

A closed form expression for the quality factor of the CMOS switched capacitor array depicted in Figure **4.4** is derived. The switched capacitor array is designed to meet a tuning range (TR), a minimum resonant frequency (ω_{MIN}), and has a fixed to maximum total capacitance ratio (χ_N). The normalized resonant frequency ω_R (defined below) is depends on the number of on-branches (m). The quality factor of the switch capacitor array is given by:

$$Q_{RES} = \underbrace{\left\{\frac{1}{\kappa C_{PU} Len^2}\right\}}_{A}\underbrace{\left\{\frac{1}{\omega_{\min}}\right\}}_{B}\underbrace{\left\{\left(\frac{1-\chi_N TR^2}{(1-\chi_N)}\right)\right\}}_{C}\left\{\frac{1/\omega_R}{TR^2-\omega_R^2}\right\}$$

$$\text{where } \omega_R^2 = \left(\frac{\omega_{RES}}{\omega_{\min}}\right)^2 = \frac{TR^2}{1+\frac{m}{N}\left(TR^2-1\right)} \tag{4.4}$$

Equation (4.4) can be divided into three terms (*A*, *B, C*). Term *A* is a technology dependent and is limited by the minimum available transistor length. Term *B* is inversely proportional to the minimum resonant frequency and is process independent. Technology-dependent fixed parasitic capacitance across the tank causes χ_N to be process dependent; however, if this is ignored, then term *C* also becomes process independent. Term C is plotted in Figure **4.5** against the normalized frequency for several target tuning ranges. As can be seen in Figure **4.5**, the quality factor of the CMOS switched capacitor array can be vastly improved by reducing its tuning range. This tuning range reduction can be achieved by using other tuning methods to perform coarse tuning and using switch capacitor arrays to perform the fine tuning. A number of alternative tuning methods are introduced and discussed in the next sub-section, and their impact on the switched capacitor array's quality factor is discussed in the final sub-section.

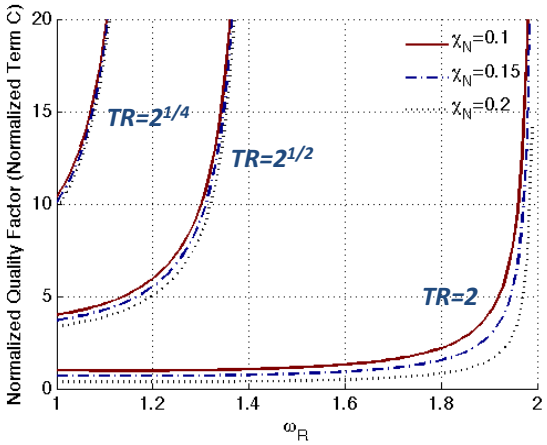

Figure 4.5: *Normalized quality factor as a function of normalized resonant frequency* (ω_R)*, as tuning range* (*TR*) *and fixed to maximum total capacitance ratio* (χ_N) *are varied.*

4.6. Phase Change Switching

Compared to MOS switches, PC switches have much lower capacitance for the same R_{ON}, and therefore, have much higher bandwidth ($\omega_{BW}=1/(R_{ON}C_P)$). Therefore, PC switches are well-suited to switching between different sub-bands, with CMOS switched capacitors used for discrete tuning within each sub-band.

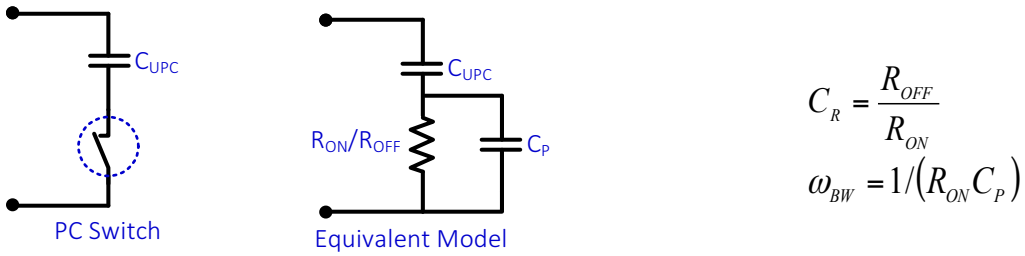

Figure 4.6: *Phase-changed switched capacitor branch and its circuit model.*

A single PC switch is used to switch between two sub-bands, whose total tuning range is TR_0, with no overlap. In each sub-band, CMOS switched capacitive tuning is used to sweep the frequency. Ideally, a PC switched capacitor can switch between an arbitrarily large capacitance C_{UPC} and a small capacitance, which is approximately equal to its parasitic capacitance C_P, while maintaining a high quality factor in both cases. In practice, a real PC switch has a small, but non-zero R_{ON}, and a large, but non-infinite R_{OFF}. The effective capacitance and quality factor of the PC-switched capacitor branch shown in Figure **4.6** is:

$$C_{EFF} = \frac{1+Q_{PC}^2}{1+\beta_{PC}Q_{PC}^2}C_{UPC} \quad , \quad Q_{EFF} = \frac{1}{Q_{PC}}\frac{1+\beta_{PC}Q_{PC}^2}{\beta_{PC}-1}$$
$$\text{where } \beta_{PC} = 1+\frac{C_{UPC}}{C_P} \ , \ Q_{PC} = \begin{cases} \omega/\omega_{BW} & \text{Switch ON} \\ \omega/\omega_{BW} \times C_R & \text{Switch OFF} \end{cases} \tag{4.5}$$

In order to get the maximum quality factor improvement from using the PC switched capacitor, the On/Off Q_{EFF} has to be greater than the minimum CMOS switched capacitor array's quality

factor in the On/Off sub-band. Using this condition, the required Q_{PC}, ω_{BW} and C_R are determined.

In order to determine the minimum CMOS switched capacitor array's quality factor in each sub-band, the tuning ranges ($TR_{L,H}$) and fixed capacitance ratios ($\chi_{NL,H}$) in both sub-bands has to be determined. Assuming the original CMOS switched capacitor array was used to switch between two capacitances $\underline{C_{MAX}} = NC_U$ and $C_{MIN}=C_{MAX}/\beta$, the modified CMOS switched capacitor array's C'_{MAX} and C'_{MIN} and the corresponding C_{PU} are:

$$\begin{aligned} C'_{MIN} &= C_{MIN} - C_P \\ C'_{MAX} &= \frac{C_{MAX} + C_{MIN}}{2} - C_P \\ C_{UPC} &= \frac{C_{MAX} - C_{MIN}}{2} + C_P \end{aligned} \tag{4.6}$$

The Corresponding tuning range in lower sub-band is $TR_L = \sqrt{2TR_0^2/(1+TR_0^2)}$, and in the upper sub-band is $TR_H = \sqrt{(1+TR_0^2)/2}$ .The corresponding $\chi_{NL,H}$ for a given original χ_{N0} are:

$$\begin{aligned} \chi_{NL} &= \frac{1+2\left(1-\frac{C_P}{C_{MIN}}\right)\left(\frac{1-TR_0^2\chi_{N0}}{1+TR_0^2}\right)}{TR^2} \\ \chi_{NH} &= \frac{\frac{C_P}{C_{MIN}} + TR_0^2\chi_{N0}\left(1-\frac{C_P}{C_{MIN}}\right)}{TR^2} \end{aligned} \tag{4.7}$$

4.7. Alternative Tuning Methods' Impact on CMOS Switched Capacitive Tuning

Since different alternative tuning methods result in different tuning ranges in the resulting sub-bands and different χ_N values, their impact on the modified CMOS switched capacitor circuit's quality factor varies. Figure **4.7** shows the normalize quality factors before and after applying the alternative tuning method for the three tuning methods.

Table 7: *Impact of alternative tuning methods on CMOS switched capacitive tuning parameters*

Original Term	TR_0	χ_{N0}	Effective L
Dual Resonance	$TR_{H,L} = \sqrt{TR_0}$	$\sqrt{TR_0} \times \chi_{N0}$	L (L(1+k), L(1-k))
Inductance Increase	$TR_{H,L} = \sqrt{TR_0}$	$TR_0 \times \chi_{N0}$	L , $2L$
Inductance decrease	$TR_{H,L} = \sqrt{TR_0}$	χ_{N0}	L, $L/2$
PC switching	$TR_L = \sqrt{2TR_0^2/(1+TR_0^2)}$ $TR_H = \sqrt{(1+TR_0^2)/2}$	See Eq. (4.7)	L

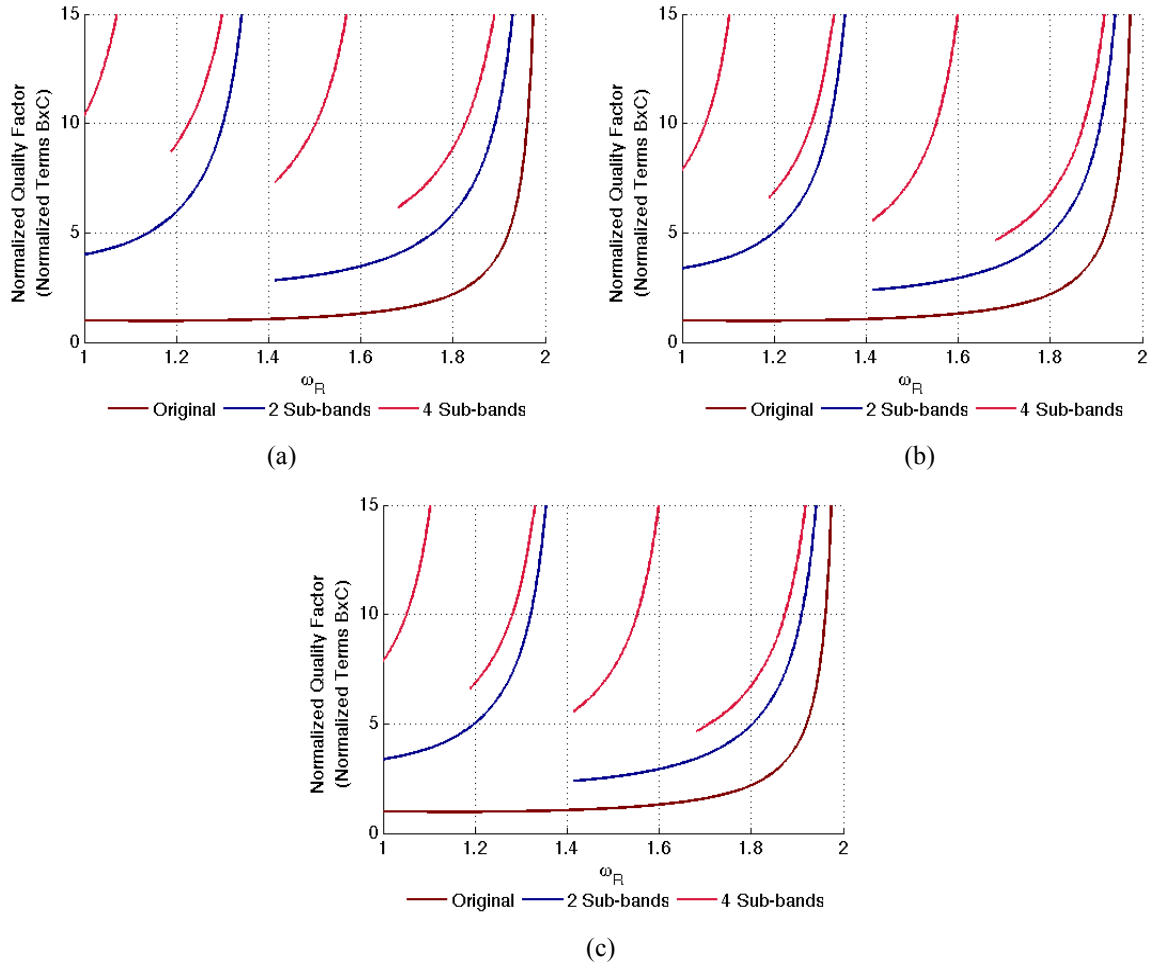

Figure 4.7: *Normalized quality factor* (*Terms B·C*) *demonstrating Q improvement from* (*a*) *TR reduction* (χ_N=*0.1*) , (*b*) *TR reduction with* χ_N *scaled by a factor of* $(TR_{ORIGINAL}/TR_{FINAL})^2$ (χ_N:*0.1*→ *0.2*) *and* (*c*) *TR reduction associate with P-C switch* (χ_N=*0.1* → [*0.2,0.5*] *for* [*high, low*] *sub-bands respectively*)

It is worth noting that equation (4.4**)** does not consider the off quality factor of the switched capacitor, dominated by the quality factor of the capacitors used. Consequently, the plotted

quality factors in Figure 4.7 approach infinity as ω_R approaches TR. In a more accurate model, it should approach the quality factor of a single unit capacitance, a value that is inversely proportional to frequency.

To compare the improvement in CMOS switched capacitor quality factor based on the different alternative tuning methods, Figure **4.8** shows the quality factor improvement (2 sub-bands Q/Original Q) evaluated at the minimum quality factor frequency in the two resulting sub-bands. As the figure shows, if the switch used to switch inductors does not impact its quality factor, one should use switching inductance and dual mode resonance as the most coarse tuning method, followed by switching inductance to a larger value and finally P-C capacitor switching.

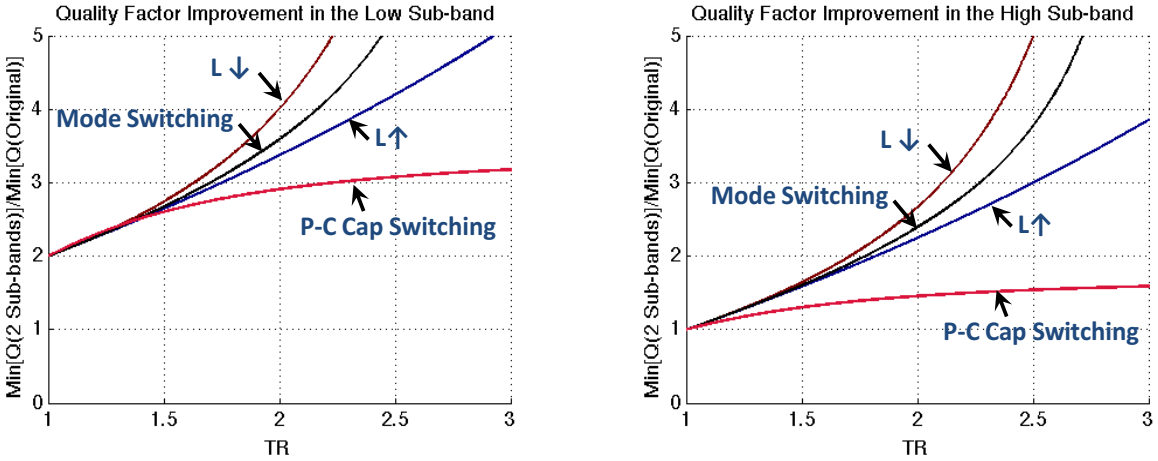

Figure 4.8: *Improvement in CMOS switched capacitor tank's minimum quality factor as a function of tuning range* (χ_{NORIG}= *0.1*)

Chapter 5
CIRCUIT DESIGN AND SIMULATIONS

5.1. Introduction

This chapter presents the two proposed QVCOs with device and bias current sizes, along with a set of phase noise simulations covering the full tuning range for each circuit. The simulations study the impact of a number of layout parasitics by adding significant parasitics gradually and observing their impact on resonance frequency (tuning range) and phase noise.

5.2. Active QVCO Circuit and Simulations

5.2.1. Circuit Overview

The active QVCO consists of two dual-resonance circuits coupled as shown in Figure **5.1**. The device sizes have been specified on the schematic. Mode switching is achieved as discussed earlier by controlling the sign of the G_M transconductance. This is achieved by the two parallel differential G_M cells which are controlled by the *Sel'* digital control signal.

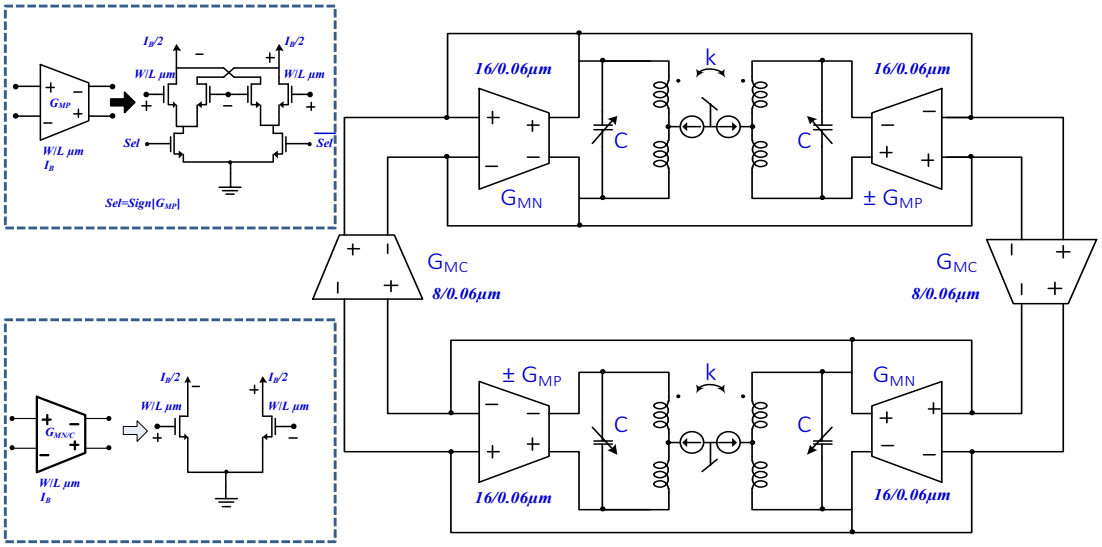

Figure 5.1: *Active quadrature voltage controlled oscillator architectures with dual resonance mode coupled resonator tanks*

The bias currents are generated and controlled by a PMOS bias circuit that was laid out as a single unit to ensure current ratio matching despite process mismatches. PMOS devices were used due to their lower flicker noise, in order to minimize the overall phase noise of the circuit. The bias circuit topology and current ratios are depicted in Figure **5.2**.

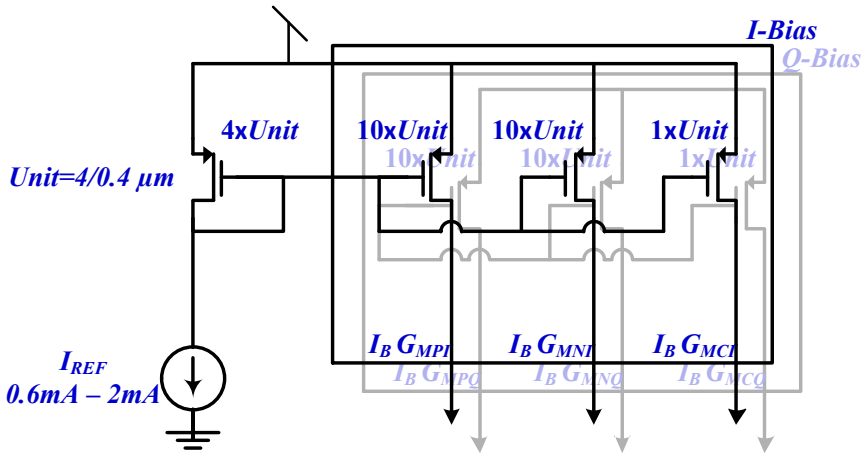

Figure 5.2: *Circuit schematic of the PMOS current mirror used for the biasing of the VCO*

5.2.2. Transformer Design

Both dual-resonance cores utilize the same transformer architecture. The layout of this transformer is shown in Figure **5.3**. It consists of two center tapped inductors which are arranged in a manner to allow for access to both transformers from the same side. The transformer is 310µm x 210µm in size. This is less than a 1/3rd larger than the area of a single such inductor. A single turn inductor was used based on the simulation on the Q^3L parameter at this frequency. The inductance, coupling and differential quality factors are shown in Figure **5.17**.

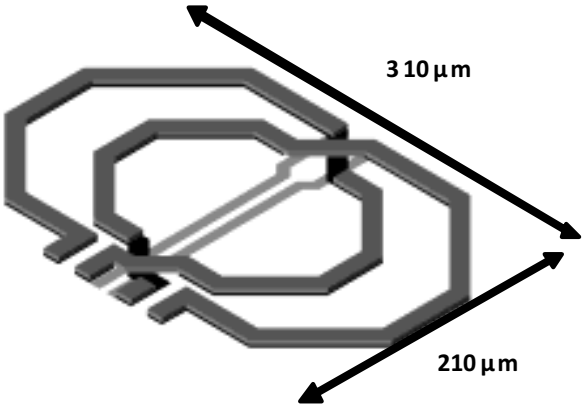

Figure 5.3: *Mutual inductor layout and dimensions*

The mutual inductor is a complex structure which can be best captured by the lumped element model such as that shown in Figure **5.4**. The model elements represent actual circuit elements. C_{SUB} and R_{SUB} represent the resistance and capacitance due to the substrate, while C_{ox} represents the oxide capacitance. C_M represents the capacitance between the two inductors in the transformer, while C represents the self capacitance of each inductor. L, and R and k represent the inductance, resistance and coupling between the two coils.

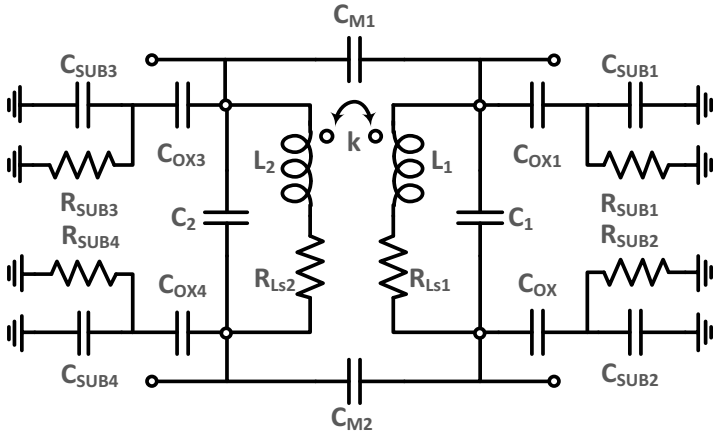

Figure 5.4: *Lumped element model of integrated circuit mutual inductor*

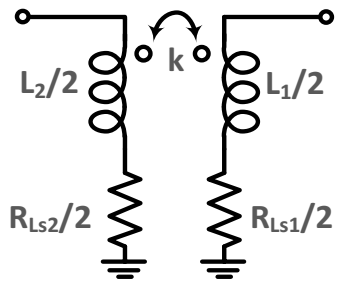

Figure 5.5: *Half circuit of reduced center-tapped mutual inductor model*

While it is advantageous to construct such model, one can attempt to use data collected differentially to fit parameters into the simpler half circuit model in Figure **5.5**.

The inductor layout was created using Cadence LayoutXL, and Integrand Software EMX EM simulator was used to extract the S-parameters from the layout. The resulting S-parameters are used to create a 4-port element whose voltage/current equations are defined by equations interpolated from the EM simulation. The model is simulated using Cadence SpectreRF S-parameters simulations to obtain a set of Z/Y-parameters. This can be done using either a single-ended driven or a differential driven test bench as shown in Figure **5.6**.

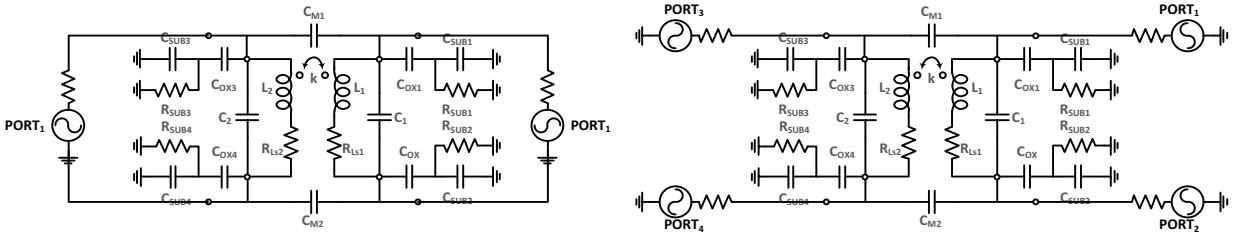

(a) (b)

Figure 5.6: (*a*) *Single-ended and* (*b*) *differentially driven mutual inductor*

The circuit parameters *L*, *R* and *k* can be readily obtained from the 2-port Z-parameter matrix derived from the S-parameter matrix the simulation produces according to equation:

$$\begin{pmatrix} R_1 + sL_1 & sk\sqrt{L_1L_2} \\ sk\sqrt{L_1L_2} & R_2 + sL_2 \end{pmatrix} = \begin{pmatrix} Z_{11} & Z_{12} \\ Z_{21} & Z_{22} \end{pmatrix} \tag{5.1}$$

On the other hand, the differentially driven model requires further data processing. This can be done by considering the Y-parameter model shown Figure **5.7** (a), which can be simplified further in Figure **5.7** (b) and (c) which assumes symmetry along the dotted line in Figure **5.7** (c).

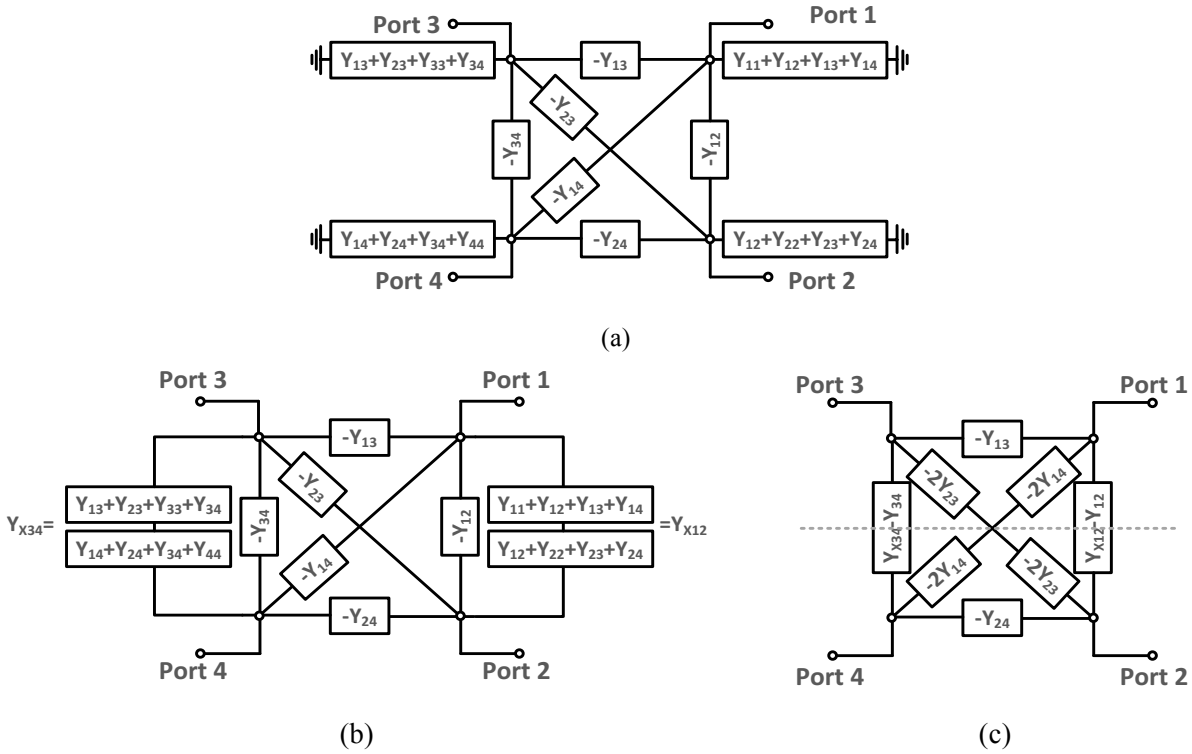

Figure 5.7: (a) *Y-parameter representation of the 4-port mutual inductor and its reduction to* (*b*) *then to* (*c*)

Similar to equation (5.1), the circuit parameters L, R and k can be readily obtained from the 4-port Y-parameter matrix derived from the S-parameter matrix the simulation produces according to equations (5.2) and (5.3):

$$\begin{pmatrix} R_1 + sL_1 & sk\sqrt{L_1L_2} \\ sk\sqrt{L_1L_2} & R_2 + sL_2 \end{pmatrix} = 2\begin{pmatrix} 2(Y_{X12} - Y_{12}) & (-Y_{13} - Y_{24} + Y_{14} + Y_{23})/2 \\ (-Y_{13} - Y_{24} + Y_{14} + Y_{23})/2 & 2(Y_{X34} - Y_{34}) \end{pmatrix}^{-1} \tag{5.2}$$

$$\begin{aligned} Y_{X12} &= \frac{(Y_{11} + Y_{12} + Y_{13} + Y_{14})(Y_{12} + Y_{22} + Y_{23} + Y_{24})}{(Y_{11} + Y_{12} + Y_{13} + Y_{14}) + (Y_{12} + Y_{22} + Y_{23} + Y_{24})} \\ Y_{X34} &= \frac{(Y_{13} + Y_{23} + Y_{33} + Y_{34})(Y_{14} + Y_{24} + Y_{34} + Y_{44})}{(Y_{13} + Y_{23} + Y_{33} + Y_{34}) + (Y_{14} + Y_{24} + Y_{34} + Y_{44})} \end{aligned} \tag{5.3}$$

The derived inductance, coupling factor and quality factors derived from the s-parameter simulations according to the single-ended and differential equations are presented in Figure **5.8**. The inductance is nominally 400 pH, and the coupling factor is nominally 0.26.

The differential quality factor is higher than the single-ended quality factor at frequencies above 5GHz. The trend is expected due to the smaller impact of substrate resistance on the differential quality factor, which becomes significant at higher frequencies. However, the values predicted by the differential model for quality factor appears way too optimistic. The single-ended extracted values are verified in the following sections.

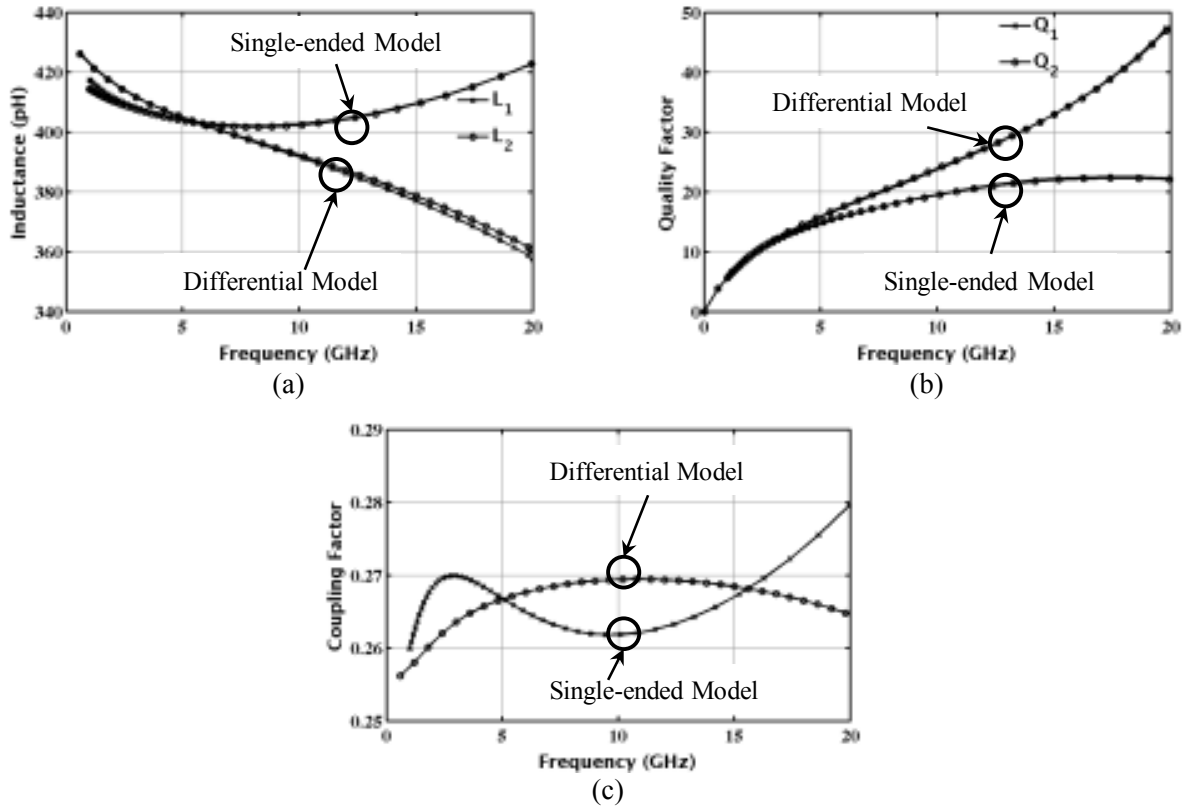

Figure 5.8: *Mutual inductor* (*a*) *inductance,* (*b) coupling factor and* (*c*) *differential quality factor*

5.2.3. Switch Capacitor Tuning Circuit

The frequency tuning is performed using the switched capacitor circuit depicted in Figure **5.9**. The circuit parameters where chosen according to the design analysis presented in Chapter 4.5. The circuit has 6-bits control allowing for 64 frequencies steps of ~7fF each.

The circuit is simulated using Cadence SpectreRF S-parameter simulation. Similar to the mutual inductance, the circuit can be simulated using a single-ended or a differential simulation as shown in Figure **5.10**.

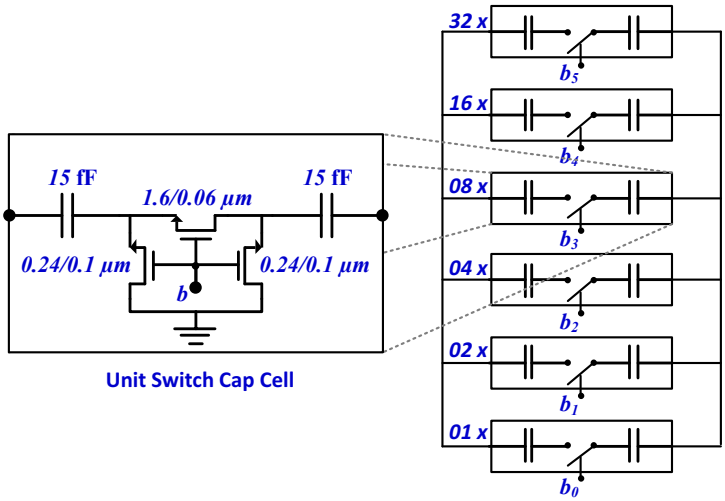

Figure 5.9: *Circuit schematics of the switched capacitor array showing devices sizes and approximate unit capacitance.*

(a) (b)

Figure 5.10: (*a*) *Single-ended and* (*b*) *differentially driven capacitor*

For the single-ended simulation, the capacitance is obtained by taking the $Z_{11}=R+(sC)^{-1}$. The capacitance is therefore the -1/(ω Im[Z_{11}]), and the quality factor -Im[Z_{11}]/(Re[Z_{11}]).

$$C = \frac{-1}{\omega \mathrm{Im}[Z_{11}]} C = -\frac{\mathrm{Im}[Z_{11}]}{\mathrm{Re}[Z_{11}]} \tag{5.4}$$

For the differential simulation, the differential Y_D is obtained as:

$$Y_D = \frac{Y_{11}Y_{22} - Y_{12}Y_{21}}{Y_{11} + Y_{12} + Y_{21} + Y_{22}} \tag{5.5}$$

The capacitance and resistance can be obtained from Y_D, by using $Z_{11}=1/Y_D$ and applying it to equation (5.4). The switched capacitor circuit was designed and laid out. Mentor Graphics Calibre PEX RC extraction tool was used to obtain the full capacitance and parasitic trace resistance of the full switch capacitor array. The RC extracted schematics were simulated in order to obtain capacitance and quality factor of the full capacitor array as a function of frequency for different control codes. The results of the simulation are depicted in Figure **5.11**.

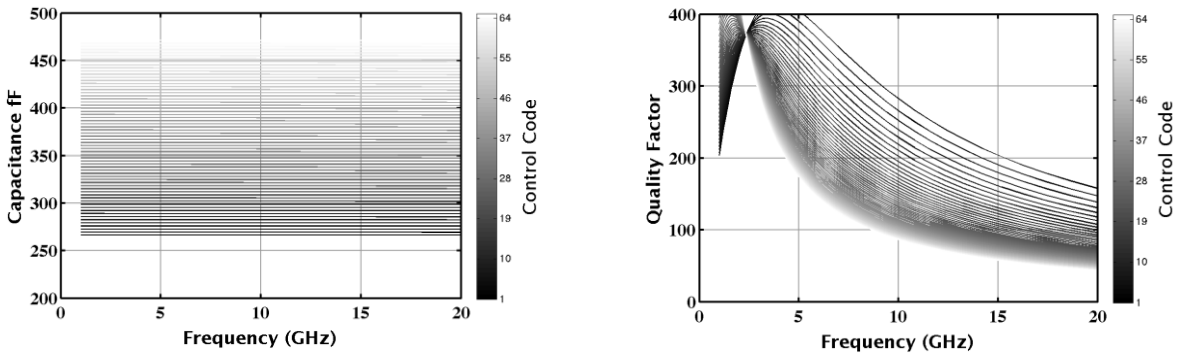

(a) (b)

Figure 5.11: *Switched capacitor array's* (*a*) *capacitance and* (*b*) *quality factor across the tuning range for a layout based simulations*

The minimum capacitance from the switch capacitor array is 266fF and the maximum capacitance is 471fF. The quality factor remains above 40 up to 20 GHz. For each capacitance value, the quality factor drops with frequency as expected. However, the significant point to observe is the quality factor of the

capacitor at the resonance frequency. This requires assuming a fixed value for the inductor (as well as additional fixed capacitance from other circuit parasitics) and calculating the resonance frequency for each value of the capacitance. For each calculated resonance frequency, the quality factor of that particular switch capacitor array arrangement is evaluated at resonance. The simulation was performed assuming a fixed capacitance (C_F=100fF) and an inductance (L=400pH). Both values reflect post layout estimates. The simulation results are depicted in Figure **5.17**. The results match theory discussed in Chapter 4.5.

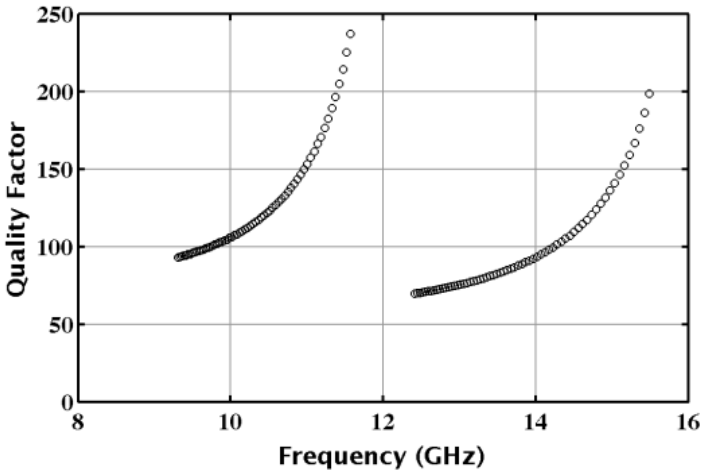

Figure 5.12: *Passive quadrature voltage controlled oscillator architectures with dual resonance mode coupled resonator tanks*

5.2.4. Complete Dual-Resonance Tank Simulation

The quality factor of the dual-resonance is obtained using the three definitions of quality factor as a mean to validate the theory, and evaluate the design. The three definitions are:

(a) Real and imaginary parts of the impedance:

The ratio of the imaginary part of the impedance to the real part of the impedance defines the quality factor of the impedance at frequencies below its self-resonance.

$$Q = \frac{\mathrm{Im}[Z]}{\mathrm{Re}[Z]} \tag{5.6}$$

This definition is the one used to obtain the inductor and capacitor array's quality factors. Given the discussion on quality factor in Chapter 3.5, the quality factor, at resonance, of the dual-resonance tank when tuned in a symmetric fashion is given by:

$$Q_{\mathrm{ImRe}} = Q_C \,//\, Q_L(1 \pm k) \tag{5.7}$$

The effective Q_L is enhanced by the factor (1+k) at the low resonance mode, and degrades by the factor (1-k) at the high resonance mode.

(b) The phase of the impedance at resonance:

The quality factor at resonance is obtained using the phase definition of quality factor:

$$Q_{\Phi} = \frac{\omega_0}{2} \frac{d\Phi}{d\omega}\bigg|_{\omega_0} \tag{5.8}$$

This simulation was performed using Cadence Spectre AC simulation. The test bench is depicted in Figure **5.13**. The circuit is driven differentially using i_{AC+} and i_{AC-} of equal magnitude of 0.5 and opposing phases. The differential voltage v_{i+}-v_{i-} is obtained, and Z_{IN}= (v_{i+}-v_{i-})/1. The resonance frequencies, phase, and phase derivate at resonance are obtained from Z_{IN}.

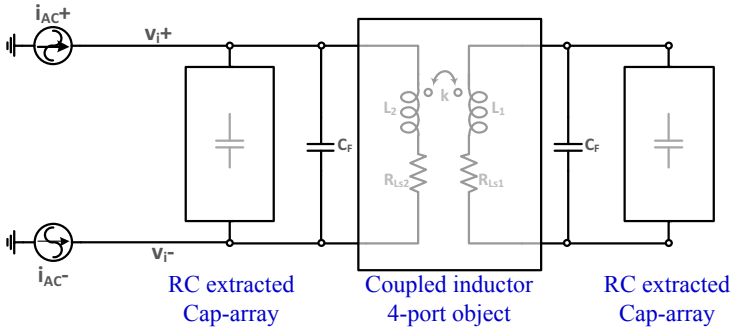

Figure 5.13: (*a*) *Single-ended and* (*b*) *differentially driven capacitor*

(c) The bandwidth of the impedance at resonance:

Using the same phase test bench, the pass-band bandwidth at resonance of Z_{IN} is obtained, and the quality factor is derived from that as the ratio of the resonance frequency to the bandwidth.

$$Q_{B3} = \frac{\omega_0}{\omega_{3dB}} \tag{5.9}$$

The three previous definitions of quality factor are evaluated and plotted against resonance frequency for the complete dual-resonance tank. The results are depicted in Figure **5.14**. The three methods agree with small discrepancies. The discrepancies increase at higher frequency since the single-ended inductor quality factor was used in the derivation. Q_{Φ} requires a large number of frequency samples in order to correctly calculate the derivatives at resonance. A reasonable 300 frequency samples were selected as a reasonable accuracy vs. simulation time.

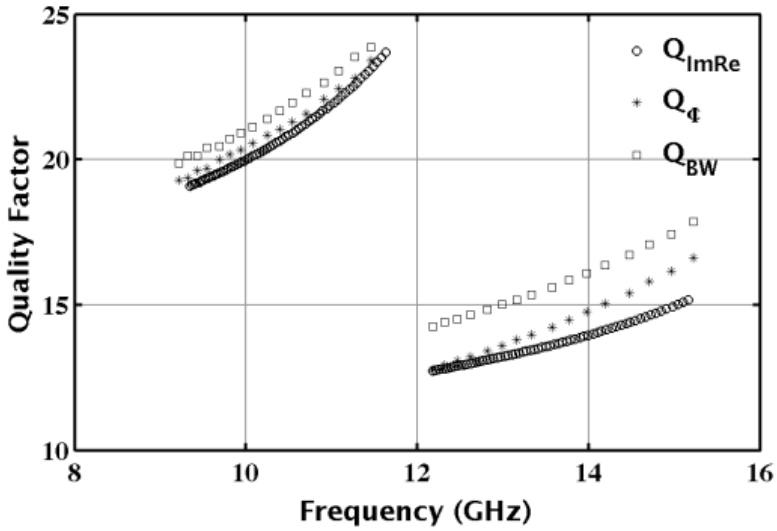

Figure 5.14: *Overall Tank Quality factor at resonance assuming a 100fF additional fixed capacitance*

5.2.5. Startup-Condition

The implications of the quality factor plots presented in Figure **5.14**, and according to theory presented in Chapters 2 and 3 on start-up, the required G_M for startup in the upper band for the

symmetric resonator is almost 1.5x that in the lower resonance mode. Assuming G_M to be proportional to $\sqrt{I_B}$, the bias current requirements for the higher oscillation mode are on the order of 2.25x that in the lower oscillation mode. This was observed in simulations and measurement as will be presented in Chapter 6.

5.2.1. Phase noise and phase error

The phase noise of the actively coupled dual-resonance QVCO circuit can be readily found by applying the quadrature theory presented in Section 2.6 to the equivalent 2nd order simplification circuit presented in Section 3.3. This statement can be verified by performing a number of circuit simulations similar to those performed in Chapters 2 and 3 on the dual resonance circuit presented in Figure **5.1** and the its equivalent 2nd order counterpart shown in Figure **5.15**.

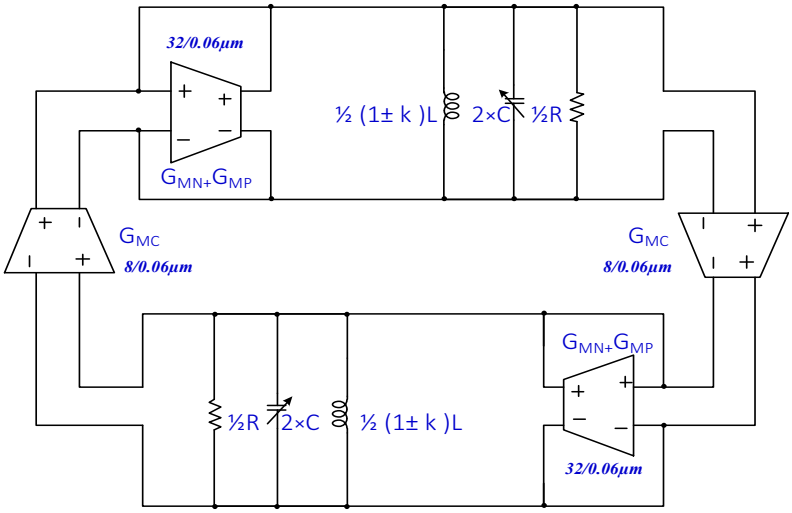

Figure 5.15: *Active quadrature voltage controlled oscillator 2nd order equivalent circuit*

To allow for G_{MC} sweeps the circuit is simulated using the Verilog-A models for G_M that were presented in Section 2.6. A theoretical phase expression is derived by extending equation (2.60), by observing that for the dual resonance quadrature circuit: 1) in the ISF expression n=4, 2)

twice as many noise source are presented as in the LC-tank quadrature circuit and 3) the coupling strength factor k=$I_{GMC}/(I_{GMN}+I_{GMP})$ for the case Ψ=90°, or more generally:

$$k = \frac{\frac{I_{G_{MC}}}{I_{G_{MN}}+I_{G_{MP}}}\left|\sin(\Psi)\right|}{1+\frac{I_{G_{MC}}}{I_{G_{MN}}+I_{G_{MP}}}\left|\cos(\Psi)\right|} \tag{5.10}$$

The phase noise expression is therefore:

$$L_{1/f^2}(\Delta\omega) = 10Log\left(\frac{\left(1+k^2+\gamma\left(1+\frac{I_{G_{MC}}}{I_{G_{MN}}+I_{G_{MP}}}k^2\right)\right)\left(\frac{4k_bT}{R_P}\right)}{16(Q)^2 {I_{\omega 0}}^2}\left(\frac{f_0}{\Delta f}\right)^2\right) \tag{5.11}$$

The theoretical expression in (5.11) is plotted against the simulated phase noise from the dual resonance AQVCO and its equivalent 2nd order QVCO in Figure **5.16**. The results simulations diverge at higher coupling strength values mainly due to the lower G_M/I_{BIAS} ratio used for these simulations. The results show that, if the CMOS devices act as switching transistors, the second order simplification of the dual-resonance actively coupled QVCO is a very good approximation of the original circuit.

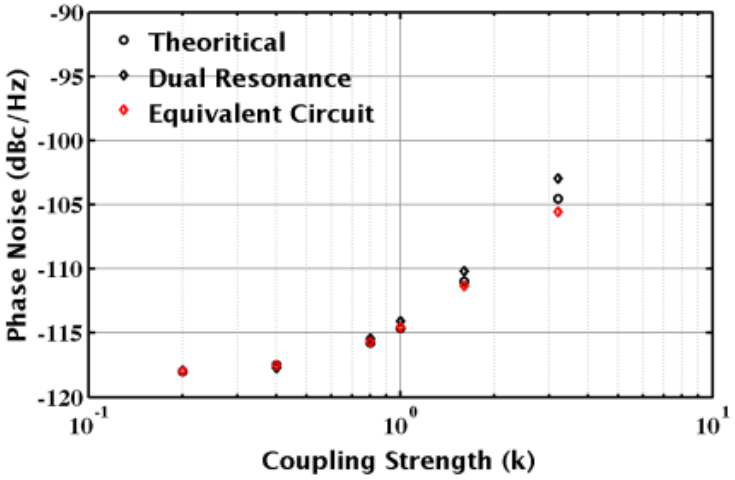

Figure 5.16: *Phase noise sweep versus k=I_Q/I_I , for dual-resonance QVCO, Equivalent 2nd order QVCO and the*

theoretical expression for phase noise with circuits simulated using Verilog-A G_M as described by Figure **2.29**

Furthermore, the phase error due to mismatches between the two coupled cores or the coupling traces, of the dual resonance AQVCO, is given by:

$$\Delta\varphi = \frac{|\sin(\Psi)|}{k+|\cos(\Psi)|}\frac{\Delta I}{2I} - \frac{|\sin(\Psi)|}{k+|\cos(\Psi)|}\frac{\Delta I_{GMC}}{2I_{GMC}} - \frac{1+(k)^2+2k|\cos(\Psi)|}{k(k+|\cos(\Psi)|)}Q\frac{\Delta\omega}{\omega_0} + \frac{(1+k|\cos(\Psi)|)|\sin(\Psi)|}{k+|\cos(\Psi)|}\frac{\Delta R}{R} + \frac{\Delta\Psi}{2} \quad \text{where } k = \frac{I_{G_{MC}}}{I_{G_{MN}}+I_{G_{MP}}} \tag{5.12}$$

where ΔI is the difference between the sum of the bias currents (I_{GMN}+I_{GMP}) of the two oscillator cores, ΔI_{GMC} is the difference between the tail bias currents of the two coupling stages between the oscillators, and Q is the quality factor of the LC-tank, $\Delta\omega$ is the difference in the oscillation frequency of the two dual-resonance cores, ΔR is the difference in the parallel resistance of the two equivalent LC-tanks and $\Delta\Psi$ is the difference between the extra phase delay in the quadrature path between the two cores. For a $\Psi=90^o$ this simplifies to:

$$\Delta\varphi = k^{-1}\frac{\Delta I}{2I} - k^{-1}\frac{\Delta I_{G_{MC}}}{2I_{G_{MC}}} - \left(1+k^{-2}\right)Q\frac{\Delta\omega}{\omega_0} + k^{-1}\frac{\Delta R}{R} + \frac{\Delta\Psi}{2} \tag{5.13}$$

5.3. Passive QVCO Circuit and Simulations

5.3.1. Circuit Overview

The passive QVCO consists of two dual-resonance circuits coupled as shown in Figure **5.17**. The device sizes have been specified on the schematic. Similar to the active QVCO architecture, mode switching is achieved by controlling the sign of the G_M transconductance. This is achieved, by the two parallel differential G_M cells which are controlled by the *Sel'* digital control signal.

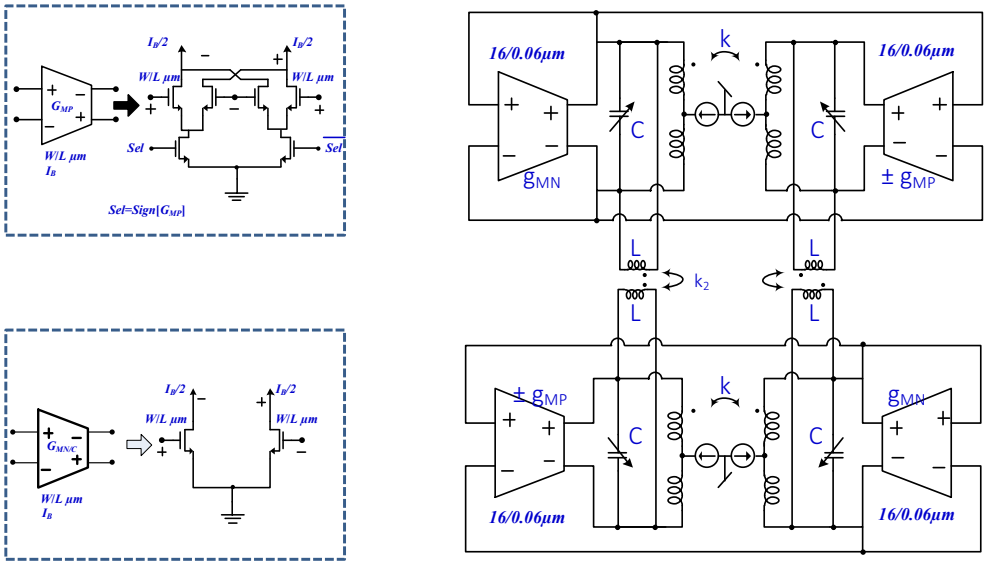

Figure 5.17: *Passive quadrature voltage controlled oscillator architectures with dual resonance mode coupled resonator tanks*

In order to maximize the layout reuse between the two designs, the same G_M stages as the active quadrature architecture were used with slightly modified layouts. Moreover, the bias current circuit was also the same as the one used in the active QVCO, however, since there is no use for the bias current allotted to the quadrature coupling cell in the active QVCO, this bias current was rerouted to the G_{MN} cells as shown in Figure **5.18**.

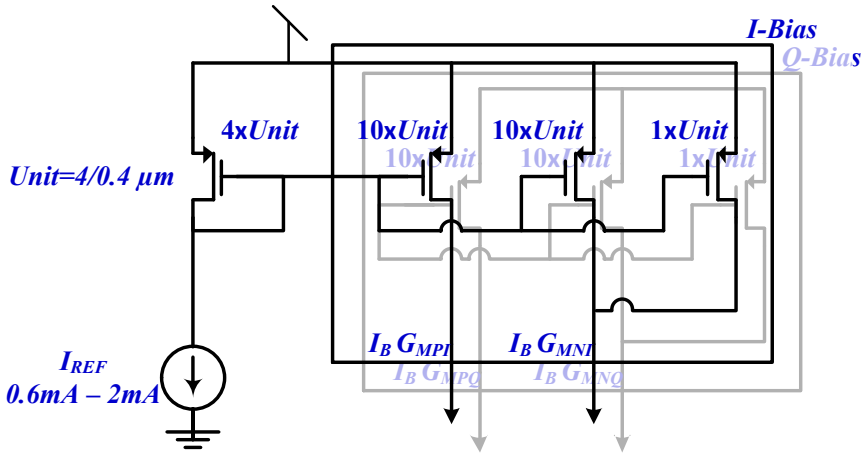

Figure 5.18: *Circuit schematic of the PMOS current mirror used for the biasing of the VCO*

5.3.2. The four coupled resonators network

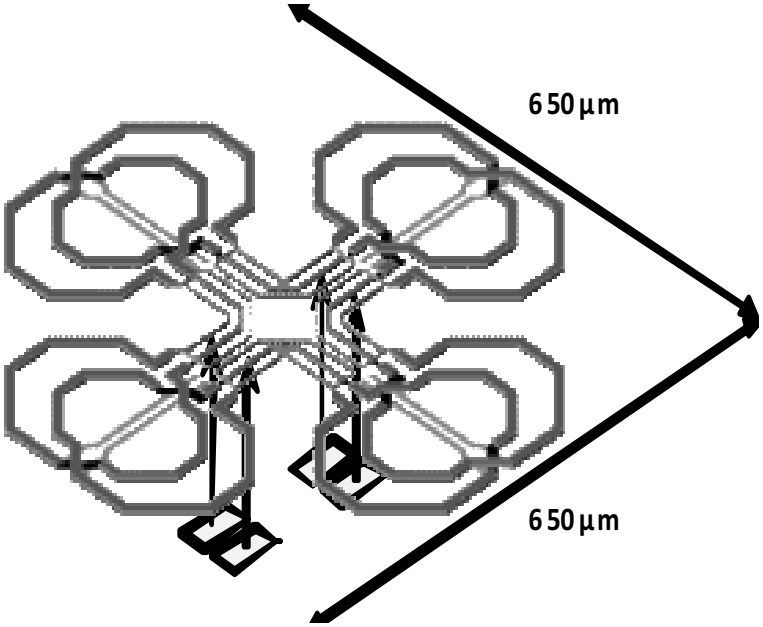

Figure 5.19: *Layout and dimensions of the four coupled resonators with capacitance placement indicated by arrows*

Due to the presence of 4 coupled inductors, and in order to separate the terms from each other, each coupled inductor is implemented separately and isolated and resembles the same architecture as presented for the active QVCO in Figure **5.3**. The capacitor and inductor values presented previously for the active design still holds.

In order to maintain a small quadrature phase error, the combination of the coupled inductors is placed in a symmetric cross shape to equalize the parasitic inductances and capacitances between adjacent blocks. In order to avoid additional parasitic capacitance, the tuning capacitors are routed along the traces connecting the 4 mutual inductors as indicated in Figure **5.19**.

5.3.3. Startup-Condition

The four coupled resonators maintain approximately the same quality factor that was presented previously for the active design since each uncoupled resonator is loaded by two inductors in

parallel with one capacitor. However, since total inductance is halved at each un-coupled resonator, the parallel resistance is also halved.

The reduction of the parallel resistance indicates that a much higher $2 \cdot G_M$ is required, almost 4· the current is required in order to obtain startup. However, due to the fact that the quadrature inductors have to operate in two different modes (one is odd and one is even) always, the impact of their presence on the overall quality factor is countering that of the dual-resonance and it improves the quality factor of the upper band while reducing it in the lower band. This in turn makes the current bias requirements in the two bands more comparable and reduces the 4x current requirement. This general trend was also observed in simulations and in lab measurements.

In order to verify this, the passive network corresponding to the PQVCO shown in Figure **5.20** is considered where k_2 is replaced by αk. Since the PQVCO doesn't suffer from frequency shift from quadrature that takes place in AQVCO, the resonance frequency, quality factors and startup-condition can all be determined based on the passive network alone.

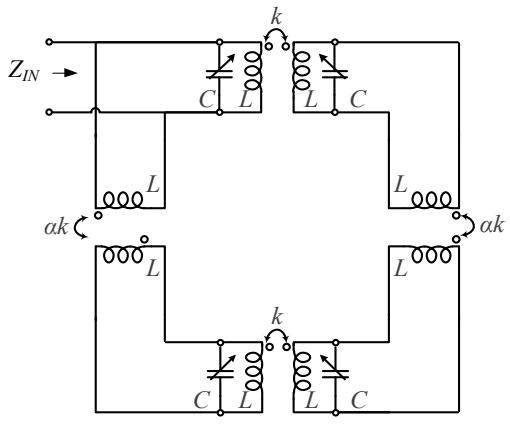

Figure 5.20: *Passive network corresponding to the passive quadrature voltage controlled oscillator*

The passive network is studied by observing the input impedance marked (Z_{IN}) in Figure **5.20**. The input impedance is given by

$$Z_{IN}(s)=\frac{sL\omega_0^{\,2}\,(2(1-k^2)s^2\,(1-\alpha k^2)+(2-(1+\alpha)k^2)\omega_0^{\,2})}{4(1-k^2)s^4\,(1-\alpha k^2)+4s^2\,(2-(1+\alpha)k^2)\omega_0^{\,2}+(4-(1+\alpha)k^2)\omega_0^{\,4}} \tag{5.14}$$

The input impedance has two resonance frequencies given by

$$\omega_{H,L}^{\,2}=\frac{2-k((1+\alpha)k\pm\sqrt{1+\alpha(1-4k^2+(1+\alpha)k^4)})}{2(1-k^2)(1-\alpha k^2)}\omega_0^{\,2} \tag{5.15}$$

where $\omega_0=\sqrt{2}/\sqrt{LC}$. Under the special condition that $\alpha=k_2/k_1$, the resonance frequency expression simplifies to

$$\omega_{H,L}^{\,2}=\frac{1\pm k/\sqrt{2}}{1-k^2}\omega_0^{\,2} \tag{5.16}$$

The expression in (5.15) can be visualized by plotting the ratio of the high to low resonance frequencies for multiple coupling strength ratios (α) as a function of the coupling strength of the dual resonance core (k) as shown in Figure **5.26**. For the sake of comparison, the tuning range of the AQVCO is also shown in Figure **5.26**. As the figure shows, the tuning range of the PQVCO is in general smaller than that of the AQVCO, and it approaches that of the AQVCO for large values of α, as k_2 approaches 1.

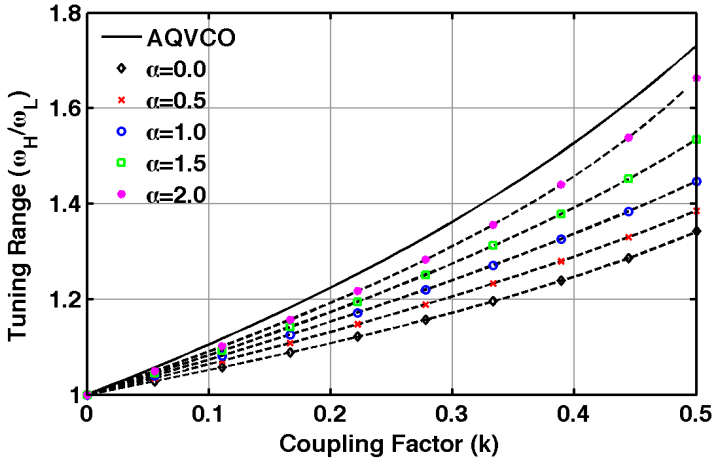

Figure 5.21: *Tuning range of the PQVCO passive network given by ω_H/ω_L versus the coupling factor (k) for multiple values of α compared to that of the AQVCO*

Furthermore, in order to obtain effective quality factor of the two poles, the denominator $D(s)$ of the system $Z_{IN}(s)=N(s)/D(s)$ can be fitted into the following system model

$$D(s) = \left(s^2 + \frac{\omega_L}{Q_L}s + {\omega_L}^2\right)\left(s^2 + \frac{\omega_L}{Q_L}s + {\omega_L}^2\right)\left(s^2 + \gamma s\right) \tag{5.17}$$

The expression of $Z_{IN}(s)$ is derived from the passive network with the addition of resistance (R) is series with every inductor as shown in Figure **5.22**.

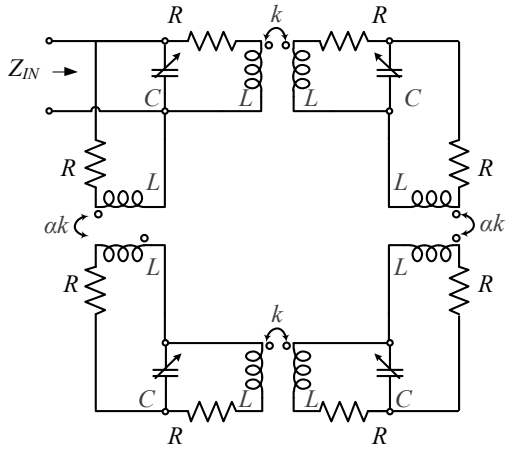

Figure 5.22: *Passive network corresponding to the passive quadrature voltage controlled oscillator with the series resistance (R_S) considered*

The corresponding denominator expression

$$\begin{aligned} D(s) = {} & \frac{R^2{\omega_0}^4}{(-1+k^2)L^2(-1+k^2\alpha^2)} + \frac{2R{\omega_0}^2(R^2+L^2{\omega_0}^2)}{(-1+k^2)L^3(-1+k^2\alpha^2)}s^2 \\ & + \frac{4R^4 + 24L^2R^2{\omega_0}^2 - L^4(-4+k^2(1+\alpha^2)){\omega_0}^4}{4(-1+k^2)L^4(-1+k^2\alpha^2)}s^2 \\ & + \frac{R(4R^2 - L^2(-6+k^2(1+\alpha^2)){\omega_0}^2)}{(-1+k^2)L^3(-1+k^2\alpha^2)}s^3 \\ & - \frac{R^2(-6+k^2(1+\alpha^2)) + L^2(-2+k^2(1+\alpha^2)){\omega_0}^2}{(-1+k^2)L^2(-1+k^2\alpha^2)}s^4 \\ & + -\frac{2R(-2+k^2(1+\alpha^2))}{(-1+k^2)L(-1+k^2\alpha^2)}s^5 + s^6 \end{aligned} \tag{5.18}$$

By equating the *s*, s^3 and s^5 terms in equations (5.17) and (5.18), the quality factors Q_L and Q_H are given by

$$Q_{H,L} = \frac{(1-\mathrm{k}^2)(1-\alpha\mathrm{k}^2)}{2\left(2-(1+\alpha)\mathrm{k}^2-4\dfrac{\omega_0^{\,2}}{\omega_{H,L}^{\,2}}\right)}\frac{\left(1-\dfrac{\omega_{H,L}^{\,2}}{\omega_{L,H}^{\,2}}\right)}{\left(1-\dfrac{\omega_{H,L}^{\,2}}{\omega_0^{\,2}}\right)}\frac{\omega_{L,H}^{\,2}}{\omega_0^{\,2}}\frac{\omega_{H,L}L}{R} \tag{5.19}$$

The expression in (5.19) corresponds to the quality factor of the inductors at resonance ($\omega_{H,L}L/R$) scaled by a factor that is a function of α, k, $\omega_{H,L\ and}\ \omega_{H,L}$. For the special case α=1, the expression simplifies to

$$Q_{H,L} = \frac{\left(1\pm\frac{\mathrm{k}}{\sqrt{2}}\right)\left(1-\mathrm{k}^2\right)}{1\pm\sqrt{2}\mathrm{k}+\mathrm{k}^2} \tag{5.20}$$

The equivalent parallel resistance at resonance is evaluated as $R=\dfrac{1}{C}\dfrac{Q_{H,L}}{\omega_{H,L}}$, and the corresponding start-up condition is $G_{MN}\pm G_{MP}>\dfrac{2}{R}$. The impact of this is captured by Figure **5.23** and Figure **5.24**.

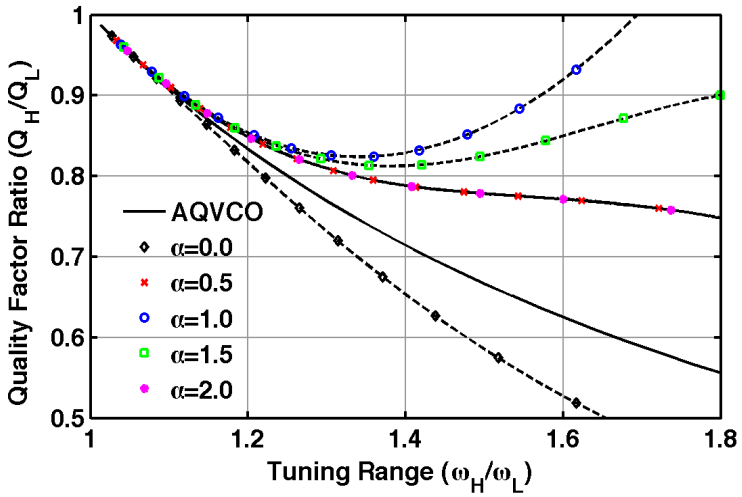

Figure 5.23: *The ratio of the quality factor in the high resonance mode to that in the low resonance mode as a function of the tuning range given by the frequency ratio of the high resonance mode to the low resonance mode for*

AQVCO and PQVCO with multiple values of α

In Figure **5.23**, the quality factor ratio Q_H/Q_L is plotted as the tuning range. As the quality tuning range increases, so does the ratio of quality factor between Q_H and Q_L for the AQVCO case. This results in startup conditions being drastically different at the two resonance frequencies. However, for the PQVCO and for a range of α values, the ratio of quality factor between the two resonance modes drops, which results in more similar startup condition between the high and low resonance modes. This however has the negative impact of lowering the overall quality factor which is captured by Figure **5.24**, which shows the ratio of the high resonance mode quality factor of the resonance circuit (Q_H) to the quality factor of the corresponding inductor at the same resonance frequency ($\omega_H L/R_S$). For all values of α, the quality factor in the high resonance mode of the PQVCO is lower than that of the AQVCO for the same tuning range. This impact can be overcome by using a larger coupling inductor than that used inside the dual-resonance core.

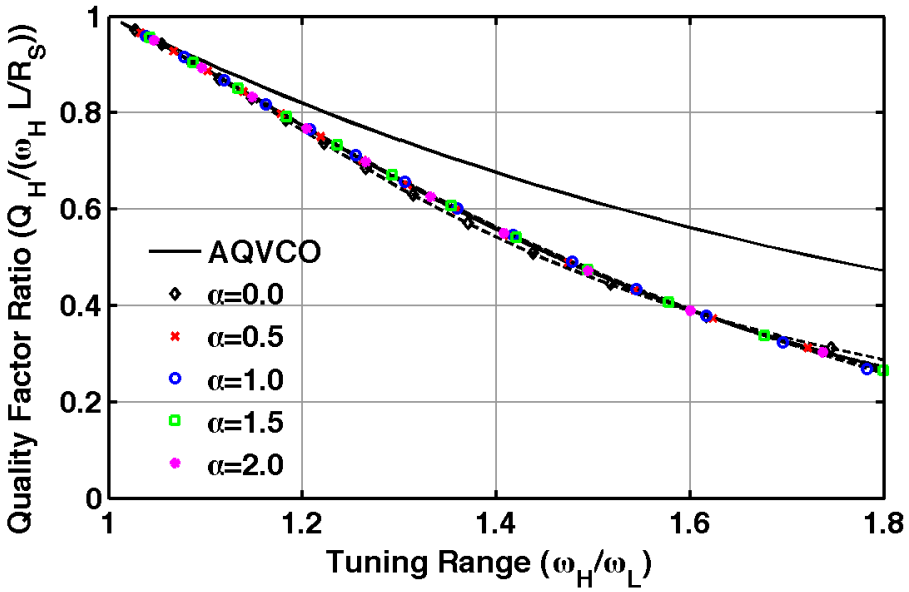

Figure 5.24: *The ratio of the quality factor in the high resonance mode to the quality factor of the inductor at the same frequency as a function of the tuning range given by the frequency ratio of the high resonance mode to the low resonance mode for AQVCO and PQVCO with multiple values of α*

5.3.1. Phase noise and phase error

The phase noise of the passively coupled dual-resonance QVCO circuit can be approximated by applying the quadrature theory presented in Section 2.6 to the equivalent 2nd order simplification circuit presented in Section 3.3. The simplified circuit is shown in Figure **5.25**.

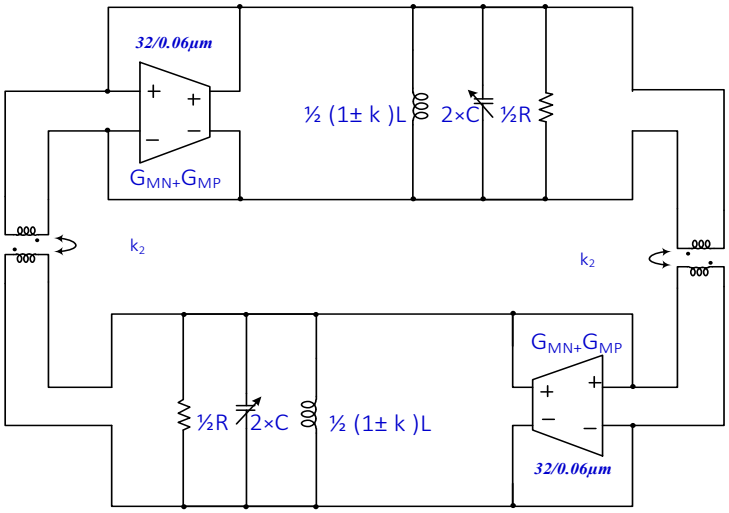

Figure 5.25: *Passive quadrature voltage controlled oscillator 2nd order equivalent circuit*

It is important to note that while this simplification allows for a simple derivation of phase noise, it's not a strictly accurate simplification. It has been pointed out in [9] and [10] that a circuit which consists of two oscillators coupled through any type of passive symmetric passive networks and a 180° inversion, can never be coupled due to even symmetries. Therefore, in reality, it is important to have 4 oscillators (such as the case of the dual-resonance passive quadrature), with non-zero phase shifts between each oscillating node, in the quadrature configuration to have a properly locked QVCO. Under this simplification, the phase noise can be simply found as:

$$L_{1/f^2}(\Delta\omega) = 10Log\left(\frac{(1+\gamma)\left(\frac{4k_bT}{R_P}\right)}{16(Q)^2 I_{\omega 0}{}^2}\left(\frac{f_0}{\Delta f}\right)^2\right) \tag{5.21}$$

This is due to the fact that in the simplified model, no two current vectors of different phases sum up at any node; therefore the ISFs are always in quadrature with the voltage at each node. In the non-simplified circuit model, there is a phase difference between the two oscillating nodes in each dual-resonance oscillator. This phase difference, if significant, leads to creating phasors between currents, which should be considered for ISF calculation. In order to verify the significant of this phase shift on the design, the circuit is simulated. To allow for proper comparison with the active QVCO, the circuit is simulated using the same Verilog-A models for G_M that were presented in Section 2.6.

The resulting plot is shown in Figure **5.26** compares the theoretical expression in (5.21) (PN_1) with the simulated phase noise (PN_4) and the phase noise calculated from simulated ISFs (PN_3). The three expression match very well, which indicates the original assumption that the passive dual resonance circuit does not suffer from noises contributed by active quadrature or in other words they have similar phase noise to that of active quadrature when the active coupling factor is 0.

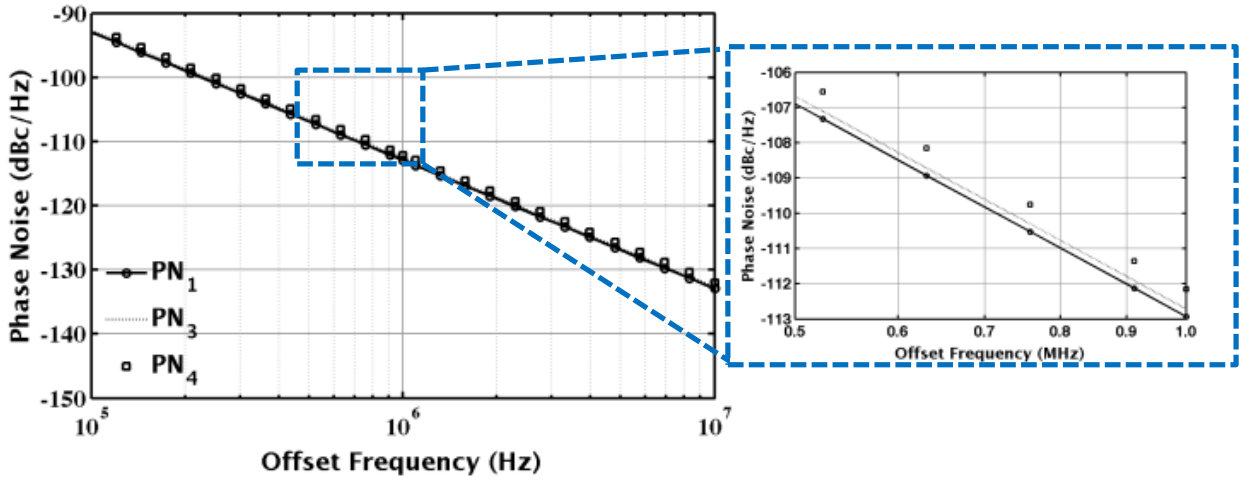

Figure 5.26: *Phase noise plots for passive dual-resonance QVCO*

The phase error due to mismatches of the dual resonance PQVCO can be empirically derived using a series of simulations by considering that the error would follow an equation similar to that in equation (5.13) as follows

$$\Delta\varphi = C_1(\alpha)\frac{\Delta I}{2I} + C_2(\alpha)Q\frac{\Delta\omega}{\omega_0} + C_3(\alpha)\frac{\Delta R}{R} + \frac{\Delta\Psi}{2} \tag{5.22}$$

The constant C_1, C_2 and C_3 are experimentally evaluated and compared to the AQVCO case. The resulting comparison is shown in Figure **5.27**. The phase error appears to be inversely proportional to the coupling strength α and it shows good coupling for $\alpha=1$ that is comparable to that of the AQVCO with quadrature coupling strength k=0.25. However, mismatches between the two coupling transformers appear directly as phase delay mismatches ΔΨ which are frequency dependent, and they result in quadrature phase errors that would require additional phase delay control to calibrate.

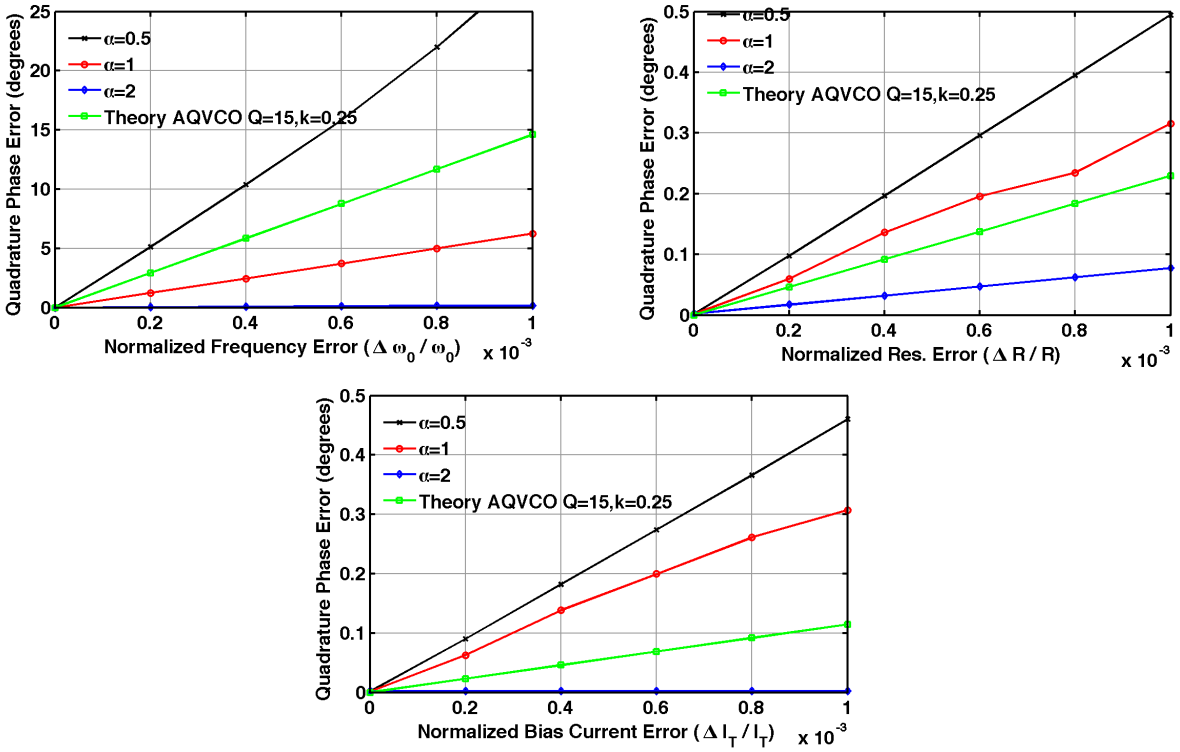

Figure 5.27: *Quadrature phase error versus mismatch in* (*a*) *resonance frequency* , (*b*) *tank resistance and* (*c*) *bias current of the two dual-resonance cores in the case of AQVCO* (*Q=15, and k=0.25*) *and PQVCO with* α*=0.5,1,2*

Chapter 6
CIRCUIT MEASUREMENT

6.1. Introduction

This chapter also presents the measurement data obtained for both chips for both phase noise and phase error measurements. The tuning range and power consumption measurement results are presented as part of the phase noise measurement, since the phase noise measurement was conducted across the full tuning range. For both measurements, the measurement setup and theory are explained. Furthermore, a comparison with state-of-art circuits is presented and the figures of merit (FOMs) are derived based on them.

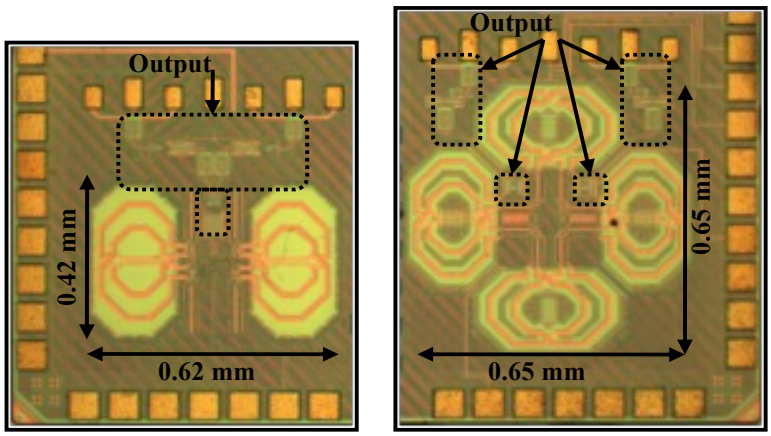

(a) (b)

Figure 6.1: *Die photo of* (*a*) *active coupled QVCO and* (*b*) *passive coupled QVCO*

Two standalone VCO designs were taped out in TSMCs 65nm Process. Both design featured digital control via a serial to parallel digital controller. The controls were used to tune the capacitor arrays, the bias current and the resonance mode selection. Both designs were followed by two stages of buffers to mitigate the off-chip loading impact on the circuit.

The die photo of the two VCOs is depicted in Figure **6.1**. The measurement made use of a set of 3 probes: two eye-pass probes for bias and digital control signals, and 1 SGS probe for output

monitoring. A set of 2.92mm cables along with connectors and various instruments were used to collect the phase noise and quadrature phase error data.

6.2. Phase Noise Measurement

6.2.1. Methodology

The measurement of phase noise can be performed using a number of methods. The main challenge lies in measuring a noisy, unlocked VCO oscillating at a high frequency. Advanced measurement instruments have reduced the complexity of performing phase noise measurements. This subsection briefly investigates the theory behind a number of the methods employed by these instruments.

6.2.2. Direct spectrum power density measurement at oscillation frequency

As discussed in section 2.5, and expressed in (2.28), the phase noise can be directly computed from the power spectral density of the oscillating signal. While this method is direct, it requires a stable and frequency locked oscillation in order to capture the spectrum correctly.

6.2.3. Phase detectors

The phase detector is used to decouple the phase noise on one hand, and the oscillation frequency on the other. This has two main advantages: 1) The measurement no longer requires a locked oscillation (though the phase detector's architecture might set stability requirements on the signal), and 2) The measurement is only concerned with offset frequencies (often are considered up to a 100 MHz) rather than having to capture high frequency (GHz) VCO outputs.

A simple phase detector can be realized by a mixer followed by a low pass filter as depicted in Figure **6.2** . As indicated by equations (6.1), a VCO under test has the output waveform given by

$V_{VCO}(t)$. If there exists a waveform ($V_X(t)$) that has the same oscillation frequency (ω_0) and a different phase, then the filtered down output is approximately the difference between the two phases scaled by some factor K_{PD} (under small angle approximation as before).

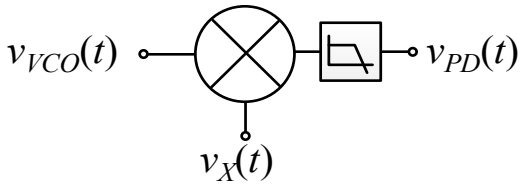

Figure 6.2:*Mixer and low pass filter as simple phase detector*

$$
\begin{aligned}
v_{VCO}(t) &= V_{VCO0}\cos(\omega_0 t + \varphi_{VCO}(t)) \\
v_X(t) &= V_{X0}\cos(\omega_0 t + \varphi_X(t)) \\
v_{PD}(t) &= K_{PD}\cos(\varphi_{VCO}(t) - \varphi_X(t)) \approx K_{PD}(\varphi_{VCO}(t) - \varphi_X(t))
\end{aligned}
\tag{6.1}
$$

6.2.4. Phase locked loop

One way to generate the waveform $V_X(t)$ is using a phase locked loop. Qualitatively, the loop locks the phases of the local oscillator ($V_{LO}(t)$) and the VCO under test ($V_{VCO}(t)$) up to the bandwidth of the loop. The residual phase difference is effectively high pass filtered. If the loop's bandwidth is sufficiently low and the phase noise of the LO is well below that of the VCO under test, then the output $V_O(t)$ will be directly proportional to the phase noise of the VCO under test.

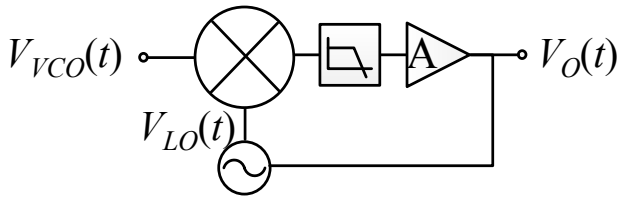

Figure 6.3: *First order PLL as a phase noise measurement setup*

Mathematically, assuming the phase noise of the LO is much lower than that of the VCO under test, the output phase can be expressed in the frequency domain as:

$$\varphi_{\mathrm{O}}(\mathrm{s}) = \frac{s}{K_{LO}\left(1+\frac{s}{AK_{PD}K_{LO}}\right)}\varphi_n(\mathrm{s}) \qquad (6.2)$$
$$V_{\mathrm{O}}(\mathrm{s}) \approx \varphi_O(\mathrm{s})$$

This is a high pass response whose pass frequency ω_{3dB} equals $AK_{PD}K_{LO}$, where K_{PD} is the phase detector's gain and K_{PD} is the LO gain and both are assumed to be constants. Note that the pass frequency needs to be set low enough to pass the phase noise, yet high enough to guarantee locking. This method is better suited for signals with low phase noise or frequency locked.

6.2.5. Delay line frequency discriminator

The delay line discriminator mixes the VCO's waveform with a delayed version of itself as shown in Figure **6.4**, instead of generating a second oscillation as the case in the PLL setup.

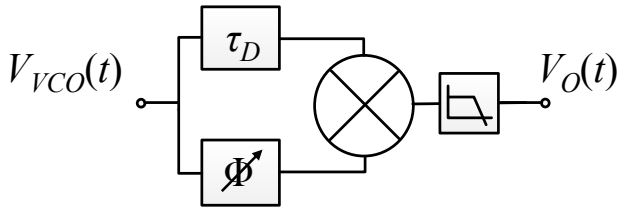

Figure 6.4: *Delay line discriminator as a phase noise measurement setup*

The delay line is configured so that the phase difference between the signal and its timed delayed version is π/2. Hence the output of the phase detector can be written as:

$$V_O(t) = K_{PD}\sin(\varphi_n(t) - \varphi_n(t-\tau)) \qquad (6.3)$$

It was shown in [27] that the spectrum of output voltage is related to the spectrum of the frequency noise (ω_n) as given in equation (6.4):

$$V_{\mathrm{O}}(f) = K_{PD}\tau_{\mathrm{D}}\left(\frac{\sin(\pi f\tau_{\mathrm{D}})}{\pi f\tau_{\mathrm{D}}}\right)\omega_n(f)$$

$$\varphi_{\mathrm{n}}(f) = \omega_n(f)/f \quad \text{or} \quad L(\Delta f) \approx \frac{S_{\omega_n}(\Delta f)}{2(\Delta f)^2} \tag{6.4}$$

It's important to note that the relationship between frequency noise and output voltage is colored by a sinc function with a notch at frequency $1/\tau_D$. Hence, in order to make a measurement, either the sinc function has to be calibrated out or τ_D has to be small enough so that the offset frequencies of interest are in the "flat" region of the sinc response. The disadvantage of using a small τ_D is the loss of output voltage sensitivity to frequency noise. This method is often used with unlocked signals and signals with high close-in spurious content, which would make it hard to measure using the PLL method.

The main disadvantage of this method is the need for programmable delay lines which are frequency dependent. Advancement in Digital Signal processing (DSP) allowed for the development of the heterodyne discriminator [28]. It is a two step process where the signal under test is first down converted into a lower frequency, and then digitized using a fast ADC. If the phase noise of the down converted signal is dominated by the phase noise of the signal under test, then it is sufficient to apply the frequency discrimination method to it, to obtain the phase noise of the original signal. Once the down converted signal is digitized, an arbitrary delay can be applied to it using a DSP algorithm.

6.2.6. Measurement Setup

The phase noise measurement was performed using the *E5052B Signal Source Analyzer* accompanied by *E5053A Microwave down-converter*. The *E5052B* is capable of performing heterodyne frequency discrimination measurements as well as PLL based measurements. The

E5053A down converter extend the frequency range to cover 3 GHz to 26.5 GHz as shown in Figure **6.5**.

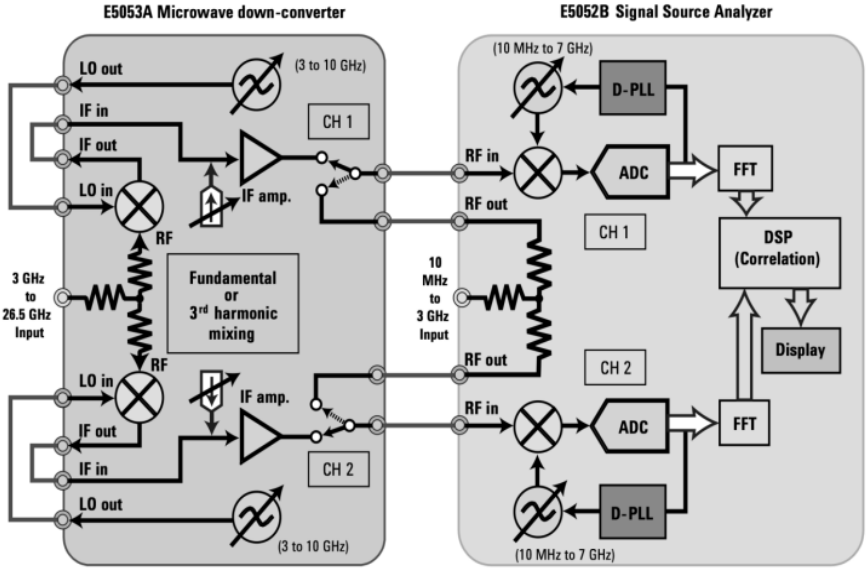

Figure 6.5: *E5052B Signal Source Analyzer connected to E5053A Microwave down-converter* [29]

6.3. Results

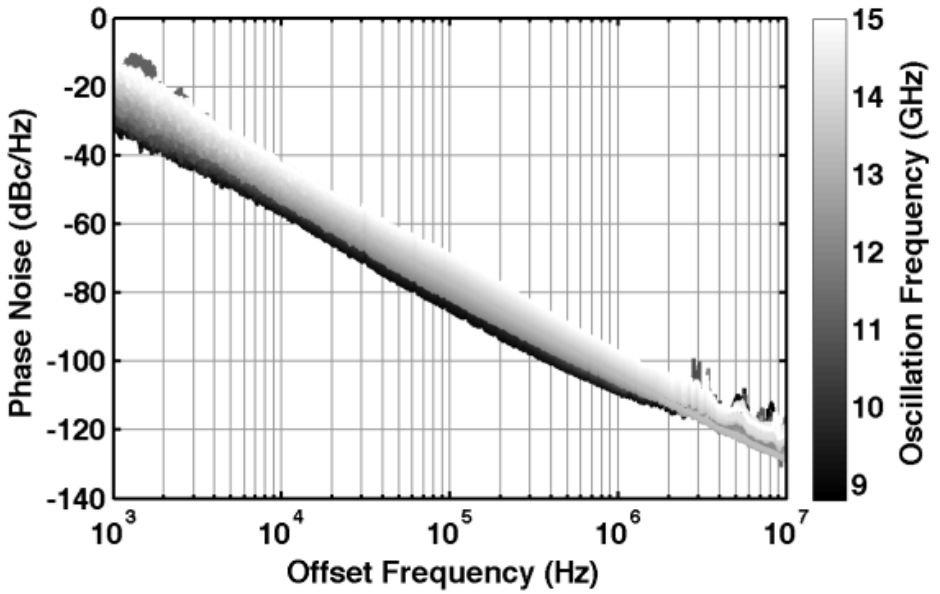

(a)

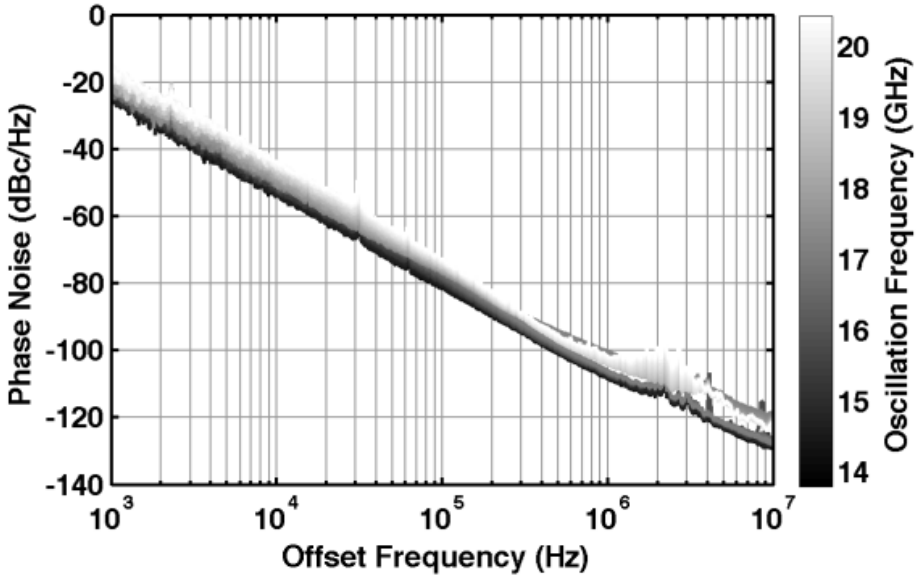

(b)

Figure 6.6: *Raw collected phase noise data for* (*a*) *active coupled QVCO and* (*b*) *passive coupled QVCO for offset frequencies ranging from 1 kHz to 10MHz superposed for multiple frequency points collected over the full tuning range of each QVCO*

The measurement was automated to collect phase noise sweeps for all digital code configurations. The raw collected data is presented in Figure **6.6**.

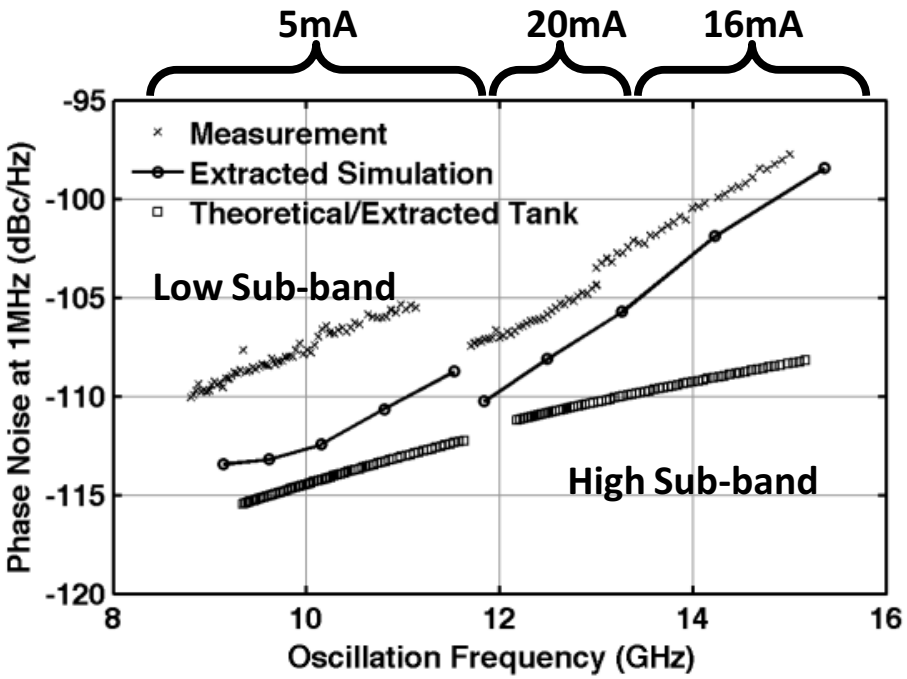

(a)

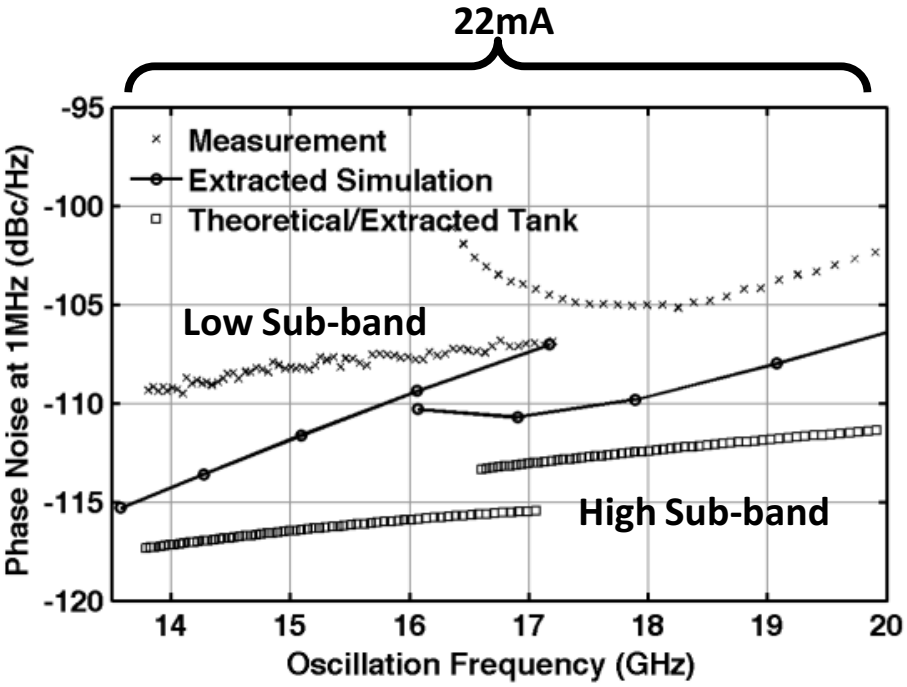

(b)

Figure 6.7: *Phase noise measured for* (*a*) *active coupled QVCO and* (*b*) *passive coupled QVCO at an offset frequency of 1MHz collected over the full tuning range of each QVCO, with current consumption of the QVCO noted for each arrangement over different frequency ranges that was used in the measurement*

6.4. Quadrature Phase Measurement

6.4.1. Methodology

The measurement of quadrature can be done using a wide range of methods. The most common method uses image rejection of either up or down conversion quadrature mixing schemes to determine the phase error angle.

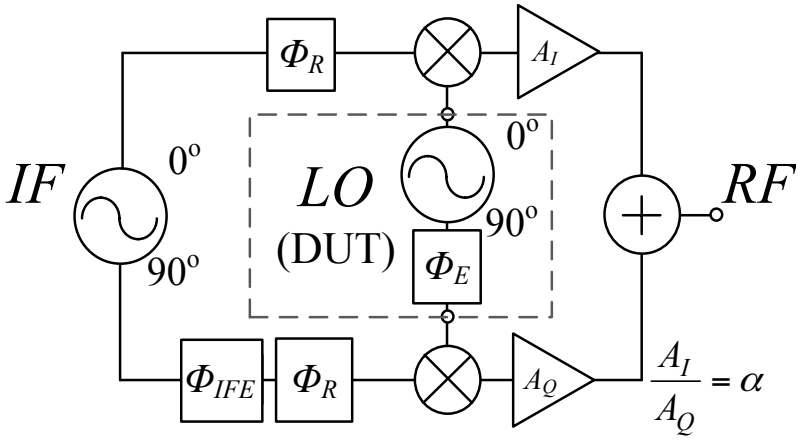

Figure 6.8: *Quadrature upconversion architecture used in quadrature phase accuracy measurement considering different circuit non-idealities that require to be measured/calibrated* (A_I, A_Q, Φ_{IFE}, Φ_R)

Considering the upconversion circuit displayed in Figure **6.8**, the goal of the measurement is to measure the phase error (Φ_E) of the quadrature VCO under test by upconverting a known quadrature low frequency signal (*IF*) and using power combining to cancel the positive or the negative sideband image (*LO* + *IF*, *LO* - *IF*). The challenge lies in capturing and calibrating all the other non-idealities in the circuit such as *IF* phase error (Φ_{IFE}), *IF* phase rotation (Φ_{IFE}), and gain mismatch between *I* channel and *Q* channel (A_I vs. A_Q).

Given sinusoidal signals, the setup in Figure **6.8** can be described by the following equations:

$$
\begin{aligned}
& V_{RF}(\mathrm{t}) = \alpha A_Q V_{IFI}(t) V_{LOI}(t) + A_Q V_{IFQ}(t) V_{LOQ}(t) \\
& V_{LOI}(t) = \cos(\omega_{LO} t) \\
\textit{LO (DUT)} \qquad & V_{LOQ}(t) = \sin(\omega_{LO} t + \phi_E) \\
& V_{IFI}(t) = \cos(\omega_{IF} t + \phi_R) \\
\textit{IF} \qquad & V_{IFQ}(t) = \sin(\omega_{IF} t + \phi_R + \phi_{IFE})
\end{aligned}
\tag{6.5}
$$

$$
V_{RF}(\mathrm{t}) = \frac{A_Q}{2}\begin{pmatrix} \alpha\cos(\phi_R + (\omega_{LO} + \omega_{IF})t) - \cos(\phi_E + \phi_{IFE} + \phi_R + (\omega_{LO} + \omega_{IF})t) + \\ \alpha\cos(-\phi_R + (\omega_{LO} - \omega_{IF})t) + \cos(\phi_E - \phi_{IFE} - \phi_R + (\omega_{LO} - \omega_{IF})t) \end{pmatrix}
$$

The ratio of the powers of the upper sideband (ω_{LO}+ ω_{IF}) and the lower sideband (ω_{LO}- ω_{IF}) is given by the expression $R_P(\alpha, \Phi_E, \Phi_{IFE})$ in (6.6)

$$
R_P(\alpha, \phi_E, \phi_{IFE}) = \frac{1 + \alpha^2 - 2\alpha\cos(\phi_E + \phi_{IFE})}{1 + \alpha^2 + 2\alpha\cos(\phi_E - \phi_{IFE})} \tag{6.6}
$$

In the special case where α=1, and Φ_{IFE} =0, the expression simplifies to that in (6.7)

$$
R_P(\phi_E) = \tan^2\frac{\phi_E}{2} \tag{6.7}
$$

Typically, the phase measurement apparatus is set up using voltage limiters to equate amplitudes and a calibration process is performed to set the *IF* phase error to zero. However, this is hard to achieve off chip at high frequencies over a wide frequency range. As it can be seen in Figure **6.9**, the image rejection magnitude (in dB), for an ideal case where there is no amplitude imbalance between the I/Q channels, the sensitivity of the phase measurement around 0 degrees is very high and an image rejection greater than 42 dB indicates a phase error less than 1^o.

However, as amplitude imbalances are introduced (α = 0.1, 0.4, 0.7), not only does the image rejection become a function of the amplitude imbalance, but also the sensitivity to phase error increases, which reduces the measurement's accuracy.

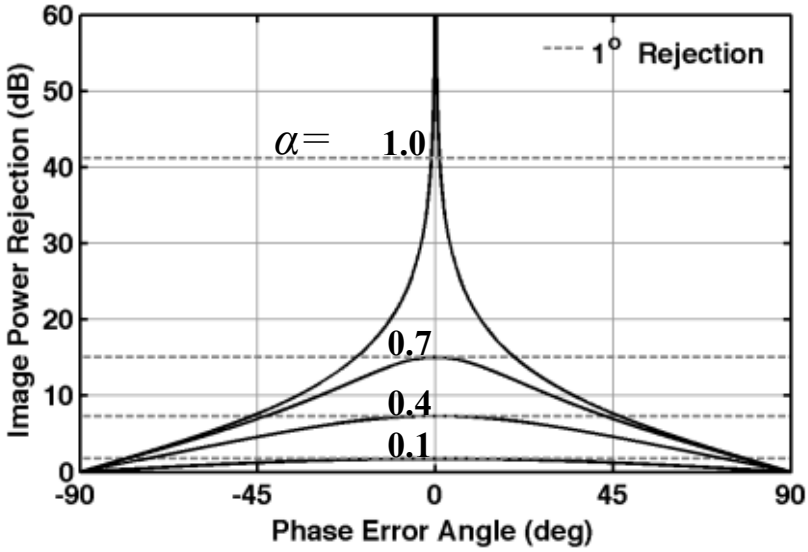

Figure 6.9: *Image rejection of a quadrature up/down converter as a function of phase error and I/Q channels gain mismatches*

In order to allow for an accurate measurement of phase error, we conduct the experiment with a swept *IF* phase. By doing so, we inherently can calibrate out *IF* phase error, and separate the phase error measurement from the amplitude imbalance. The use of *IF* sweeps aims at finding the *IF* phases for which the image rejection is maximum. We begin by rewriting the equation in (6.6) in terms of Φ_{IF} instead of Φ_{IFE}, where Φ_{IF} refers to the absolute phase difference between the *IF* signal in the I and the Q channels. The resulting image power rejection ratio is given by (6.8):

$$R_P(\alpha,\phi_E,\phi_{IF}) = \frac{1+\alpha^2-2\alpha\sin(\phi_E+\phi_{IF})}{1+\alpha^2-2\alpha\sin(\phi_E-\phi_{IF})} \tag{6.8}$$

The maximum image power rejection angle is given by (6.9)

$$\phi_{IF\,R_{PMAX}}(\alpha,\phi_E) = \pm\cos^{-1}\left(\frac{2\alpha}{1+\alpha^2}\cos\left(\frac{\pi}{2}-\phi_E\right)\right) \tag{6.9}$$

Assuming small angle approximations, this maxim image power rejection $R_{PMAX}(\alpha)$ and the corresponding Φ_{IF} are given by (6.10):

$$R_{PMAX}(\alpha) \approx \left(\frac{1\pm\alpha}{1\mp\alpha}\right)^2 \tag{6.10}$$

$$\phi_{IF\,R_{PMAX}}(\alpha,\phi_E) \approx \pm\left(\frac{\pi}{2} - \frac{2\alpha}{1+\alpha^2}\phi_E\right)$$

From the previous two equations we notice that for very small error signals:

1) The calibration of Φ_{IF} is inherent; because Φ_{IFPMAX} are symmetric around Φ_{IF}=0.
2) The maximum image rejection is only a function of amplitude imbalances.
3) Once amplitude imbalance (α) and Φ_{IF}=0 are known, Φ_E can be readily found.

These results are depicted in Figure **6.11** (a). The plot is constructed by sweeping the phase error Φ_E and plotting the resulting R_{PMAX} as a function Φ_{IFPMAX} as well as Φ_E. In addition the small signal approximation expression is plotted (it's phase independent). The plot shows there is very good correspondence between the "R_{PMAX} *vs.* Φ_{IFPMAX}" and ""R_{PMAX} *vs.* Φ_E" well beyond small angle approximation for moderate alpha values.

Consequently, one can use Φ_{IFPMAX} as an approximation of Φ_E. In order to facilitate this task, Figure **6.10** (b) shows the contours of errors in this approximation. One can set an upper bound on the approximation based on the required accuracy and the limitations on the measurement (mainly noise and phase steps). If a measurement falls beyond the tolerance, exact phase error can be calculated using a numerical solution to equations (6.8) and (6.9).

The main disadvantage of this method is that it requires the stepping of the *IF* phase with fine steps and constant amplitude, which requires advance instrumentation. However, it's a method where no calibration is needed.

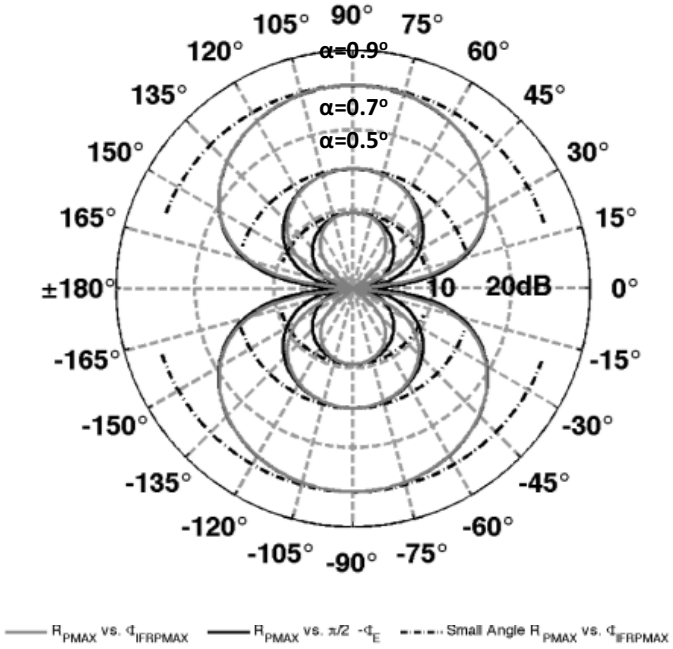

(a)

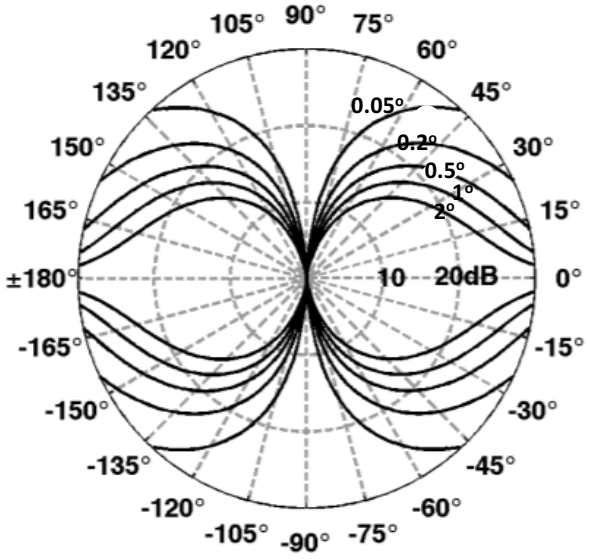

(b)

Figure 6.10: (*a*) *Maximum image rejection* R_{PMAX} *as a function of maximum image rejection angle* (Φ_{IFPMAX})*, phase error* (Φ_E) *and small signal approximation* (*given by*(*6.10*)) *for three different amplitude imbalance values* (α=*0.5,0.7,0.9*). (*b*) *Phase estimation error contours* (Φ_E -Φ_{IFPMAX}) *of the maximum image rejection* R_{PMAX} *as a function of maximum image rejection angle* (Φ_{IFPMAX}) *plot*

6.4.2. Measurement Setup

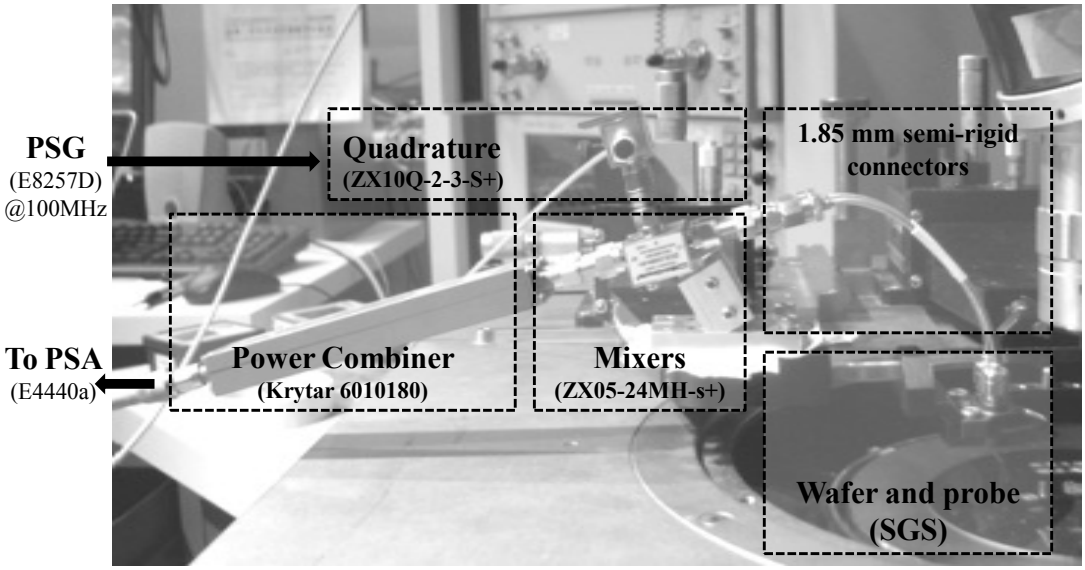

Figure 6.11: *Quadrature upconversion measurement setup picture with parts and test equipment marked*

An initial measurement setup shown in Figure **6.11** was used to characterize the phase. An SGS probe similar to the case for phase noise was landed on both the *I* and the *Q* channels of the quadrature VCO and both channels were connected to off chip mixers (ZX05-24MH-s+). The *IF* was initially derived from a 90^{o} power splitter (ZX10Q-2-3-S+). However due to amplitude imbalances, the quadrature was replaced by two 50MHz signals from an arbitrary waveform generator (Arb: Tektronix AWG70002A) with a swept phase difference as described in the previous section. The outputs of the mixers were combined using a Krytar 6010180 power splitter/combiner and the output was observed in the E4440a power signal analyzer (PSA).

The measurement was automated to step through *IF* phase difference derived from the Arb (with coarse and fine sweeps). For each phase point the power data was capture by the PSA, the relevant peaks were detected and their power ratio is calculated, and logged vs. the angle.

6.4.3. Results

The raw measured data of the phase sweeps is presented in

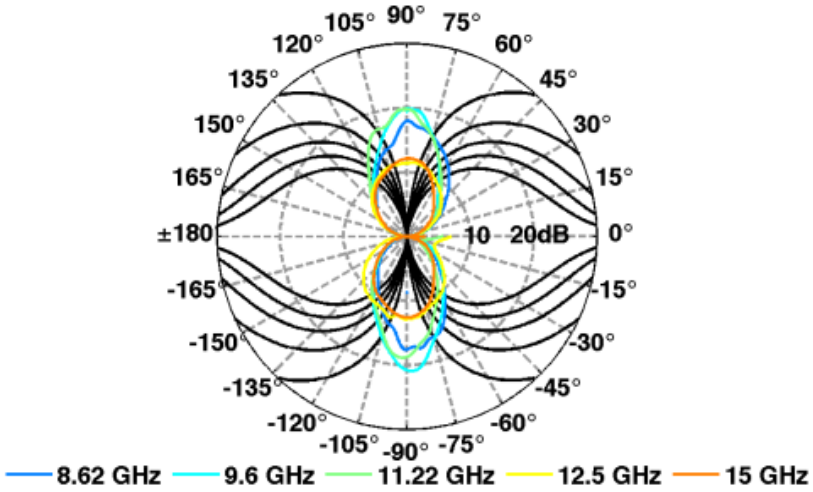

(a)

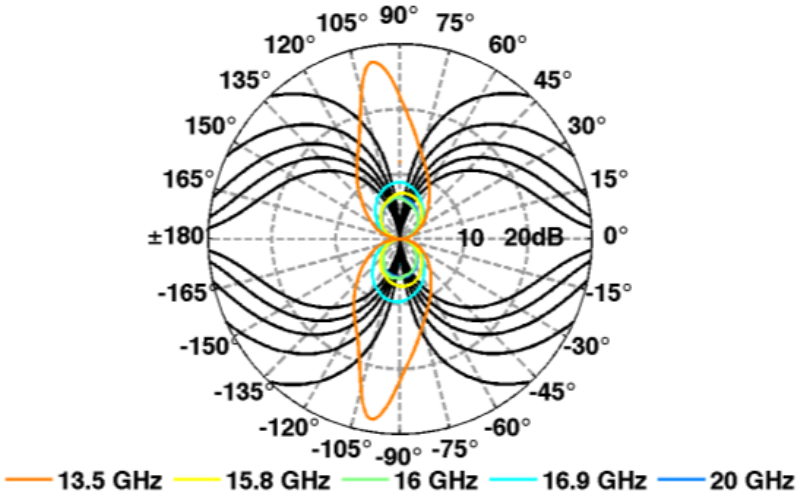

(b)

Figure 6.12: *Raw collected image rejection vs. IF phase sweep data for* (*a*) *active coupled QVCO and* (*b*) *passive coupled QVCO with phase estimation error contours given in Figure* **6.10** (*b*) *marked on each plot*

Using the previous data and the methodology discussed in the previous section the actual phase figures are computed and presented is Figure **6.13**.

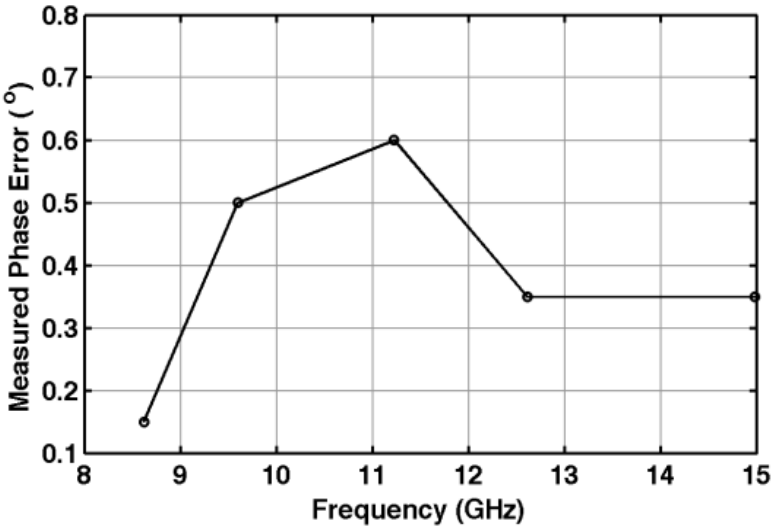

(a)

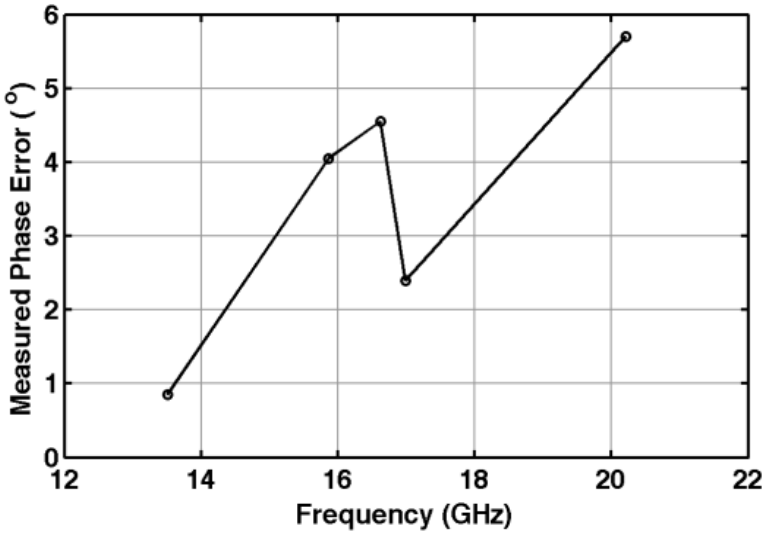

(b)

Figure 6.13: *Phase errors of* (*a*) *active coupled QVCO and* (*b*) *passive coupled QVCO calculated as the maximum image rejection angle in the phase sweeps presented in Figure* **6.12**

6.5. Overall Performance

For the sake of comparison, a number of figures of merit are introduced and used to compare this work with other works in the literature. Originally the phase noise figure of merit (FOM_{PN}) has been used to compare oscillators. It aims at capturing the architecture's ability to minimize phase noise for a given power budget and oscillation frequency at a certain frequency offset.

$$FOM_{PN} = L(\Delta f) - 10\log\left(\frac{1}{P_{DC}(mW)}\left(\frac{f_0}{\Delta f}\right)^2\right) \tag{6.11}$$

Since this *FOM* doesn't capture the tradeoff between tuning range, phase noise and power budget, a second *FOM* denoted FOM_T is introduced to capture the tuning range.

$$FOM_T = L(\Delta f) - 10\log\left(\frac{1}{P_{DC}(mW)}\left(\frac{f_{MAX} - f_{MIN}}{\Delta f}\right)^2\right) \tag{6.12}$$

A final figure of merit aims similar to (6.12) is given by FOM_{T2} with further emphasis on fractional tuning range versus absolute tuning range, which agrees more with the discussion presented on tradeoffs between fractional tuning range and phase noise for a given power budget presented in 4.5.

$$FOM_{T2} = L(\Delta f) - 10\log\left(\frac{1}{P_{DC}(mW)}\left(\frac{f_0}{\Delta f}\right)^2\right) - 20\log\left(\frac{FTR}{10\%}\right) \tag{6.13}$$

The FOMs are plotted across the tuning range of both passive and active QVCO in Figure **6.14**. The works are compared with the state-of-art designs in Table 8.

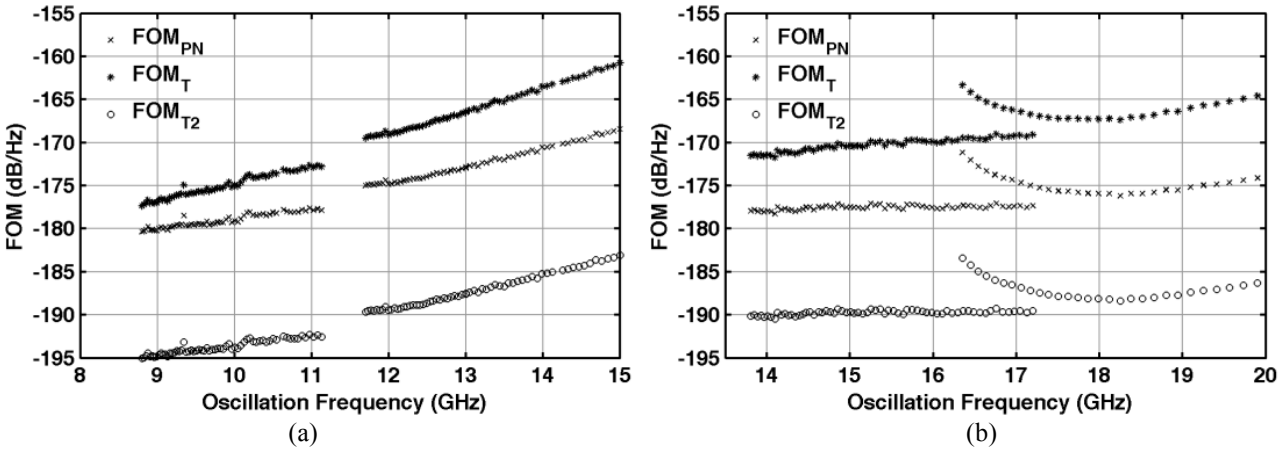

Figure 6.14: *FOM_{PN} ,FOM_T and FOM_{T2} of the* (*a*) *active coupled QVCO and* (*b*) *passive coupled QVCO evaluated for an offset frequency of 1MHz over the full tuning range*

Table 8: *Performance comparison with state-of-art wideband VCO designs*

		Saberi et al (2011)	Bajestan et al (2015)	This Work (Active)	This Work (Passive)
Process		130nm	65nm	65 nm	65 nm
Center Frequency	*GHz*	13.3	3.8	12	17
Tuning Range	%	62.7	78	46	36
Supply Voltage	V	1.2	0.6	1.2	1.2
Power	*mW*	20-29	5.8-9.4	6 -19.2	26.4
Phase Noise (1 MHz offset at center frequency)	*dBc/Hz*	-107	-123.7	-107	-109
FOM(PN)	*dB/Hz*	-175.59	-186.49	-177.58	-179.39
FOM(T)	*dB/Hz*	-171.53	-184.33	-170.84	-170.52
FOM(T2)	*dB/Hz*	-191.53	-204.33	-190.84	-190.52
Area	mm^2		0.35	0.27	0.42
Phase Error	o	<3.3	<1.5	<0.6	<6

Chapter 7
CONCLUSION AND FUTURE WORK

In order to create a wideband voltage controlled oscillator, a necessary component for multi-standard and cognitive radios, this thesis presented two QVCO designs targeted towards the 10-20GHz bands. Dual-resonance is a key feature of the presented work, which aimed at generating wider tuning range using little area overhead and without sacrificing phase noise. The two architectures used a dual-resonance circuit core with symmetrically tuned coupled resonators. The resonance mode was selected using a digital code that controlled the feedback architecture in the circuit.

The two architectures employed passive and active mechanisms to obtain quadrature in the circuit. The underlying premise is that an active loop can provide a very accurate quadrature angles, at the expense of added phase noise. On the other hand, passive architectures have lower phase noises, but their quadrature accuracy is susceptible to passive element imbalances.

Low phase noise, and low quadrature phase error are desired. Quadrature angle accuracy is necessary for image rejection and has significant impacts on receiver sensitivity. Similarly, phase noise reduces the sensitivity of radios and makes them more susceptible to blockers. An ideal design should aim at minimizing both.

This thesis presented principles of voltage controlled oscillator design that focused on the design of LC-tank VCOs. The main concepts that were introduced in this context were startup condition, phase noise, and quadrature accuracy.

The previous analysis was made relevant to the studying of a dual-resonance VCO, which is the main building block of the two QVCOs presented in this thesis, by introducing a method of circuit reduction that allowed for the reduction of the 4-th order network of the dual-resonance

VCO, to a 2nd order LC-tank. Startup condition, phase noise analysis and quadrature accuracy theory considered previously was extended based on this model. Impulse sensitivity function analysis, based on linear time invariant phase noise theory, was presented as a mean to study the phase noise contribution of different circuit elements.

In order to achieve wide tuning, while not sacrificing phase noise, the passives (tune-LC networks) were analyzed. The advantage of using high bandwidth switches such as phase change switches was studied, and quantified through mathematical expressions that capture that tradeoff between phase noise, tuning range and the switch bandwidth.

The theory introduced was reflected in the design of the two QVCOs which were presented with focus on the circuit, dual-resonance passive resonator design, and startup conditions of both architectures. This was then compared and contrasted with the measured results which showed agreement in general trends.

The results presented have shown that it is possible to obtain equal phase noise to power consumed performance at higher frequencies, as defined by FOMs, using passive QVCO compared to the active QVCO. However, the passive QVCO needed higher currents in order to obtain startup. This was the case because the passive QVCO architecture was implemented using parallel dual resonators, halving the parallel tank resistance and doubling the required G_M. Additionally, the phase error of the passive QVCO (6^o) is significantly larger than the active one which was within 0.6^o. Additional circuitry is needed to control and reduce this error.

The circuit design can be enhanced by the introduction of a phase error correction unit. Architectures can range from introduction of tuned coupling capacitance between the resonators, phase-shifters, and additional digital logic. The error correction circuit can either use a set of

calibration points in addition to digital lookup tables, or a closed loop image rejection based receiver with negative feedback.

Furthermore, the design can be furthered by introducing a combined architecture that employs phase change switches and both QVCOs in order to generate frequencies over the range of 8-20 GHz. Since the loops share a lot and have been implemented using the same unit elements, it can be possible to use phase change switches to chose between inductive coupling and active device coupling. In doing so, a much wider tuning range can be obtained with minimal impact on the phase noise of the lower frequency bands. The higher frequency bands, on the other hand, which would be implemented using the phase change switched inductors need to be further studied, since even 1Ω resistance in series with the inductors can half its quality factor at resonance.

References

[1] P. Andreani, X. Wang, L. Vandi, and A. Fard, "A study of phase noise in colpitts and LC-tank CMOS oscillators," *IEEE J. Solid-State Circuits*, vol. 40, no. 5, pp. 1107–1118, 2005.

[2] B. Razavi, "A study of injection locking and pulling in oscillators," *IEEE J. Solid-State Circuits*, vol. 39, no. 9, pp. 1415–1424, Sep. 2004.

[3] L. Romano, S. Levantino, C. Samori, and A. L. Lacaita, "Multiphase LC oscillators," *Circuits Syst. I Regul. Pap. IEEE Trans.*, vol. 53, no. 7, pp. 1579–1588, 2006.

[4] A. Mazzanti and P. Andreani, "On the amplitude and phase errors of quadrature LC-tank CMOS oscillators," *IEEE J. Solid-State Circuits*, vol. 41, no. 6, pp. 1305–1313, 2006.

[5] A. Bevilacqua, F. P. Pavan, C. Sandner, A. Gerosa, and A. Neviani, "A 3.4-7 GHz transformer-based dual-mode wideband VCO," in *ESSCIRC 2006 - Proceedings of the 32nd European Solid-State Circuits Conference*, 2006, pp. 440–443.

[6] S. Saberi and J. Paramesh, "A 11.5-22GHz dual-resonance transformer-coupled quadrature VCO," in *Digest of Papers - IEEE Radio Frequency Integrated Circuits Symposium*, 2011, vol. 22, no. 1, pp. 4–7.

[7] G. Li, L. Liu, Y. Tang, and E. Afshari, "A low-phase-noise wide-tuning-range oscillator based on resonant mode Switching," *IEEE J. Solid-State Circuits*, vol. 47, no. 6, pp. 1295–1308, 2012.

[8] A. Ravi, K. Soumyanath, R. E. Bishop, B. A. Bloechel, and L. R. Carley, "An optimally transformer coupled , 5 GHz Quadrature VCO in a 0.18um digital CMOS process," pp. 4–7, 2003.

[9] C. T. Fu and H. C. Luong, "A 0.8-V CMOS quadrature LC VCO using capacitive coupling," *2007 IEEE Asian Solid-State Circuits Conf. A-SSCC*, vol. 2, no. 1, pp. 436–439, 2007.

[10] N. Kuo, S. Member, J. Chien, and A. M. Niknejad, "Design and Analysis on Bidirectionally and Passively Coupled QVCO With Nonlinear Coupler," vol. 63, no. 4, pp. 1130–1141, 2015.

[11] U. Decanis, A. Ghilioni, E. Monaco, A. Mazzanti, and F. Svelto, "A low-noise quadrature VCO based on magnetically coupled resonators and a wideband frequency divider at millimeter waves," in *IEEE Journal of Solid-State Circuits*, 2011, vol. 46, no. 12, pp. 2943–2955.

[12] G. Li and E. Afshari, "A low-phase-noise wide-tuning-range quadrature oscillator in 65nm CMOS," *Proc. Cust. Integr. Circuits Conf.*, pp. 3–6, 2012.

[13] M. M. Bajestan, V. D. Rezaei, and K. Entesari, "A Low Phase-Noise Wide Tuning-Range Quadrature Oscillator Using a Transformer-Based Dual-Resonance LC Ring," vol. 63, no. 4, pp. 1142–1153, 2015.

[14] M. M. Bajestan, V. D. Rezaei, and K. Entesari, "A 2.75-6.25GHz low-phase-noise quadrature VCO based on a dual-mode ring resonator in 65nm CMOS," *Dig. Pap. - IEEE Radio Freq. Integr. Circuits Symp.*, pp. 265–268, 2014.

[15] Q. Wu, T. Quach, A. Mattamana, S. Elabd, S. R. Dooley, J. J. McCue, P. L. Orlando, G. L. Creech, and W. Khalil, "Design of Wide Tuning-Range mm-Wave VCOs Using Negative Capacitance," *2012 IEEE Compd. Semicond. Integr. Circuit Symp.*, pp. 1–4, Oct. 2012.

[16] L. Fanori, A. Liscidini, and R. Castello, "Capacitive degeneration in LC-tank oscillator for DCO fine-frequency tuning," in *IEEE Journal of Solid-State Circuits*, 2010, vol. 45, no. 12, pp. 2737–2745.

[17] D. B. Leeson, "A simple model of feedback oscillator noise spectrum," *Proc. IEEE*, vol. 54, no. 2, pp. 329–330, 1966.

[18] A. Hajimiri, S. Member, and T. H. Lee, "A General Theory of Phase Noise in Electrical Oscillators," vol. 33, no. 2, pp. 179–195, 1998.

[19] P. Andreani, "On the phase-noise and phase-error performances of multiphase LC CMOS VCOs," *IEEE J. Solid-State Circuits*, vol. 39, no. 11, pp. 1883–1893, Nov. 2004.

[20] A. Hajimiri and T. H. Lee, "Design issues in CMOS differential LC oscillators," *IEEE J. Solid-State Circuits*, vol. 34, no. 5, pp. 717–724, 1999.

[21] F. Pepe, P. Milano, P. Milano, F. Pepe, A. Bonfanti, and A. L. Lacaita, "A fast and accurate simulation method of impulse sensitivity function in oscillators A fast and accurate simulation method of Impulse Sensitivity Function in oscillators," no. January, 2016.

[22] A. Mazzanti and P. Andreani, "Class-C harmonic CMOS VCOs, with a general result on phase noise," in *IEEE Journal of Solid-State Circuits*, 2008, vol. 43, no. 12, pp. 2716–2729.

[23] a. . Mirzaei, M. E. Heidari, R. . Bagheri, S. . Chehrazi, and a. a. Abidi, "The Quadrature LC Oscillator: A Complete

Portrait Based on Injection Locking," *IEEE J. Solid-State Circuits*, vol. 42, no. 9, pp. 1916–1932, Sep. 2007.

[24] A. Mazzanti and P. Andreani, "A time-variant analysis of fundamental 1/f3 phase noise in CMOS parallel LC-tank quadrature oscillators," *IEEE Trans. Circuits Syst. I Regul. Pap.*, vol. 56, no. 10, pp. 2173–2180, 2009.

[25] E. Hegazi and A. A. Abidi, "Varactor characteristics, oscillator tuning curves, and AM-FM conversion," *IEEE J. Solid-State Circuits*, vol. 38, no. 6, pp. 1033–1039, 2003.

[26] Q. Wu, S. Elabd, T. K. Quach, A. Mattamana, S. R. Dooley, J. McCue, P. L. Orlando, G. L. Creech, and W. Khalil, "A −189 dBc/Hz FOMT wide tuning range Ka-band VCO using tunable negative capacitance and inductance redistribution," *2013 IEEE Radio Freq. Integr. Circuits Symp.*, pp. 199–202, Jun. 2013.

[27] Hewlett-Packard, "Phase Noise Characterization of Microwave Oscillators." 1985.

[28] K. Gheen, "Phase Noise Measurement Methods and Techniques," *Aerosp. Def. Symp.*, 2012.

[29] A. Note, "Agilent E5052A Signal Source Analyzer Advanced Phase Noise and Transient Measurement Techniques."

[30] P. Andreani, A. Bonfanti, L. Romanò, and C. Samori, "Analysis and design of a 1.8-GHz CMOS LC quadrature VCO," in *IEEE Journal of Solid-State Circuits*, 2002, vol. 37, no. 12, pp. 1737–1747.

[31] B. Çatli and M. M. Hella, "A dual band, wide tuning range CMOS voltage controlled oscillator for multi-band radio," in *Digest of Papers - IEEE Radio Frequency Integrated Circuits Symposium*, 2007, pp. 595–598.

[32] M. Tiebout, "Low-power low-phase-noise differentially tuned quadrature VCO design in standard CMOS," *IEEE J. Solid-State Circuits*, vol. 36, no. 7, pp. 1018–1024, Jul. 2001.

[33] M. Tsuru, K. Kawakami, K. Tajima, K. Miyamoto, M. Nakane, K. Itoh, M. Miyazaki, and Y. Isota, "A Triple-Tuned Ultra-Wideband VCO," *IEEE Trans. Microw. Theory Tech.*, vol. 56, no. 2, pp. 346–354, 2008.

[34] A. W. L. Ng and H. C. Luong, "A 1-V 17-GHz 5-mW CMOS quadrature VCO based on transformer coupling," in *IEEE Journal of Solid-State Circuits*, 2007, vol. 42, no. 9, pp. 1933–1941.

[35] P. Andreani, "A phase noise analysis of CMOS colpitts oscillators," *Proc. Norchip Conf.*, no. 1, pp. 151–154, 2004.

[36] P. Andreani, "Phase noise analysis of the LC-tank CMOS oscillator," *Proc. Norchip Conf.*, no. 6, pp. 147–150, 2004.

[37] M. Hopkinson, C. Jin, H. Liu, and R. Airey, "1.34 μm GaInNAs quantum well lasers with low room-temperature threshold current density," vol. 42, no. 7, pp. 1–2, 2006.

[38] M. Bagheri, R. Bagheri, and L. E. Larson, "A CMOS quadrature oscillator with deterministic output sequence," *2011 IEEE 11th Top. Meet. Silicon Monolith. Integr. Circuits RF Syst.*, pp. 1–4, Jan. 2011.

[39] A. Bevilacqua, F. P. Pavan, C. Sandner, A. Gerosa, and A. Neviani, "Transformer-Based Dual-Mode Voltage-Controlled Oscillators," *IEEE Trans. Circuits Syst. II Express Briefs*, vol. 54, no. 4, pp. 293–297, Apr. 2007.

[40] G. Cusmai, M. Repossi, G. Albasini, A. Mazzanti, and F. Svelto, "A Magnetically Tuned Quadrature Oscillator," in *IEEE Journal of Solid-State Circuits*, 2007, vol. 42, no. 12, pp. 2870–2877.

[41] T. Djurhuus, V. Krozer, J. Vidkjær, and T. K. Johansen, "Trade-off between phase-noise and signal quadrature in unilaterally coupled oscillators," in *IEEE MTT-S International Microwave Symposium Digest*, 2005, vol. 2005, no. C, pp. 883–886.

[42] B. Çath and M. M. Hella, "A 1.94 to 2.55 GHz, 3.6 to 4.77 GHz tunable CMOS VCO based on double-tuned, double-driven coupled resonators," *IEEE J. Solid-State Circuits*, vol. 44, no. 9, pp. 2463–2477, 2009.

[43] S. L. J. Gierkink, S. Levantino, R. C. Frye, C. Samori, and V. Boccuzzi, "A low-phase-noise 5-GHz CMOS quadrature VCO using superharmonic coupling," *IEEE J. Solid-State Circuits*, vol. 38, no. 7, pp. 1148–1154, Jul. 2003.

[44] K. K. Lee, C. Bryant, M. Törmänen, and H. Sjöland, "A 65-nm CMOS ultra-low-power LC quadrature VCO," in *2009 NORCHIP*, 2009, no. 5, pp. 6–9.

[45] D. Murphy, J. J. Rael, and A. A. Abidi, "Phase noise in LC oscillators: A phasor-based analysis of a general result and of loaded Q," *IEEE Trans. Circuits Syst. I Regul. Pap.*, vol. 57, no. 6, pp. 1187–1203, 2010.

[46] A. Bevilacqua and P. Andreani, "Phase Noise Analysis of the Tuned-Input-Tuned-Output (TITO) Oscillator," vol. 59, no. 1, pp. 20–24, 2012.

[47] S. Rong and H. C. Luong, "Analysis and design of transformer-based dual-band VCO for software-defined radios," *IEEE Trans. Circuits Syst. I Regul. Pap.*, vol. 59, no. 3, pp. 449–462, 2012.

[48] J. R. Long and M. a. Copeland, "The modeling, characterization, and design of monolithic inductors for silicon RF IC's," *IEEE J. Solid-State Circuits*, vol. 32, no. 3, pp. 357–368, 1997.